EUROPEAN ORGANIZATION FOR NUCLEAR RESEARCH (CERN)

CERN-EP-2024-231
2024/09/18

CMS-TOP-23-007

Measurements of polarization and spin correlation and observation of entanglement in top quark pairs using lepton+jets events from proton-proton collisions at $\sqrt{s} = 13\,\mathrm{TeV}$

The CMS Collaboration*

Abstract

Measurements of the polarization and spin correlation in top quark pairs ($\mathrm{t\bar{t}}$) are presented using events with a single electron or muon and jets in the final state. The measurements are based on proton-proton collision data from the LHC at $\sqrt{s} = 13\,\mathrm{TeV}$ collected by the CMS experiment, corresponding to an integrated luminosity of $138\,\mathrm{fb}^{-1}$. All coefficients of the polarization vectors and the spin correlation matrix are extracted simultaneously by performing a binned likelihood fit to the data. The measurement is performed inclusively and in bins of additional observables, such as the mass of the $\mathrm{t\bar{t}}$ system and the top quark scattering angle in the $\mathrm{t\bar{t}}$ rest frame. The measured polarization and spin correlation are in agreement with the standard model. From the measured spin correlation, conclusions on the $\mathrm{t\bar{t}}$ spin entanglement are drawn by applying the Peres–Horodecki criterion. The standard model predicts entangled spins for $\mathrm{t\bar{t}}$ states at the production threshold and at high masses of the $\mathrm{t\bar{t}}$ system. Entanglement is observed for the first time in events at high $\mathrm{t\bar{t}}$ mass, where a large fraction of the $\mathrm{t\bar{t}}$ decays are space-like separated, with an expected and observed significance of above 5 standard deviations.

Submitted to Physical Review D

*See Appendix A for the list of collaboration members

1 Introduction

The top quark is the most massive known fundamental particle with a lifetime of the order of 10^{-25} s. This is shorter than the quantum chromodynamics (QCD) hadronization time scale $1/\Lambda_{\mathrm{QCD}} \approx 10^{-24}$ s, and the spin decorrelation time scale $m_{\mathrm{t}}/\Lambda^2_{\mathrm{QCD}} \approx 10^{-21}$ s, where m_{t} is the top quark mass [1, 2]. Consequently, the top quark usually decays before hadronization, thus preserving its spin information in the angular distribution of the decay products. This makes top quark and antiquark ($\mathrm{t\bar{t}}$) pairs excellent candidates for studying polarization and spin correlation.

We present measurements of the polarization and spin correlation in $\mathrm{t\bar{t}}$ pairs using proton-proton collisions at a center-of-mass energy of 13 TeV at the CERN LHC. The measurements are performed using data collected by the CMS detector between 2016 and 2018, corresponding to an integrated luminosity of $138\,\mathrm{fb}^{-1}$. Once produced, a top quark decays via the weak interaction into a W boson and a b quark. The W boson further decays into either two quarks, which subsequently hadronize into jets, or a charged lepton and a neutrino. In this analysis, we focus on the final state with two b jets, two jets from one W boson, and an electron or muon paired with a neutrino from the other W boson. This decay channel is referred to as the e/μ+jets channel.

At the LHC $\mathrm{t\bar{t}}$ pairs are produced through gluon-gluon (gg) fusion and quark-antiquark ($\mathrm{q\bar{q}}$) annihilation. The top quarks and antiquarks are unpolarized at leading order (LO). However, their spins are expected to be strongly correlated [3]. The complete spin correlation is encoded in a $3{\times}3$ matrix that depends on the $\mathrm{t\bar{t}}$ production mechanism, the invariant mass of the $\mathrm{t\bar{t}}$ system $m(\mathrm{t\bar{t}})$, and the scattering angle of the top quark. Evidence for $\mathrm{t\bar{t}}$ spin correlation was first reported by the D0 experiment at the Tevatron in Refs. [4, 5]. The ATLAS and CMS experiments have performed a number of top quark polarization and spin correlation measurements using various observables and data sets [6–15].

The top quark polarization and spin correlation measurement is interesting in its own right as a test of the standard model (SM) [16, 17], but it also provides new opportunities for testing quantum mechanics (QM) at high energies using the decay products of unstable particles as probes. This is not possible in experiments with stable particles, such as electrons and photons. An important prediction of QM is quantum entanglement, which has been studied in connection with particle physics at high energies only in recent years [18–21]. The ATLAS and CMS experiments reported the observation of entanglement in the $\mathrm{t\bar{t}}$ system at the production threshold [14, 15]. In this paper we also include measurements of entanglement at high $m(\mathrm{t\bar{t}})$.

This paper is organized in the following way. First, we outline the measurement strategy in Section 2. We briefly describe the CMS detector in Section 3 and then discuss the signal and background modeling used for this analysis in Section 4. The event selection and the $\mathrm{t\bar{t}}$ reconstruction are described in Sections 5 and 6, respectively, followed by a discussion of the background estimation in Section 7 and the extraction of the polarization and spin correlation coefficients in Section 8. Systematic uncertainties are detailed in Section 9. Finally, the results are presented in Section 10 and the paper is summarized in Section 11. Tabulated results are provided in the HEPData record for this analysis [22].

2 Measurement strategy

We perform a measurement of the $\mathrm{t\bar{t}}$ polarization and spin correlation in the helicity basis $\{n, r, k\}$ following Ref. [23]. This basis is defined by boosting the top quarks and their decay products from the laboratory frame into the $t\bar{t}$ rest frame. Afterward, based on the unit vectors in the top quark direction $\hat{k}$ and the beam in the positive z-direction $\hat{b}$, the axes of the new coordinate system are given by

$$\hat{n} = \frac{\hat{b} \times \hat{k}}{\sin(\theta)}, \quad \hat{r} = \frac{\hat{b} - \cos(\theta)\hat{k}}{\sin(\theta)}, \quad \hat{k}, \tag{1}$$

where θ is the scattering angle of the top quark, i.e., $\cos(\theta) = \hat{b} \cdot \hat{k}$. The Bose–Einstein symmetry of the gg initial state [23] requires a redefinition of the n and r axes (which are odd under Bose–Einstein symmetry) to allow nonzero values of the polarization and spin correlation coefficients involving an odd number of these axes. This is done by multiplying the n and r directions by the sign of $\cos(\theta)$, which is also odd under Bose–Einstein symmetry, such that all axes are even under Bose–Einstein symmetry:

$$\{n, r, k\} \to \{\text{sgn}(\cos(\theta))n,\ \text{sgn}(\cos(\theta))r,\ k\}. \tag{2}$$

Finally, the top quark and antiquark are boosted individually into their rest frames together with their corresponding decay products.

In this basis, the unit vector

$$\mathbf{\Omega}(\bar{\mathbf{\Omega}}) = \big(\sin(\theta_{\text{p}(\bar{\text{p}})})\cos(\phi_{\text{p}(\bar{\text{p}})}), \sin(\theta_{\text{p}(\bar{\text{p}})})\sin(\phi_{\text{p}(\bar{\text{p}})}), \cos(\theta_{\text{p}(\bar{\text{p}})})\big) \tag{3}$$

describes the direction of a decay product $\text{p}(\bar{\text{p}})$ of the top (anti)quark, where $\phi_{\text{p}(\bar{\text{p}})}$ is the azimuthal and $\theta_{\text{p}(\bar{\text{p}})}$ the polar angle of the decay product. The differential cross section as a function of the four variables $\phi_{\text{p}(\bar{\text{p}})}$ and $\theta_{\text{p}(\bar{\text{p}})}$ has the form

$$\begin{aligned} \Sigma_{\text{tot}}(\phi_{\text{p}(\bar{\text{p}})}, \theta_{\text{p}(\bar{\text{p}})}) &= \frac{\text{d}^4\sigma}{\text{d}\phi_{\text{p}}\,\text{d}\cos(\theta_{\text{p}})\,\text{d}\phi_{\bar{\text{p}}}\,\text{d}\cos(\theta_{\bar{\text{p}}})} \\ &= \sigma_{\text{norm}}\big(1 + \kappa\mathbf{P}\cdot\mathbf{\Omega} + \bar{\kappa}\bar{\mathbf{P}}\cdot\bar{\mathbf{\Omega}} - \kappa\bar{\kappa}\mathbf{\Omega}\cdot(C\bar{\mathbf{\Omega}})\big), \end{aligned} \tag{4}$$

with two 3-dimensional polarization vectors $\mathbf{P}$ and $\bar{\mathbf{P}}$, and one 3×3 spin correlation matrix C. This means that Σ_{tot} depends linearly on 15 coefficients collectively referred to as $Q_m = \{P_n, P_r, P_k, \bar{P}_n, \ldots, C_{nn}, C_{nr}, \ldots, C_{kk}\}$. In this analysis, we perform a measurement of all 15 coefficients, which we subsequently refer to as the full matrix measurement. There is one additional coefficient σ_{norm} that describes the overall normalization. The spin analyzing power κ represents how much information from the top quark spin is transferred to its decay products. We use the down-type quarks and the charged leptons in the W boson decays. The magnitude of κ for these decay products have the maximum value of unity at LO. Including QCD corrections, the magnitude of κ for down-type quarks is reduced to 0.966 [24]. However, we perform the measurements using the LO values and leave the application of different κ values for reinterpretations. For simplicity, we flip the sign of κ for $\bar{t}$ decays following the convention of Ref. [3], instead of inverting the axes of the coordinate system as in Refs. [15, 23].

The top quark, being a spin-1/2 particle, can be described as a two-state quantum system known as a qubit. The minimal example of an entangled state consists of two qubits, e.g., a $t\bar{t}$ pair, where the entanglement can be characterized by their spin correlation. The Peres–Horodecki criterion [25, 26] can be used to determine if a quantum state is separable. If the state is not separable, it is considered entangled. In general, a quantum state is described by a density matrix ρ, in this case a spin density matrix whose coefficients are probed by Eq. (4). A quantum state is said to be separable if ρ can be factorized into individual states belonging to separate subspaces, i.e., $\rho = \sum_n q_n \rho_n^a \otimes \rho_n^b$, where ρ_n^a, ρ_n^b are density matrices describing the quantum states of the subsystems a and b and the q_n are the corresponding probabilities. If ρ is a separable physical state, the state $\rho^{T_2} = \sum_n q_n \rho_n^a \otimes (\rho_n^b)^T$ resulting from taking the transpose for only subsystem b should also be a physical state. It was demonstrated [25, 26] that a sufficient condition for entanglement is that ρ^{T_2} has at least one negative eigenvalue, meaning it is not a physical state. This translates to a sufficient condition for entanglement based on the diagonal elements of the spin correlation matrix [18, 27]:

$$\Delta_{\mathrm{E}} = C_{nn} + |C_{rr} + C_{kk}| > 1. \tag{5}$$

Based on the measured values of the spin correlation matrix we apply this criterion to evaluate the entanglement of the $\mathrm{t\bar{t}}$ system in different regions of phase space.

As an alternative to the full matrix measurement, we measure angular variables directly sensitive to Δ_{E}. The trace of the spin correlation matrix $\mathrm{Tr}(C)$ can be probed using the opening angle χ between the two decay products in the helicity basis, $\cos(\chi) = \mathbf{\Omega} \cdot \bar{\mathbf{\Omega}}$. This observable is sensitive to the entanglement in the spin-singlet state [18] expected from gg fusion events at the $\mathrm{t\bar{t}}$ production threshold. The distribution of χ is given by

$$\frac{\mathrm{d}\sigma}{\mathrm{d}\cos(\chi)} = \sigma_{\mathrm{norm}}\big(1 + D\kappa\bar{\kappa}\cos(\chi)\big), \text{ where } D = -\frac{1}{3}\,\mathrm{Tr}(C). \tag{6}$$

For gg fusion events at low $m(\mathrm{t\bar{t}})$, both C_{rr} and C_{kk} are positive [3], which simplifies the entanglement criterion to

$$\Delta_{\mathrm{E}} = -3D = \mathrm{Tr}(C) > 1. \tag{7}$$

The entanglement in a spin-triplet state, predicted in both $\mathrm{q\bar{q}}$ annihilation and gg fusion events with high $m(\mathrm{t\bar{t}})$ and low $|\cos(\theta)|$, can be probed using a criterion based on [3, 28]

$$\tilde{D} = \frac{1}{3}(C_{nn} - C_{rr} - C_{kk}). \tag{8}$$

The signs of C_{rr} and C_{kk} become negative at transverse momentum of the top quark $p_{\mathrm{T}}(\mathrm{t}) \sim m_{\mathrm{t}}$ [3], so the entanglement criterion based on $\tilde{D}$ in the high-$m(\mathrm{t\bar{t}})$ region is:

$$\Delta_{\mathrm{E}} = 3\tilde{D} > 1. \tag{9}$$

The extraction of $\tilde{D}$ is performed using $\tilde{\chi} = -\Omega_n\bar{\Omega}_n + \Omega_r\bar{\Omega}_r + \Omega_k\bar{\Omega}_k$, analogous to χ but with an inverted sign of the n-component of one of the decay products.

3 The CMS detector

The central feature of the CMS apparatus is a superconducting solenoid of 6 m internal diameter, providing a magnetic field of 3.8 T. Within the solenoid volume are a silicon pixel and strip tracker, a lead tungstate crystal electromagnetic calorimeter (ECAL), and a brass and scintillator hadron calorimeter (HCAL), each composed of a barrel and two endcap sections. Forward calorimeters extend the pseudorapidity (η) coverage provided by the barrel and endcap detectors. Muons are measured in gas-ionization detectors embedded in the steel flux-return yoke outside the solenoid.

Events of interest are selected using a two-tiered trigger system. The first level (L1), composed of custom hardware processors, uses information from the calorimeters and muon detectors to select events at a rate of around 100 kHz within a fixed latency of about 4 μs [29]. The second level, known as the high-level trigger, consists of a farm of processors running a version of the full event reconstruction software optimized for fast processing, and reduces the event rate to around 1 kHz before data storage [30]. For this measurement events are selected using single electron and muon triggers for isolated leptons with minimum p_{T} requirements, depending on the year, of 24 and 27 GeV for muons and 27 and 32 GeV for electrons.

The primary vertex is taken to be the vertex corresponding to the hardest scattering in the event, evaluated using tracking information alone, as described in Section 9.4.1 of Ref. [31]. The particle-flow (PF) algorithm [32] aims to reconstruct and identify each individual particle in an event, with an optimized combination of information from various elements of the CMS detector. The energy of photons is obtained from the ECAL measurement. The energy of electrons is determined from a combination of the electron momentum at the primary interaction vertex as determined by the tracker, the energy of the corresponding ECAL cluster, and the energy sum of all bremsstrahlung photons spatially compatible with originating from the electron track. The energy of muons is obtained from the curvature of the corresponding track. The energy of charged hadrons is determined from a combination of their momentum measured in the tracker and the matching ECAL and HCAL energy deposits, corrected for the response function of the calorimeters to hadronic showers. Finally, the energy of neutral hadrons is obtained from the corresponding corrected ECAL and HCAL energies. A more detailed description of the CMS detector, together with a definition of the coordinate system used and the relevant kinematic variables, can be found in Ref. [33].

4 Signal and background modeling

The matrix element (ME) event generator POWHEG V2 [34–36] is used to simulate $\mathrm{t\bar{t}}$ events with next-to-LO (NLO) QCD accuracy. It is subsequently combined with the parton shower (PS) simulation from PYTHIA 8.230 [37], using the underlying event tune CP5 [38]. In addition, a sample of $\mathrm{t\bar{t}}$ production at next-to-NLO (NNLO) QCD is generated with POWHEG MINNLO [39] in combination with the CP5 PYTHIA tune. This is used to estimate uncertainties in the contribution from higher-order QCD. Similarly, for the estimation of electroweak corrections, we use the HATHOR 2.1-B3 package [40]. The measured coefficients are compared to the predictions obtained using POWHEG+HERWIG 7.1 [41] with tune CH3 [42] and MADGRAPH5_aMC@NLO 2.6.1 [43] combining ME calculations at NLO QCD including up to two additional partons with the PYTHIA PS using the FXFX algorithm [44]. In all $\mathrm{t\bar{t}}$ simulations, the decays of the top quarks including the spin correlation are evaluated at LO precision.

The $\mathrm{t\bar{t}}$ simulations are normalized to the inclusive cross section value of 832^{+40}_{-46} pb [45] which is calculated with NNLO precision including soft-gluon resummation at the level of next-to-next-to-leading-logarithm. The renormalization scale μ_{r} and factorization scale μ_{f} are taken to be equal to the average transverse mass of the top quark and antiquark, $m_{\mathrm{T}} = 0.5(\sqrt{m_{\mathrm{t}}^2 + p_{\mathrm{T}}(\mathrm{t})^2} + \sqrt{m_{\mathrm{t}}^2 + p_{\mathrm{T}}(\bar{\mathrm{t}})^2})$, where p_{T} is the transverse momentum of the top quark evaluated in the $\mathrm{t\bar{t}}$ rest frame, and $m_{\mathrm{t}} = 172.5\,\mathrm{GeV}$ [46] is used in all simulations, unless stated otherwise. The main background processes in this analysis are single top quark production, Drell–Yan (DY) and W boson production in association with jets, and events composed uniquely of jets produced through the strong interaction, referred to as QCD multijet events. Single top quark production via t channel and top quark production in association with a W boson are generated using POWHEG+PYTHIA, while the production via s channel is generated at NLO QCD using MADGRAPH5_aMC@NLO+PYTHIA. The simulation of background from DY+jets and W+jets production is performed at LO QCD using MADGRAPH5_aMC@NLO+PYTHIA with the MLM PS matching [47, 48] of up to four partons. The QCD multijet processes are simulated at LO using PYTHIA. The cross sections are taken from NNLO calculations for W+jets and DY+jets events [49] and NLO calculations for single top quark events [50, 51]. The default parameterization of the parton distribution functions (PDFs) used in all simulations is the NNLO version of NNPDF 3.1 [52].

The detector response is modeled using GEANT4 [53]. Additional proton-proton interactions within the same or nearby bunch crossings (pileup) are overlaid on each simulated event. Simulated events are assigned event weights based on the number of pileup interactions to match the pileup distribution in data. The same reconstruction algorithms that are applied to the data are used for simulated events.

5 Physics object reconstruction

The measurements presented in this analysis depend on the reconstruction and identification of electrons, muons, jets, and the missing transverse momentum $\vec{p}_{\mathrm{T}}^{\mathrm{miss}}$ associated with neutrinos.

Electrons [54] and muons [55] are selected if they are isolated and compatible with originating from the primary vertex. Moreover, they must have $p_{\mathrm{T}} > 30\,\mathrm{GeV}$ and $|\eta| < 2.4$. In the 2018 data set, the minimum p_{T} of electrons was raised to 34 GeV because of the increased trigger thresholds. Leptons are required to satisfy several quality criteria including isolation and compatibility with the primary vertex. The electron and muon reconstruction and selection efficiencies are measured in the data using the "tag-and-probe" technique [56]. Depending on p_{T} and η, the overall reconstruction and selection efficiency is 50–80% for electrons and 75–85% for muons.

Jets are clustered from PF candidates using the anti-k_{T} jet algorithm with a distance parameter of 0.4 implemented in the FASTJET package [57, 58]. Charged PF candidates originating from a pileup interaction vertex are excluded. The total energy of the jets is corrected for energy depositions from pileup. In addition, p_{T}- and η-dependent corrections are applied to account for detector response effects [59]. If an isolated lepton with $p_{\mathrm{T}} > 15\,\mathrm{GeV}$ within $\Delta R = \sqrt{(\Delta\phi)^2 + (\Delta\eta)^2} = 0.4$ around a jet exists, the jet is assumed to represent the isolated lepton and is discarded to prevent counting the lepton momentum twice. The jets are considered for analysis if they fulfill the kinematic requirements $p_{\mathrm{T}} > 30\,\mathrm{GeV}$ and $|\eta| < 2.4$.

For the identification of b jets, the DeepJet algorithm [60, 61] is used. It is based on an artificial neural network (NN) that provides a discriminant to distinguish between b and other flavored jets. Jets are categorized based on three thresholds of the discriminant and a jet belongs to the category with the highest threshold that is smaller than that jet's discriminant value. The tight, medium, and loose thresholds have, depending on the jet p_{T} and η, efficiencies of about 50–70, 70–82, and 85–92%, respectively, and rejection probabilities of about 97, 85, and 55% for c jets and about 99.5, 98, and 90% for non-heavy-flavor jets.

The missing transverse momentum vector $\vec{p}_{\mathrm{T}}^{\mathrm{miss}}$ is computed as the negative vector sum of the transverse momenta of all the PF candidates in an event, and its magnitude is denoted as $p_{\mathrm{T}}^{\mathrm{miss}}$ [62]. The $\vec{p}_{\mathrm{T}}^{\mathrm{miss}}$ is modified to account for corrections to the energy scale of the reconstructed jets in the event.

The data was recorded in the years 2016–2018. For each year individual sets of simulations and correction factors are used according to the actual data-taking conditions and detector configurations. Because of significant changes in the detector configuration affecting the tracking efficiency, two separate sets of simulations and scale factors are used for 2016 data. Therefore, four different data-taking periods are analyzed.

6 Event reconstruction

The reconstruction of the $t\bar{t}$ system is performed using an artificial NN. The goal is the correct identification of detector-level objects as decay products of the leptonically (t_ℓ) and hadronically (t_h) decaying top quarks in e/μ+jets events. In the simulation, a quark or lepton at the generator level can be spatially matched to the corresponding detector-level object. Of the possible candidates, we select the highest p_T object within $\Delta R = 0.2$. If a one-to-one assignment to a corresponding detector-level object is possible for all of the particles in the generator-level $t\bar{t}$ system, the event is labeled "reconstructable", while all other e/μ+jets events are called "nonreconstructable".

The input layer of the NN is a vector encoding kinematical information about the detector-level objects and b tagging category for jets. The first four elements of the vector hold the four-momentum of the electron or muon ($p_x(\ell)$, $p_y(\ell)$, $p_z(\ell)$, $E(\ell)$), followed by (p_x^{miss}, p_y^{miss}). Finally, for up to eight jets the four-momentum and their b tagging category (p_x, p_y, p_z, E, b cat.) are stored. The NN is trained to assume the following order of the jets: the b jet in the decay of t_ℓ, the b jet in the decay of t_h, the down-type, and the up-type quark in the W boson decay. The remaining jets are added in descending order of their p_T. If there are fewer than eight jets, the rest of the input vector is filled with zeros. The b tagging information also helps to identify c jets from W boson decays, since 40–50% of the c jets are loosely b tagged. The input layer is followed by seven fully connected layers, each with 220 nodes and hyperbolic tangent as activation function. The output layer consists of a single node whose value is transformed by a sigmoid function into the range $[0, 1]$. In total, the network has about 300 000 parameters.

The NN is trained using about 20M simulated e/μ+jets events. Events with one selected electron or muon, no additional isolated electron or muon with $p_T > 15\,\text{GeV}$, and at least four jets are used. The NN is trained using a batch size of 128 events and the ADAM algorithm [63] for the minimization of the logistic loss function. For each event in a batch, the network is provided with all possible permutations for the four jets from the $t\bar{t}$ decay using up to eight jets per event, i.e., for 4 (5, 6, 7, 8) jets the training includes 24 (120, 360, 840, 1680) input vectors. Correct permutations are trained to have a response of one, while all other permutations should result in zero. The training sample includes "nonreconstructable" events, i.e., those with no correct permutation. During the training, the logistic loss function is monitored with a validation sample. The losses for the training and validation samples are compatible and no indication of overtraining is observed. During the inference, for each event, all possible permutations of assigning detector-level jets to the corresponding $t\bar{t}$ decay products are successively provided as input to the NN and the permutation resulting in the highest NN score S_{NN} is used.

For the selected permutation, the neutrino four-momentum p_ν is calculated using the W boson mass constraint $(p_\nu + p_\ell)^2 = m_W^2$, where $\vec{p}_T^{\,miss}$ is taken as the p_T of the neutrino. This constraint results in a quadratic equation for the longitudinal component of the neutrino momentum $p_z(\nu)$. If no real solution exists, the x and y components of $\vec{p}_T^{\,miss}$ are scaled separately to find a single solution under the condition of a minimum modification of p_T^{miss}, i.e., in the transverse plane we choose the point with the smallest distance from $\vec{p}_T^{\,miss}$ for which a solution exists. This modified $\vec{p}_T^{\,miss}$ together with the calculated solution for $p_z(\nu)$ form the neutrino momentum. If there are two solutions of the quadratic equation, the invariant mass $m(t_\ell)^2 = (p_\nu + p_\ell + p_{b_\ell})^2$ is calculated for both p_ν and the solution closer to m_t is selected.

To enhance the fraction of correctly reconstructed events and reduce the background contribution, event selection requirements on the reconstructed particle masses $|m(t_\ell) - 172.5\,\text{GeV}| < 50\,\text{GeV}$, $|m(t_h) - 172.5\,\text{GeV}| < 50\,\text{GeV}$, and $|m(W_h) - 80.4\,\text{GeV}| < 30\,\text{GeV}$ are imposed.

The distributions of S_{NN} are shown in Fig. 1 for events in categories where either both (2b) or exactly one (1b) of the jets identified as b jets from the $t\bar{t}$ decay are medium b tagged. In these distributions, it can be seen that the data and the prediction are in agreement within the uncertainty bands. We reject all events with $S_{NN} < 0.1$ due to the low fraction of correctly reconstructed events and the large contribution of background processes.

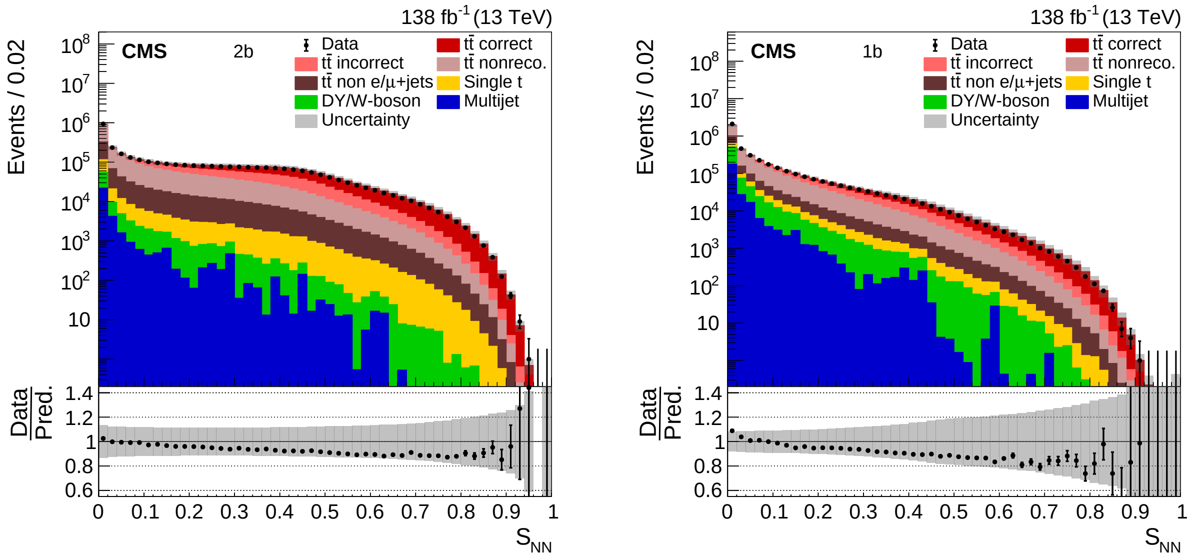

Figure 1: Distribution of S_{NN} in the 2b (left) and 1b (right) categories. The data (points) are compared to the prediction (stacked histograms). The $t\bar{t}$ contribution is split into the correctly and incorrectly reconstructed, "nonreconstructable", and non e/μ+jets events. The gray uncertainty band indicates the combined statistical and systematic uncertainties in the prediction, while the vertical bars on the points show the statistical uncertainty of the data. The ratios of data to the predicted yields are provided in the lower panels.

The 2b and 1b categories are further split based on the value of S_{NN}. In the 1b (2b) category events belong to the S_{high} category if $S_{NN} > 0.30$ (0.36), while the remaining events are placed in the S_{low} category. These requirements define the signal categories for the analysis and were systematically optimized to minimize the uncertainties in the expected spin polarization and correlation coefficients.

In the simulation, the fraction of reconstructable e/μ+jets events is 73% for 2b S_{high}, 47% for 2b S_{low}, 64% for 1b S_{high}, and 38% for 1b S_{low}. The fractions of correctly reconstructed events with respect to all signal and background events in the various categories are 46% for 2b S_{high}, 21% for 2b S_{low}, 37% for 1b S_{high}, and 15% for 1b S_{low}. Figure 2 shows these fractions as functions of $m(t\bar{t})$ together with the fraction of correctly reconstructed events with respect to all reconstructable events.

7 Background estimation

The main background contributions of non-$t\bar{t}$ events are expected from QCD multijet, DY, W boson, and single top quark production.

The shapes of the QCD multijet (multijet), and DY and W boson (EW) background distributions are estimated using a combined template of these backgrounds that is obtained from a b-jet depleted control region (CR). The simulation of these backgrounds suffers from large statistical uncertainties due to their high cross sections but low fraction of events that pass the

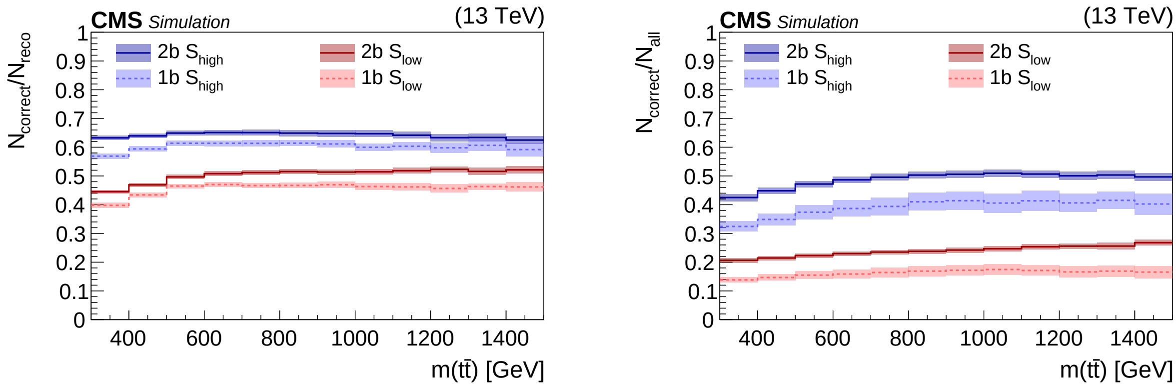

Figure 2: Reconstruction efficiency of the NN (left) and the fraction of correctly reconstructed events (right) as a function of $m(\mathrm{t\bar{t}})$ estimated from the simulation. The values are shown separately for the 1b and 2b categories with the S_{low} and S_{high} selections. The event counts N_{correct} and N_{reco} refer to the number of correctly reconstructed and "reconstructable" $\mathrm{t\bar{t}}$ events, respectively. All reconstructed events regardless of the process are labeled N_{all}. The uncertainty bands include all systematic uncertainties as detailed in Section 9.

selection. They contribute fractions of about 6.6% (1b S_{low}), 2.4% (1b S_{high}), 1.1% (2b S_{low}), and 0.2% (2b S_{high}), i.e., the contribution in the 2b categories is negligible. The shape of the background distribution is estimated by performing the NN reconstruction for events without any jet fulfilling the medium b tagging requirement. No selections on S_{NN} are applied, but the mass ranges of t_ℓ, $\mathrm{t_h}$, and the $\mathrm{W_h}$ boson are required as introduced in Section 6. These selection requirements define the CR. The expected contributions of $\mathrm{t\bar{t}}$ and single top quark events are subtracted from the data in the CR. The simulated kinematic distributions obtained in the CR are generally in agreement with the simulated distributions in the signal categories, as shown for the 1b signal category in Fig. 3.

As systematic uncertainties in the background template shapes, we evaluate shape differences between the CR and the signal categories. The definition of the CR is inclusive in S_{NN}. This choice has the advantage of maximizing the number of events in the CR while minimizing the contribution from $\mathrm{t\bar{t}}$ events. We obtain alternative shapes from additional control regions, where the S_{low} or S_{high} requirement of the corresponding signal category is also imposed. While it is expected that these distributions are more similar to the real background, they suffer from a small sample of events and large $\mathrm{t\bar{t}}$ contributions. Therefore, they are only used to evaluate the uncertainty in the background templates.

In the CR, there is an excess of about 20% in data. This excess is within the uncertainty in the simulated event yield. However, to take into account a possible underestimation of $\mathrm{t\bar{t}}$ production in the CR, an additional systematic uncertainty in the shape is obtained by scaling the amount of subtracted $\mathrm{t\bar{t}}$ and single top quark events by the ratio of the total observed and simulated event yields in the CR, shown as the dashed light blue lines in Fig. 3.

The predicted ratio of the multijet and EW event yield (multijet+EW) in each signal category to the corresponding CR is applied to normalize the background templates. This normalization factor has a large statistical uncertainty due to the limited number of simulated events in the signal categories. In addition, the observed differences between the predicted and observed event yields in the CR are considered as a systematic uncertainty in the normalization of the background. As a result, the normalization uncertainties can be as large as 50%, depending on the category.

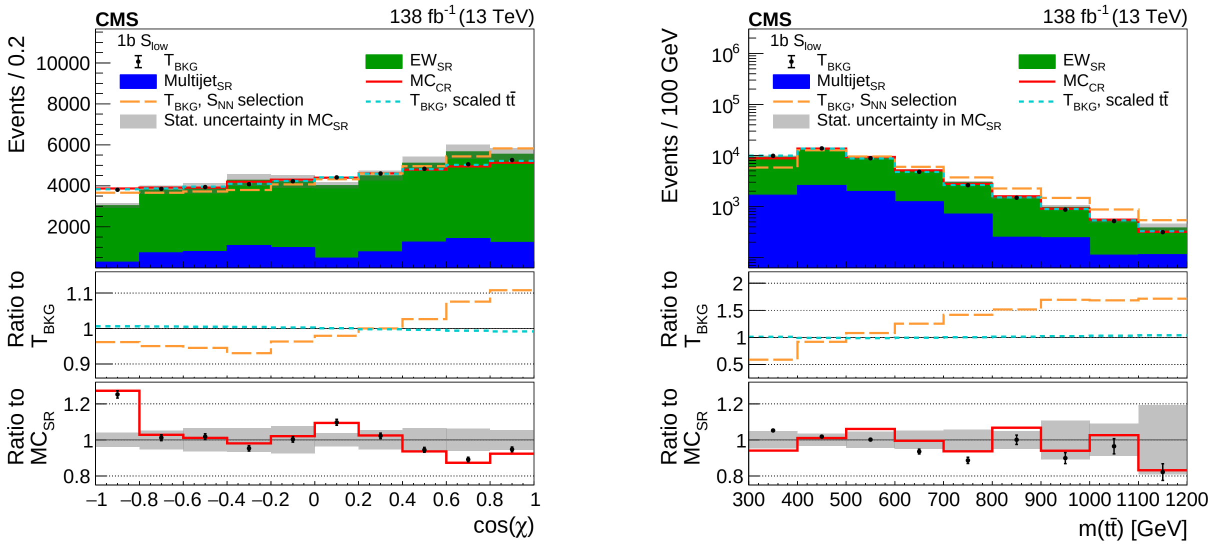

Figure 3: Comparison of the $\cos(\chi)$ (left) and $m(\mathrm{t\bar{t}})$ (right) distributions of the simulated background in the control region ($\mathrm{MC_{CR}}$) shown as the red line, and in the 1b S_{low} signal region ($\mathrm{MC_{SR}}$) shown as the stacked histograms of the multijet and EW components. The estimated background template ($\mathrm{T_{BKG}}$) shown as black markers corresponds to the data distribution in the CR after subtracting the predicted $\mathrm{t\bar{t}}$ and single top quark contributions. Variations of the $\mathrm{T_{BKG}}$ are obtained applying the additional S_{NN} selection for the 1b S_{low} category (orange line) and by taking into account the mismatch of the normalization in the CR when subtracting the $\mathrm{t\bar{t}}$ and single top quark contributions (blue line). All distributions are normalized to the event yields predicted by the $\mathrm{MC_{SR}}$. The gray uncertainty band shows the statistical uncertainties in the $\mathrm{MC_{SR}}$. The middle panels show the relative effects of the $\mathrm{T_{BKG}}$ variations. The lower panels show the ratio of the $\mathrm{MC_{CR}}$ and the $\mathrm{T_{BKG}}$ to the $\mathrm{MC_{SR}}$.

The obtained background predictions with their shape and normalization uncertainties are included in the fits of spin polarization and correlation coefficients, as described in Section 8. The normalization uncertainties are treated as uncorrelated among all categories, because of their large statistical component from the simulation. The shape uncertainties are considered as uncorrelated among the categories to account for differences in their selection. In addition, the uncertainties are assumed uncorrelated among the data-taking periods, because of the differences in the b tagging performances and selections. It has been verified that the results of the analysis are not sensitive to these assumptions.

The contribution of single top quark production is about 4.0% (1b S_{low}), 2.2% (1b S_{high}), 2.4% (2b S_{low}), and 1.4% (2b S_{high}). Templates according to their SM expectation are taken from the simulation. We evaluate the relevant uncertainties in these templates (as described in Section 9): ME and PS scales, jet resolution and energy scales, and b tagging and lepton efficiencies. The ME scale uncertainties are treated independently from the corresponding variations of the $\mathrm{t\bar{t}}$ simulation.

In Figs. 4–9, the distributions of several observables in all signal categories are shown with the multijet+EW background estimation taken from the CR. The uncertainty bands include statistical uncertainties and all systematic uncertainties detailed in Section 9, and are in general dominated by uncertainties in the jet energy scale.

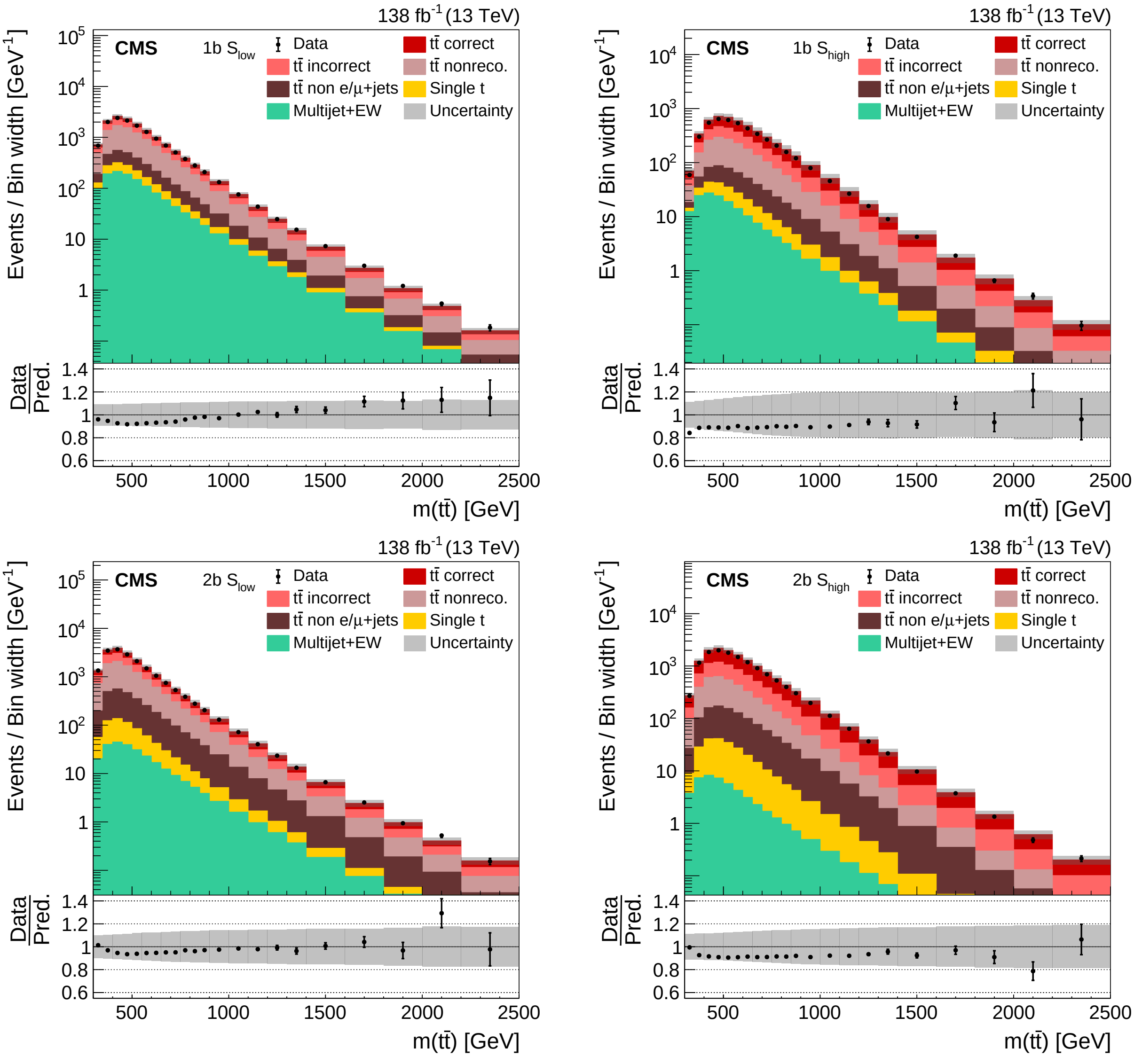

Figure 4: Distribution of $m(t\bar{t})$ in all four categories. The data (points) are compared to the prediction (stacked histograms). The $t\bar{t}$ and single top quark contributions are taken from the simulation, while the multijet+EW background is obtained from the CR. The $t\bar{t}$ contribution is split into the correctly and incorrectly reconstructed, "nonreconstructable", and non e/μ+jets events. The gray uncertainty band indicates the combined statistical and systematic uncertainties in the prediction. The vertical bars on the points show the statistical uncertainty of the data. Ratios to the predicted yields are provided in the lower panels.

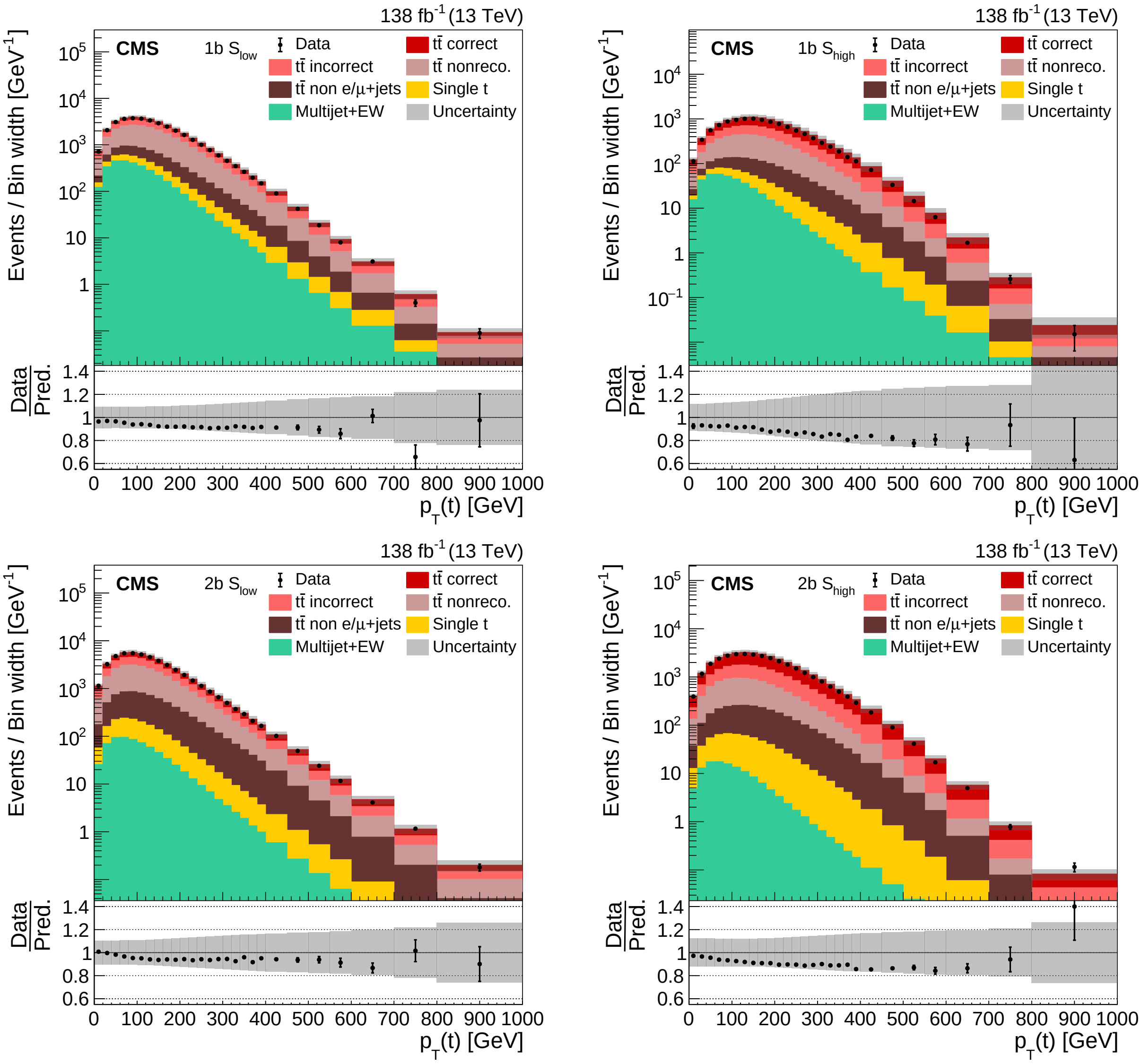

Figure 5: Distribution of $p_{\mathrm{T}}(\mathrm{t})$ in all four categories. The data (points) are compared to the prediction (stacked histograms). The $\mathrm{t\bar{t}}$ and single top quark contributions are taken from the simulation, while the multijet+EW background is obtained from the CR. The $\mathrm{t\bar{t}}$ contribution is split into the correctly and incorrectly reconstructed, “nonreconstructable”, and non e/μ+jets events. The gray uncertainty band indicates the combined statistical and systematic uncertainties in the prediction. The vertical bars on the points show the statistical uncertainty of the data. Ratios to the predicted yields are provided in the lower panels.

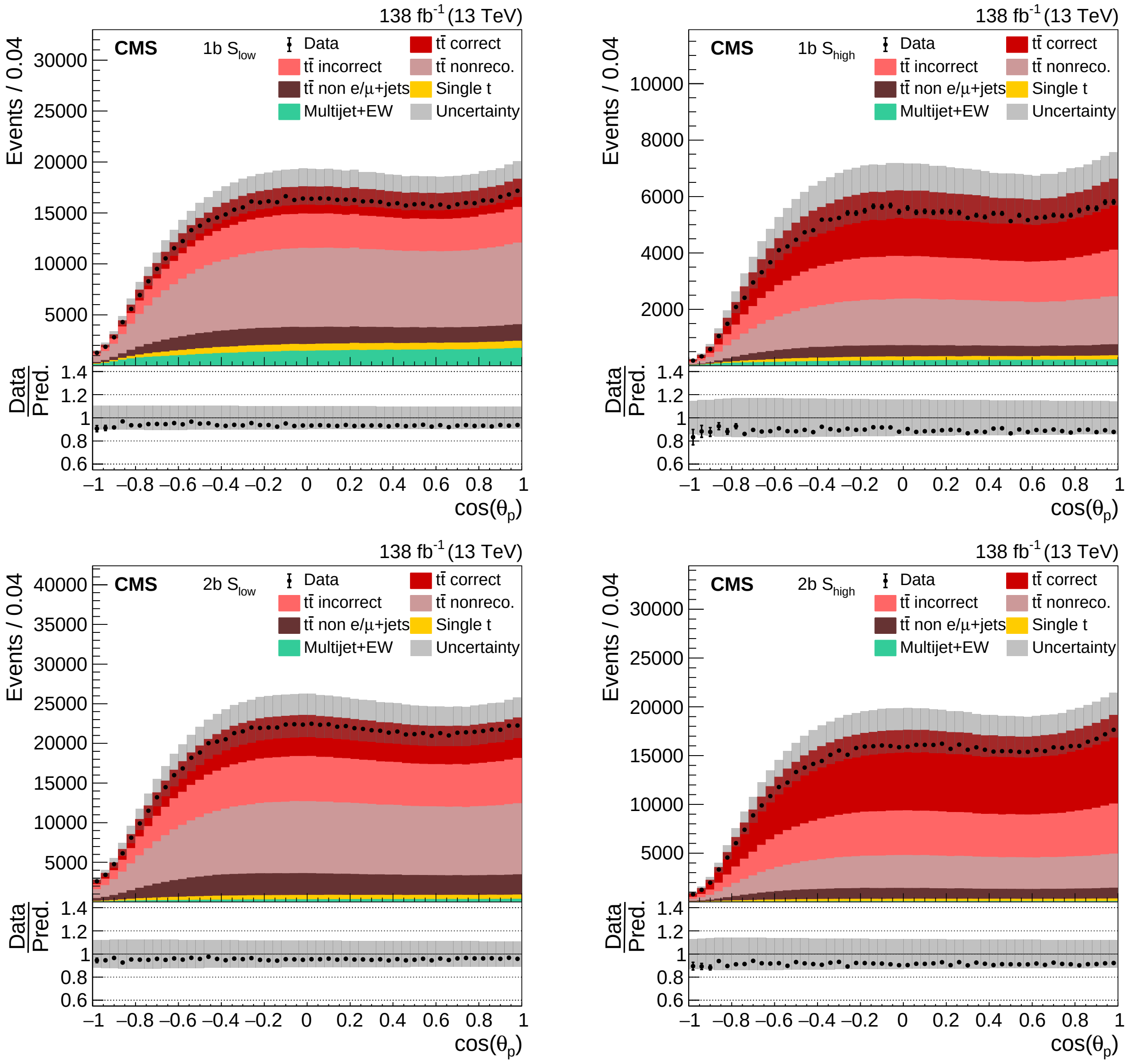

Figure 6: Distribution of $\cos(\theta_{\mathrm{p}})$ in all four categories. The data (points) are compared to the prediction (stacked histograms). The $\mathrm{t\bar{t}}$ and single top quark contributions are taken from the simulation, while the multijet+EW background is obtained from the CR. The $\mathrm{t\bar{t}}$ contribution is split into the correctly and incorrectly reconstructed, "nonreconstructable", and non e/μ+jets events. The gray uncertainty band indicates the combined statistical and systematic uncertainties in the prediction. The vertical bars on the points show the statistical uncertainty of the data. Ratios to the predicted yields are provided in the lower panels.

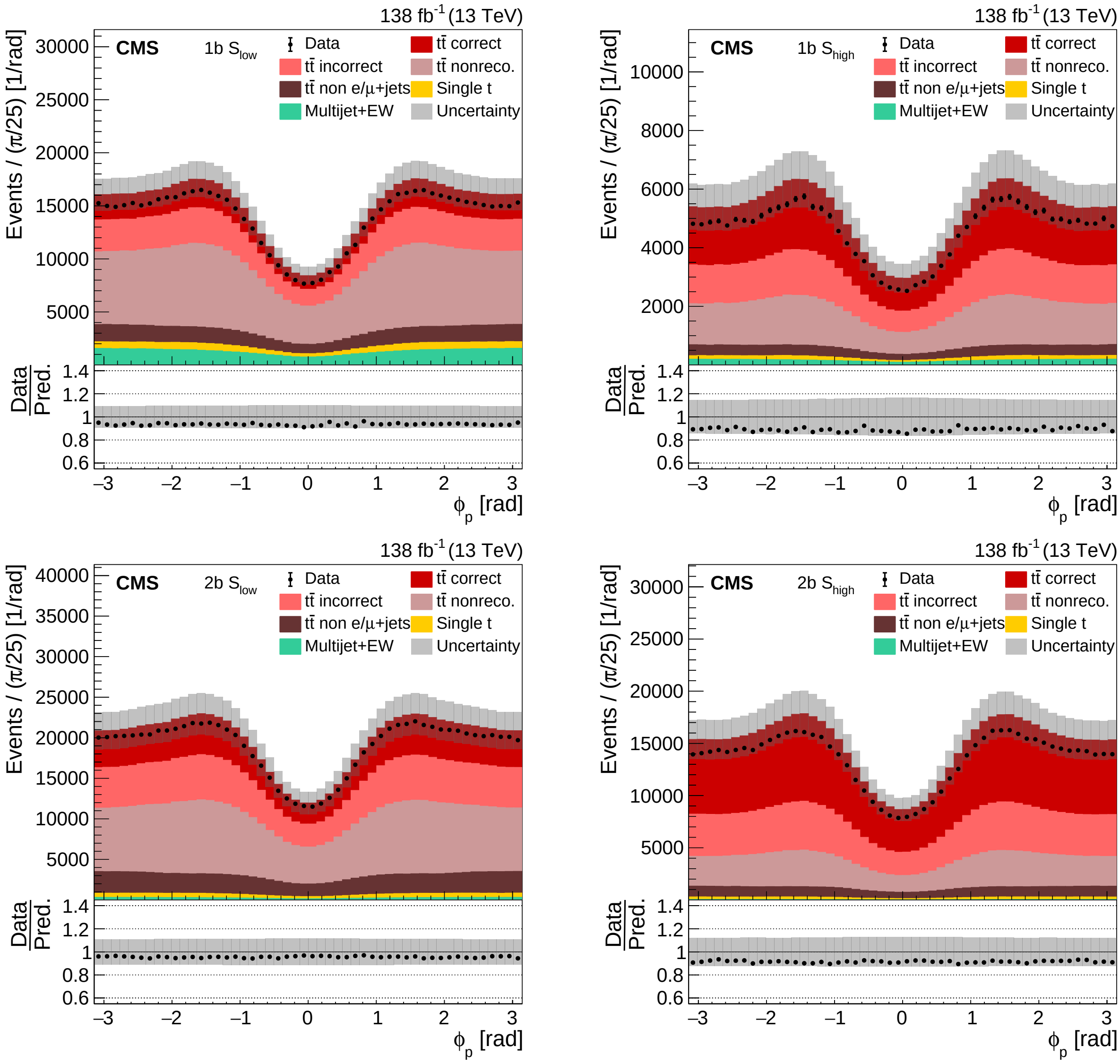

Figure 7: Distribution of ϕ_{p} in all four categories. The data (points) are compared to the prediction (stacked histograms). The $\mathrm{t\bar{t}}$ and single top quark contributions are taken from the simulation, while the multijet+EW background is obtained from the CR. The $\mathrm{t\bar{t}}$ contribution is split into the correctly and incorrectly reconstructed, "nonreconstructable", and non e/μ+jets events. The gray uncertainty band indicates the combined statistical and systematic uncertainties in the prediction. The vertical bars on the points show the statistical uncertainty of the data. Ratios to the predicted yields are provided in the lower panels.

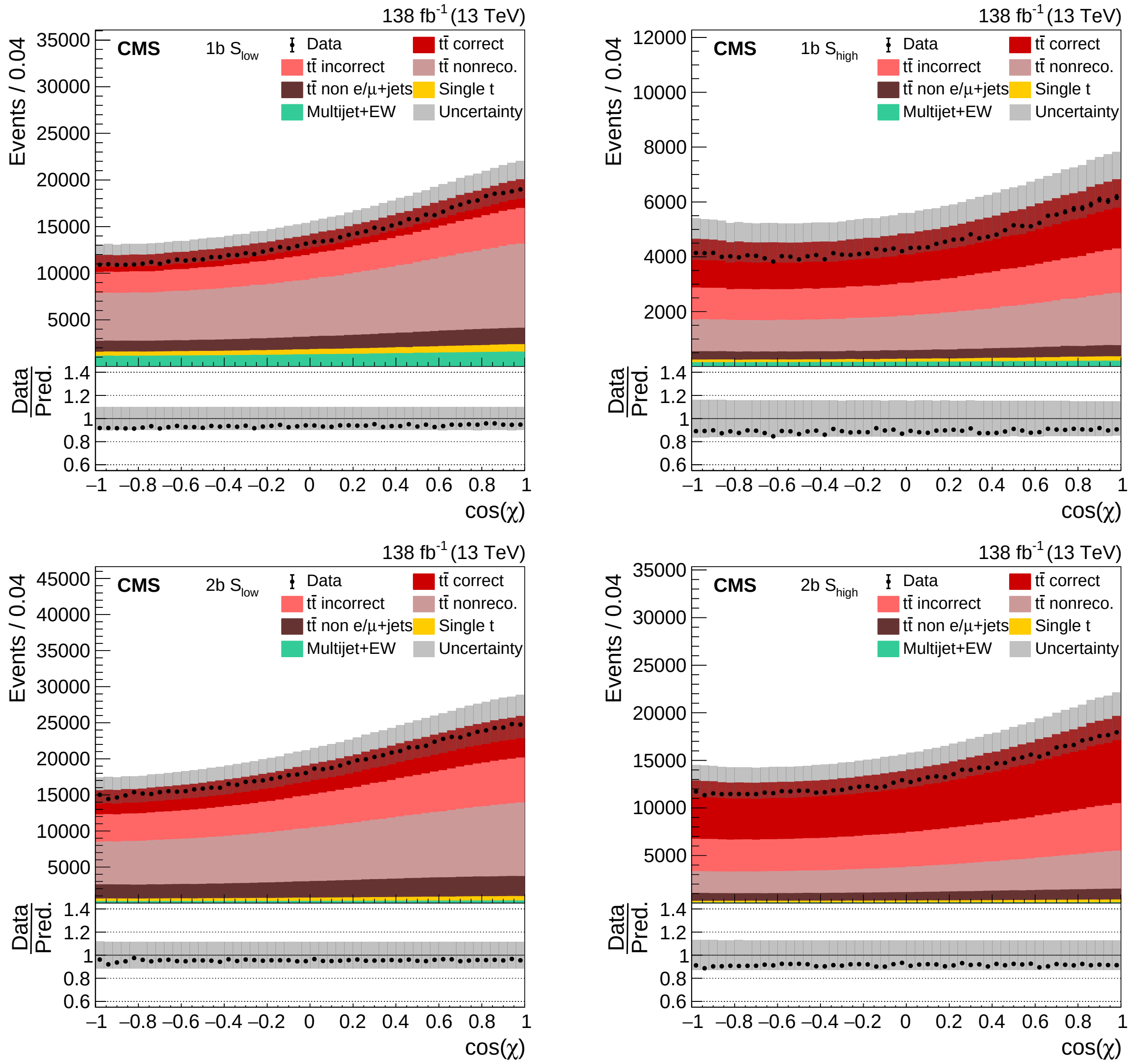

Figure 8: Distribution of $\cos(\chi)$ in all four categories. The data (points) are compared to the prediction (stacked histograms). The $t\bar{t}$ and single top quark contributions are taken from the simulation, while the multijet+EW background is obtained from the CR. The $t\bar{t}$ contribution is split into the correctly and incorrectly reconstructed, "nonreconstructable", and non e/μ+jets events. The gray uncertainty band indicates the combined statistical and systematic uncertainties in the prediction. The vertical bars on the points show the statistical uncertainty of the data. Ratios to the predicted yields are provided in the lower panels.

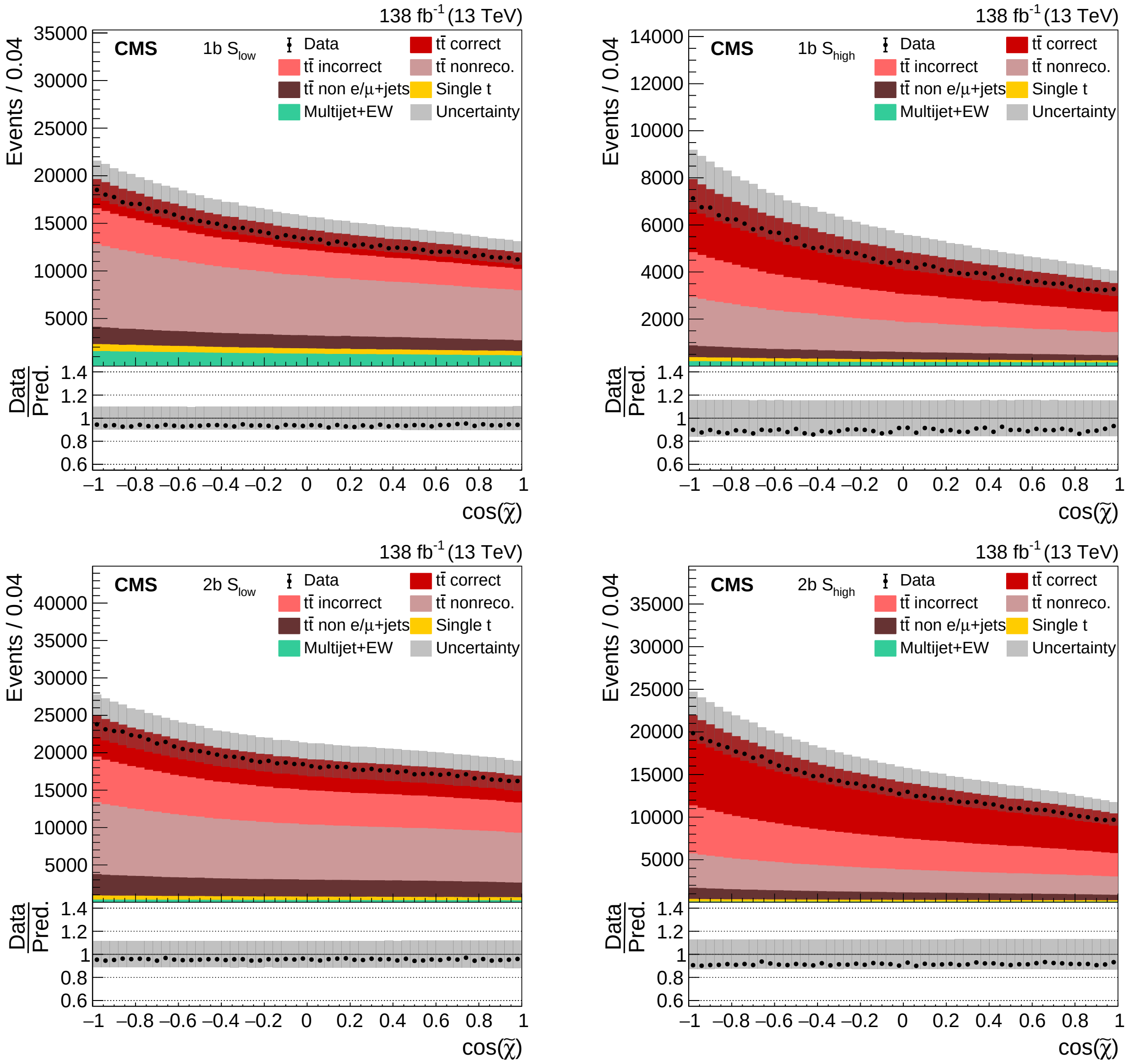

Figure 9: Distribution of $\cos(\tilde{\chi})$ in all four categories. The data (points) are compared to the prediction (stacked histograms). The $t\bar{t}$ and single top quark contributions are taken from the simulation, while the multijet+EW background is obtained from the CR. The $t\bar{t}$ contribution is split into the correctly and incorrectly reconstructed, "nonreconstructable", and non e/μ+jets events. The gray uncertainty band indicates the combined statistical and systematic uncertainties in the prediction. The vertical bars on the points show the statistical uncertainty of the data. Ratios to the predicted yields are provided in the lower panels.

8 Extraction of polarization and spin correlation coefficients

Following the formalism introduced in Eq. (4), the differential cross section Σ_{tot} can be written as a linear combination of functions Σ_m, which depend on the angles $\phi_{\text{p}(\bar{\text{p}})}$ and $\theta_{\text{p}(\bar{\text{p}})}$ of the decay products of the top quark and antiquark:

$$\Sigma_{\text{tot}} = \Sigma_0 + \sum_{m=1}^{15} Q_m \Sigma_m. \tag{10}$$

The spin analyzing powers κ and the cross section σ_{norm} are absorbed in the definitions of the functions Σ_m.

The values of the coefficients Q_m can be extracted by fitting Σ_{tot} with Eq. (10). This approach is used at the generator level to obtain the Q_m^{MC}—the polarization and spin correlation of the partonic top quarks as predicted by each of the $\text{t}\bar{\text{t}}$ simulations and their uncertainty variations. These fits are performed in bins of the additional observables $m(\text{t}\bar{\text{t}})$ *vs.* $|\cos(\theta)|$ and $p_{\text{T}}(\text{t})$ *vs.* $|\cos(\theta)|$. A binning in $m(\text{t}\bar{\text{t}})$ of $\{300, 400, 600, 800, 13000\}$ GeV with the first $m(\text{t}\bar{\text{t}})$ bin including a few underflow events, and in $p_{\text{T}}(\text{t})$ of $\{0, 100, 200, 300, 6500\}$ GeV is used. In both cases the bins are further divided into $|\cos(\theta)|$ bins with the boundaries $\{0, 0.4, 0.7, 1\}$. As a result we obtain the average values of the Q_m^{MC} in each of these bins. The knowledge of the Q_m^{MC} facilitates the analytical calculation of $\Sigma_{\text{tot}}^{\text{MC}}$ as a function of $\phi_{\text{p}(\bar{\text{p}})}$ and $\theta_{\text{p}(\bar{\text{p}})}$ in each bin of the additional observables.

For the measurement of the Q_m, we are interested in templates T_m that can be fit to the data and describe only the effect of the corresponding coefficient. At the generator level, these templates are $L\Sigma_m$, where L is the integrated luminosity. Accordingly, the T_m are the corresponding distributions of events at the detector level in the signal categories. The binnings at the generator and the detector levels are the same. The T_m include all $\text{t}\bar{\text{t}}$ events selected at the detector level, meaning that they describe polarization and spin correlation effects of e/μ+jets and all other $\text{t}\bar{\text{t}}$ events, also referred as $\text{t}\bar{\text{t}}$ non e/μ+jets. To avoid the full simulation of $\text{t}\bar{\text{t}}$ samples for each Q_m we use a reweighting technique to evaluate the T_m. For this, each event is assigned a weight equal to $\Sigma_m/\Sigma_{\text{tot}}^{\text{MC}}$, which are evaluated for each event based on the generator-level values of $\theta_{\text{p}(\bar{\text{p}})}$, $\phi_{\text{p}(\bar{\text{p}})}$, and the bin determined by the additional observables $m(\text{t}\bar{\text{t}})$ *vs.* $|\cos(\theta)|$ or $p_{\text{T}}(\text{t})$ *vs.* $|\cos(\theta)|$. In this bin we know the average value of the Q_m^{MC}, as determined from the fits of the Σ_m at the generator level. The generator-level Σ_m and the T_m for the 2b S_{high} category at the detector level are shown in Fig. 10. Here, the x axis shows the bin number of the unrolled 4-dimensional distribution of $\phi_{\bar{\text{p}}}$, $\cos(\theta_{\bar{\text{p}}})$, ϕ_{p}, and $\cos(\theta_{\text{p}})$, listed from the outermost to the innermost variable, where $\cos(\theta_{\text{p}(\bar{\text{p}})})$ uses two bins: $\{-1, 0, 1\}$, and $\phi_{\text{p}(\bar{\text{p}})}$ is divided into four bins: $\{-\pi, -\pi/2, 0, \pi/2, \pi\}$, resulting in a total number of 64 bins.

In general, the Q_m are not constant within a bin. At the generator level, the functions Σ_m do not depend on the kinematic properties of the top quarks, so they factorize and the average values of the Q_m are fitted in each bin. However, at the detector level, the T_m do change as a function of the top quark and antiquark kinematic properties due to selection requirements and detector effects. Therefore, it is important to perform the measurements in sufficiently small bins such that either the Q_m or the T_m are approximately constant within each bin. If the T_m vary significantly within a fitted bin, the measured Q_m could be biased if the values of the coefficients change within a bin in a different way than in the SM simulation. The binnings in $m(\text{t}\bar{\text{t}})$ *vs.* $|\cos(\theta)|$ and $p_{\text{T}}(\text{t})$ *vs.* $|\cos(\theta)|$ were selected to minimize the bias due to nonconstant T_m templates within the bins. The way the templates are constructed ensures that a template fit to the SM prediction extracts the correct Q_m, i.e., the bias is minimized for SM-like data.

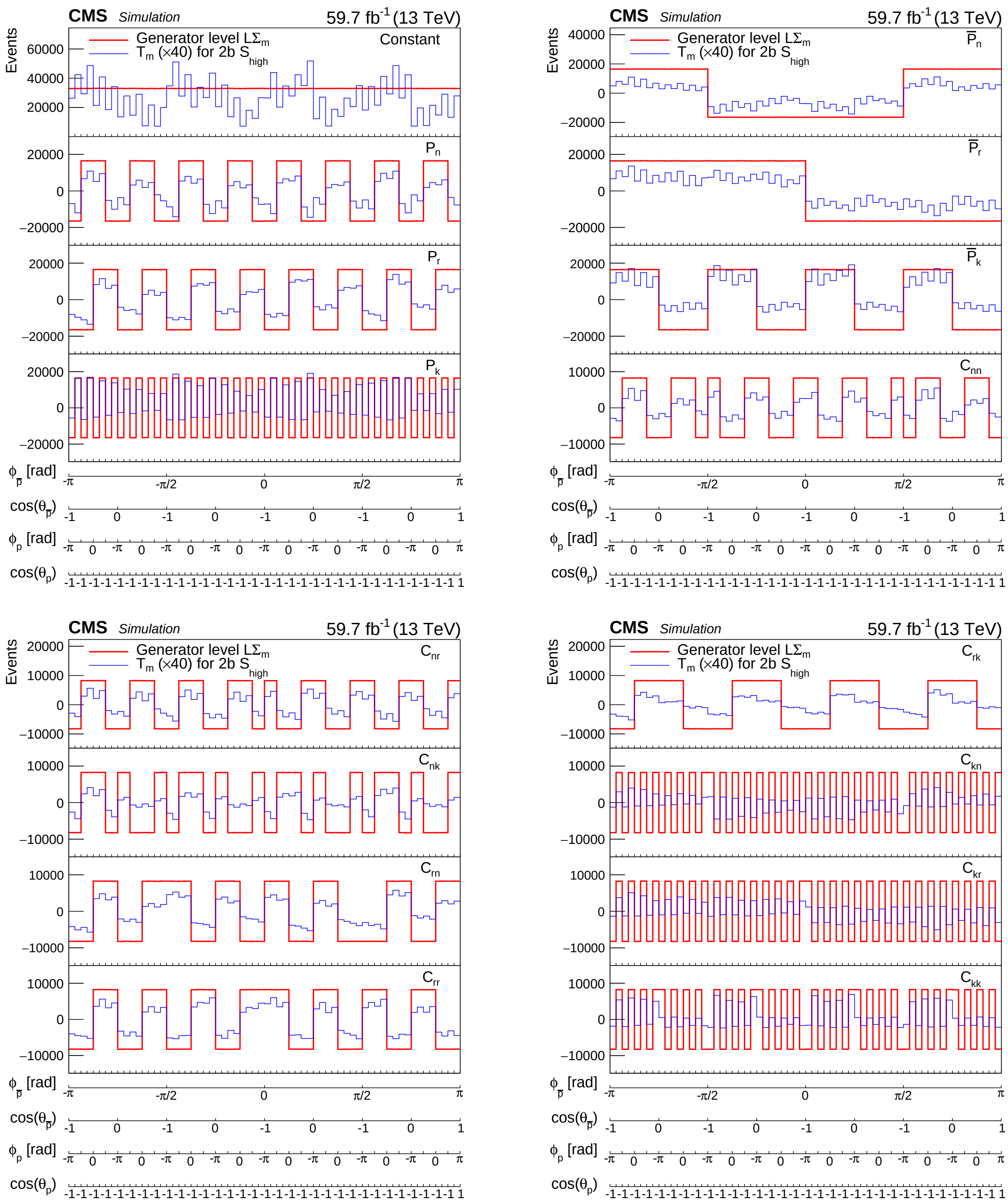

Figure 10: Examples of unrolled 4-dimensional distributions $L\Sigma_m$ and T_m as functions of $\phi_{\mathrm{p}(\bar{\mathrm{p}})}$ and $\theta_{\mathrm{p}(\bar{\mathrm{p}})}$ for the individual coefficients of the polarization vectors and the spin correlation matrix for events with $400 < m(\mathrm{t\bar{t}}) < 600\,\mathrm{GeV}$ and $|\cos(\theta)| < 0.4$. The $L\Sigma_m$ (red lines) are the distributions at the generator level in the full phase space, and the T_m (blue lines) are the distributions in the 2b S_{high} category for the 2018 data. For the purpose of illustration, the events are required to be reconstructed and generated in the same $m(\mathrm{t\bar{t}})$ *vs.* $|\cos(\theta)|$ bin. The detector-level distributions are enhanced by a factor of 40 to improve their visibility.

The same reweighting procedure is used for the D and $\tilde{D}$ measurements, but decomposing the distribution of $\cos(\chi)$ and $\cos(\tilde{\chi})$ into constant and linear terms as given by Eq. (6). In these cases we use 10 equally sized bins in $\cos(\chi)$, and $\cos(\tilde{\chi})$ for all measurements. A finer binning in $m(\mathrm{t\bar{t}})$ of $\{300, 400, 500, 600, 700, 800, 900, 1000, 13000\}$ GeV and $p_{\mathrm{T}}(\mathrm{t})$ of $\{0, 50, 100, 150, 200, 250, 300, 400, 6500\}$ GeV is selected for the D and $\tilde{D}$ measurements.

We perform a maximum likelihood fit combining the information of the four selections (2b S_{high}, 2b S_{low}, 1b S_{high}, 1b S_{low}) in the four data-taking periods, for a total of 16 categories. The statistical model describes the total number of events in each bin

$$N_{ij'n'}(a_n, \{Q_{mn}\}, \{\nu_k\}) = S_{ij'n'}(a_n, \{Q_{mn}\}, \{\nu_k\}) + B_{ij'n'}(\{\nu_k\}), \tag{11}$$

with i denoting the category and j' referring to a bin in the 1-dimensional concatenated detector-level distribution of $\phi_{\mathrm{p}(\bar{\mathrm{p}})}$ and $\theta_{\mathrm{p}(\bar{\mathrm{p}})}$. The index n' (n) refers to a bin of the $m(\mathrm{t\bar{t}})$ *vs.* $|\cos(\theta)|$ or $p_{\mathrm{T}}(\mathrm{t})$ *vs.* $|\cos(\theta)|$ distribution at the detector (generator) level. The normalization parameters a_n and the Q_{mn} (or D_n, $\tilde{D}_n$) are defined separately for each bin n and are free parameters in the fit. The $S_{ij'n'}$ and $B_{ij'n'}$ are the $\mathrm{t\bar{t}}$ and background contributions, respectively, and both can depend on the nuisance parameters $\{\nu_k\}$ modeling the variation of the expected event yields due to systematic uncertainties. The $\mathrm{t\bar{t}}$ contribution takes the form

$$S_{ij'n'}(a_n, \{Q_{mn}\}, \{\nu_k\}) = \sum_n a_n \left(T_{i0nj'n'}(\{\nu_k\}) + \sum_{m=1}^{15} Q_{mn} T_{imnj'n'}(\{\nu_k\}) \right), \tag{12}$$

where $T_{imnj'n'}$ are the detector-level distributions (templates) obtained by reweighting the $\mathrm{t\bar{t}}$ simulation to the individual components proportional to the Q_{mn} and the templates $T_{i0nj'n'}$ correspond to the constant terms. Finally, the function

$$-2\log\Big(L(a_n, \{Q_{mn}\}, \{\nu_k\})\Big) = -2\sum_{ij'n'} \Big[d_{ij'n'} \log\Big(N_{ij'n'}(a_n, \{Q_{mn}\}, \{\nu_k\})\Big) - N_{ij'n'}(a_n, \{Q_{mn}\}, \{\nu_k\}) \Big] - 2\log\Big(G(\{\nu_k\})\Big) \tag{13}$$

is minimized with respect to the value of the parameters a_n, Q_{mn}, and ν_k. Here, $d_{ij'n'}$ are the observed event yields and $G(\{\nu_k\})$ describes the Gaussian constraints of the ν_k. Goodness of fit tests indicate good agreement between the data and the fitted model with p-values [64] of 0.80–0.95 for all fits. We tested that the Gaussian approximation can be used to describe the distributions of the uncertainties in the measured parameters. This allows us to use Gaussian error propagation when evaluating quantities derived from the measured parameters.

In Figs. 11–12, the pre- and post-fit distributions are shown for the full matrix measurement in the 2b S_{high} category. The pre-fit model uses the POWHEG+PYTHIA predictions. In addition, a model without any polarization and spin correlation is shown as a blue line to demonstrate those effects. The 2b S_{high} category is shown here as an example since it is the category with the largest effects from polarization and spin correlation. The agreement between the data and the model is very similar in the other categories.

The same strategy is used to extract D_n ($\tilde{D}_n$) directly. In this case, j' represents a bin of $\cos(\chi)$ ($\cos(\tilde{\chi})$). The pre- and post-fit distributions in the 2b S_{high} category of the D and $\tilde{D}$ measurements in bins of $m(\mathrm{t\bar{t}})$ *vs.* $|\cos(\theta)|$ are presented in Figs. 13–16, respectively. The post-fit model describes the data well and no significant deviations are observed in any of the $m(\mathrm{t\bar{t}})$ *vs.* $|\cos(\theta)|$ or $p_{\mathrm{T}}(\mathrm{t})$ *vs.* $|\cos(\theta)|$ bins.

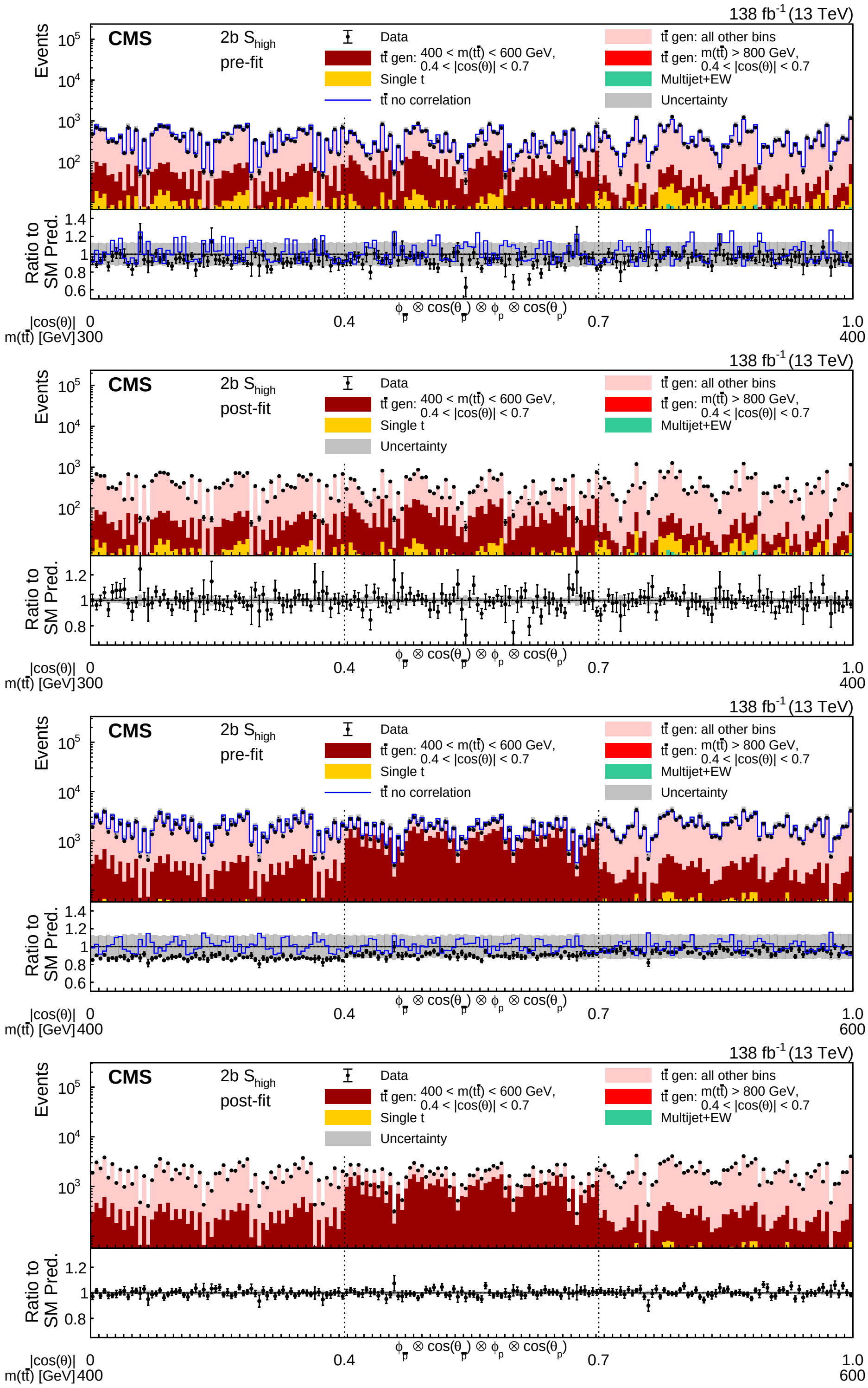

Figure 11: Pre- and post-fit distributions comparing the data (points) to the POWHEG+PYTHIA simulation (stacked histograms) for the full matrix measurement in bins of $m(\mathrm{t\bar{t}})$ *vs.* $|\cos(\theta)|$ in the 2b S_{high} category. The x axis shows the bins of the unrolled 4-dimensional distribution of $\phi_{\bar{\mathrm{p}}}$, $\cos(\theta_{\bar{\mathrm{p}}})$, ϕ_{p}, and $\cos(\theta_{\mathrm{p}})$, listed from the outermost to the innermost variable in each of the $m(\mathrm{t\bar{t}})$ *vs.* $|\cos(\theta)|$ bins. The boundaries of the $|\cos(\theta)|$ and $m(\mathrm{t\bar{t}})$ bins are labeled and indicated by dashed and solid lines, respectively. For the illustration of resolution effects, $\mathrm{t\bar{t}}$ events generated in two selected $m(\mathrm{t\bar{t}})$ *vs.* $|\cos(\theta)|$ bins are shown in different shades of red. All other $\mathrm{t\bar{t}}$ contributions are shown in pink. A model without any polarization and spin correlation is shown as a blue line. The gray uncertainty band indicates the combined statistical and systematic uncertainties in the prediction. The vertical bars on the points show the statistical uncertainty. Ratios to the predicted yields are provided in the lower panels.

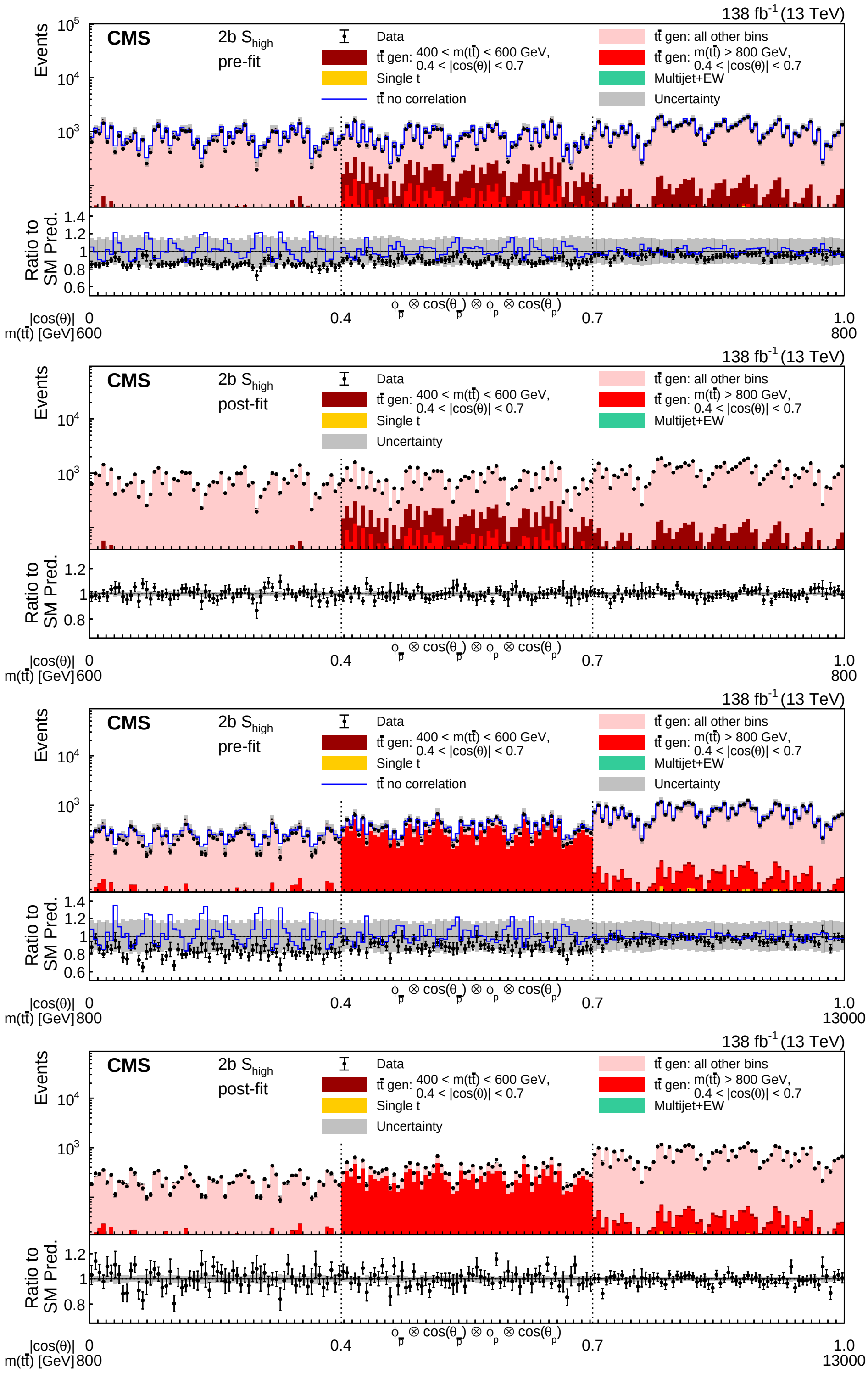

Figure 12: Pre- and post-fit distributions comparing the data (points) to the POWHEG+PYTHIA simulation (stacked histograms) for the full matrix measurement in bins of $m(t\bar{t})$ *vs.* $|\cos(\theta)|$ in the 2b S_{high} category. The x axis shows the bins of the unrolled 4-dimensional distribution of $\phi_{\bar{p}}$, $\cos(\theta_{\bar{p}})$, ϕ_{p}, and $\cos(\theta_{p})$, listed from the outermost to the innermost variable in each of the $m(t\bar{t})$ *vs.* $|\cos(\theta)|$ bins. The boundaries of the $|\cos(\theta)|$ and $m(t\bar{t})$ bins are labeled and indicated by dashed and solid lines, respectively. For the illustration of resolution effects, $t\bar{t}$ events generated in two selected $m(t\bar{t})$ *vs.* $|\cos(\theta)|$ bins are shown in different shades of red. All other $t\bar{t}$ contributions are shown in pink. A model without any polarization and spin correlation is shown as a blue line. The gray uncertainty band indicates the combined statistical and systematic uncertainties in the prediction. The vertical bars on the points show the statistical uncertainty. Ratios to the predicted yields are provided in the lower panels.

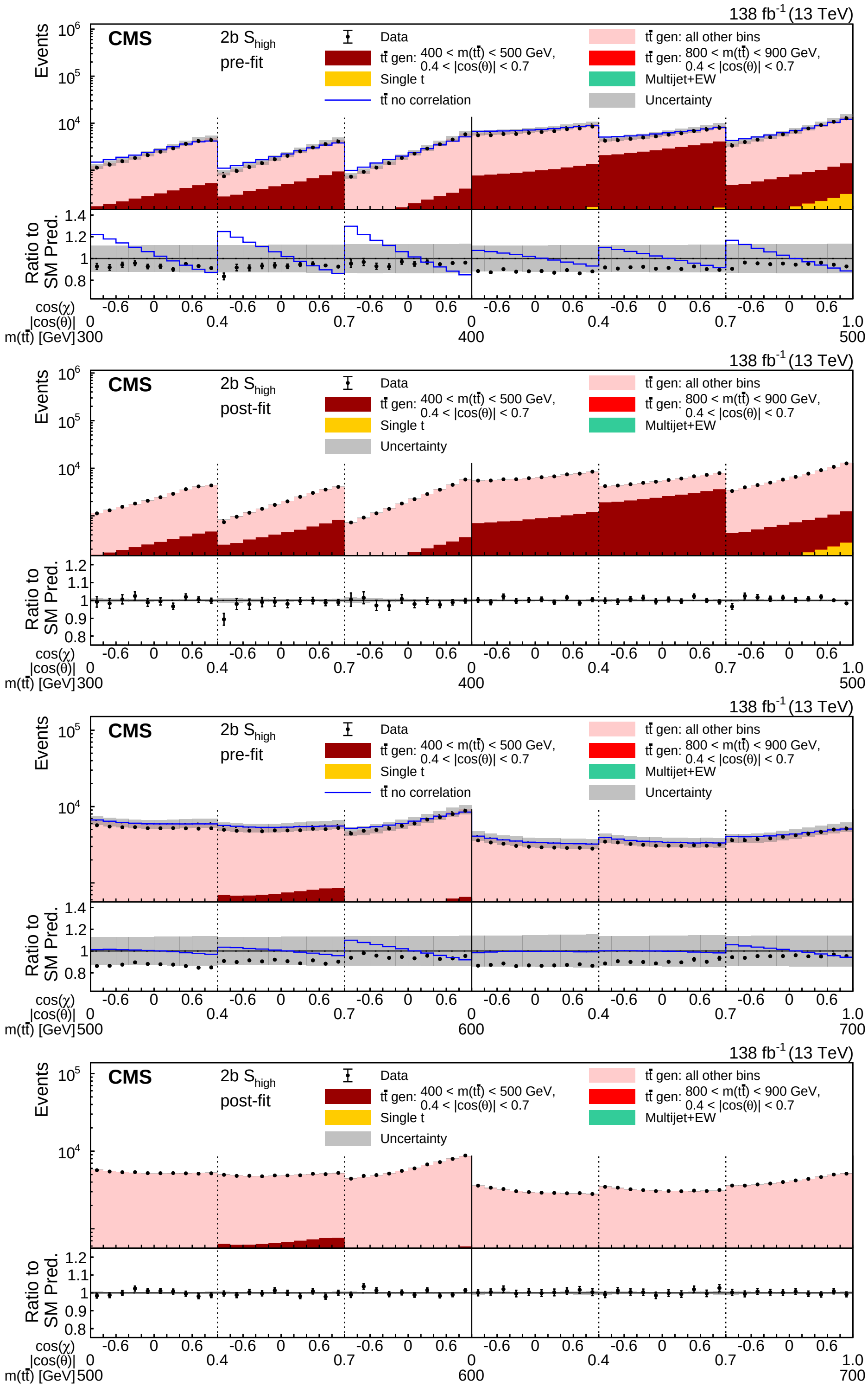

Figure 13: Pre- and post-fit distributions of $\cos(\chi)$ comparing the data (points) to the POWHEG+PYTHIA simulation (stacked histograms) for the D measurement in bins of $m(\mathrm{t\bar{t}})$ *vs.* $|\cos(\theta)|$ in the 2b S_{high} category. The boundaries of the $|\cos(\theta)|$ and $m(\mathrm{t\bar{t}})$ bins are labeled and indicated by dashed and solid lines, respectively. For the illustration of resolution effects, $\mathrm{t\bar{t}}$ events generated in two selected $m(\mathrm{t\bar{t}})$ *vs.* $|\cos(\theta)|$ bins are shown in different shades of red. All other $\mathrm{t\bar{t}}$ contributions are shown in pink. A model without any polarization and spin correlation is shown as a blue line. The gray uncertainty band indicates the combined statistical and systematic uncertainties in the prediction. The vertical bars on the points show the statistical uncertainty. Ratios to the predicted yields are provided in the lower panels.

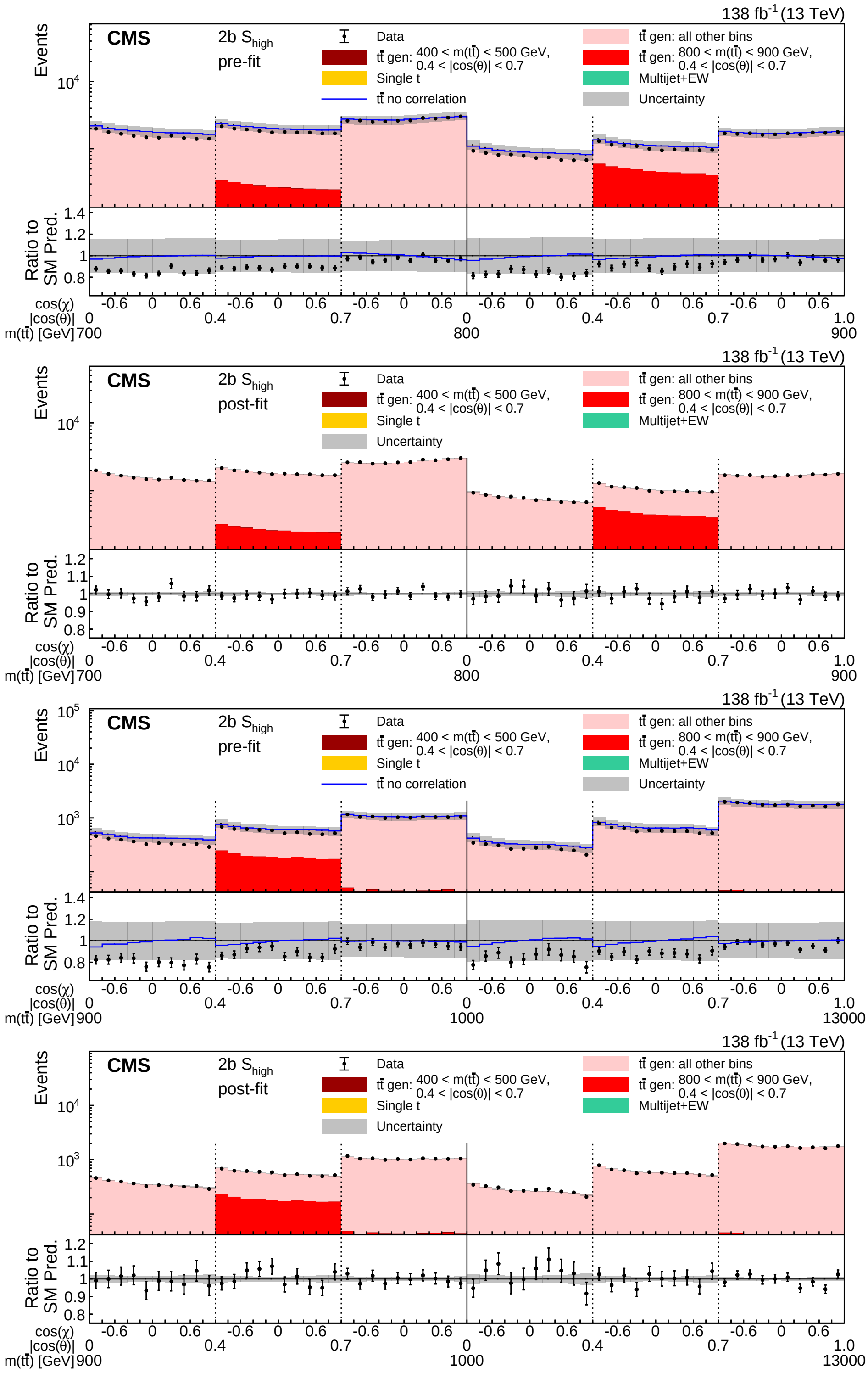

Figure 14: Pre- and post-fit distributions of $\cos(\chi)$ comparing the data (points) to the POWHEG+PYTHIA simulation (stacked histograms) for the D measurement in bins of $m(\mathrm{t\bar{t}})$ *vs.* $|\cos(\theta)|$ in the 2b S_{high} category. The boundaries of the $|\cos(\theta)|$ and $m(\mathrm{t\bar{t}})$ bins are labeled and indicated by dashed and solid lines, respectively. For the illustration of resolution effects, $\mathrm{t\bar{t}}$ events generated in two selected $m(\mathrm{t\bar{t}})$ *vs.* $|\cos(\theta)|$ bins are shown in different shades of red. All other $\mathrm{t\bar{t}}$ contributions are shown in pink. A model without any polarization and spin correlation is shown as a blue line. The gray uncertainty band indicates the combined statistical and systematic uncertainties in the prediction. The vertical bars on the points show the statistical uncertainty. Ratios to the predicted yields are provided in the lower panels.

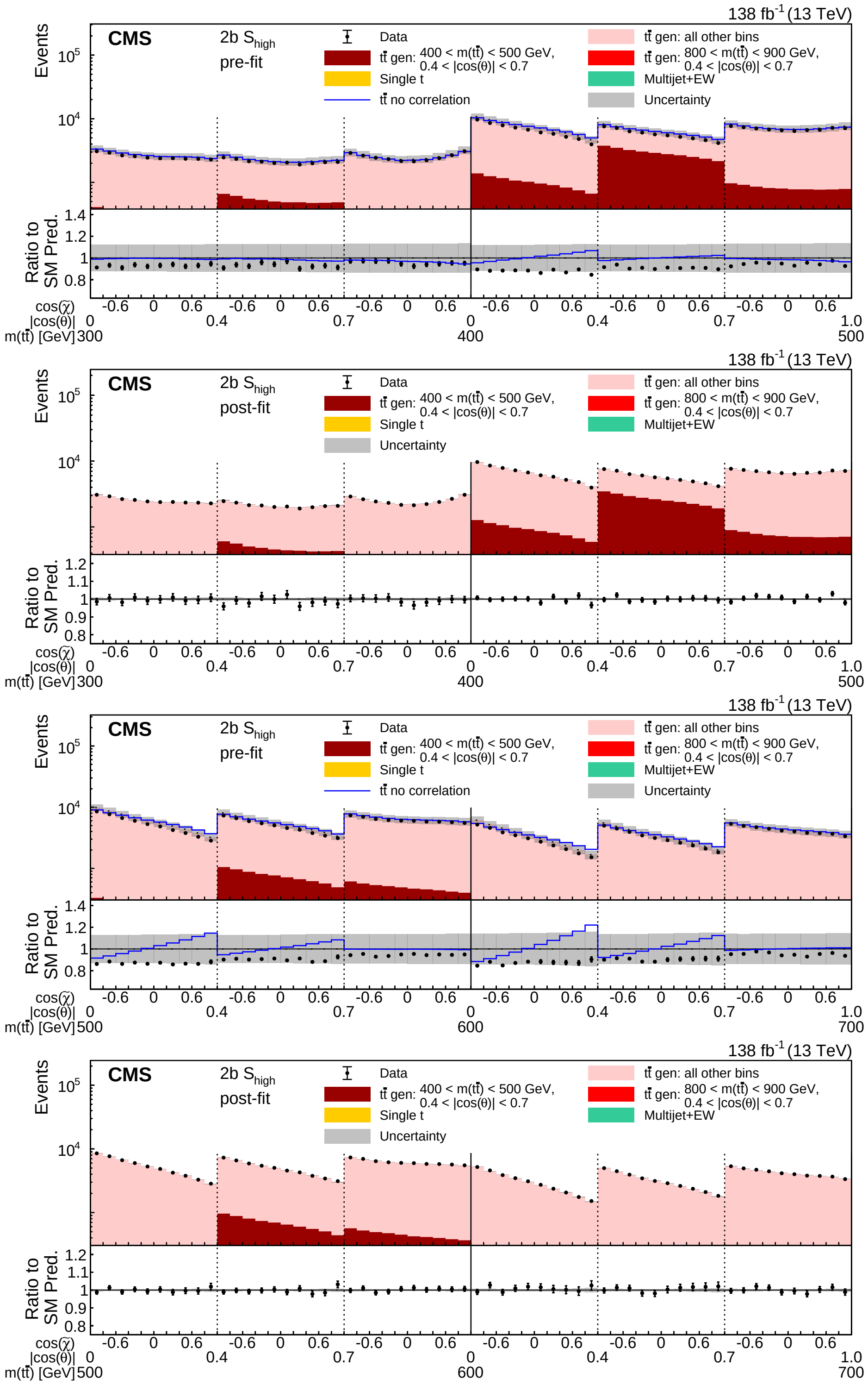

Figure 15: Pre- and post-fit distributions of $\cos(\tilde{\chi})$ comparing the data (points) to the POWHEG+PYTHIA simulation (stacked histograms) for the $\tilde{D}$ measurement in bins of $m(t\bar{t})$ *vs.* $|\cos(\theta)|$ in the 2b S_{high} category. The boundaries of the $|\cos(\theta)|$ and $m(t\bar{t})$ bins are labeled and indicated by dashed and solid lines, respectively. For the illustration of resolution effects, $t\bar{t}$ events generated in two selected $m(t\bar{t})$ *vs.* $|\cos(\theta)|$ bins are shown in different shades of red. All other $t\bar{t}$ contributions are shown in pink. A model without any polarization and spin correlation is shown as a blue line. The gray uncertainty band indicates the combined statistical and systematic uncertainties in the prediction. The vertical bars on the points show the statistical uncertainty. Ratios to the predicted yields are provided in the lower panels.

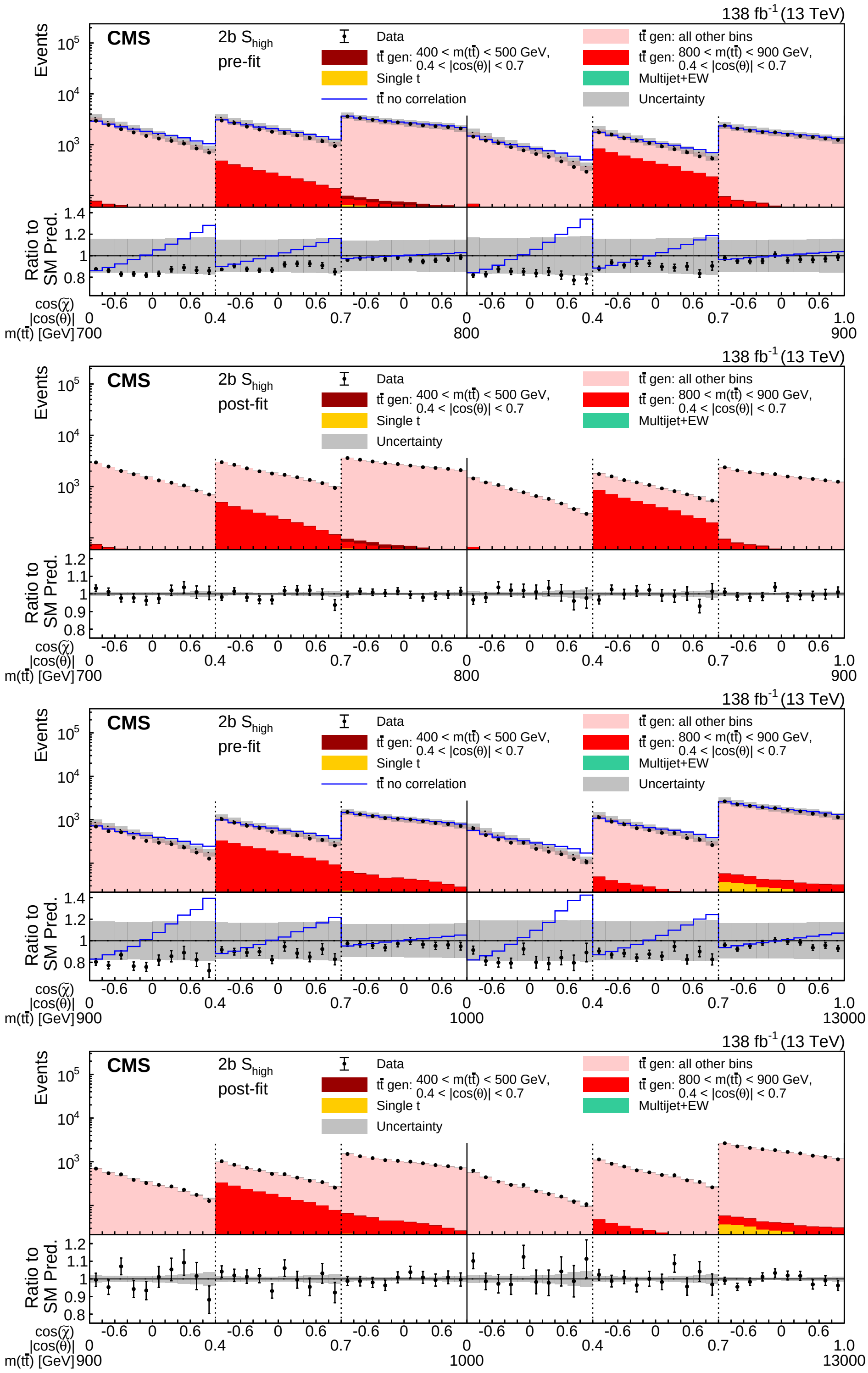

Figure 16: Pre- and post-fit distributions of $\cos(\tilde{\chi})$ comparing the data (points) to the POWHEG+PYTHIA simulation (stacked histograms) for the $\tilde{D}$ measurement in bins of $m(t\bar{t})$ *vs.* $|\cos(\theta)|$ in the 2b S_{high} category. The boundaries of the $|\cos(\theta)|$ and $m(t\bar{t})$ bins are labeled and indicated by dashed and solid lines, respectively. For the illustration of resolution effects, $t\bar{t}$ events generated in two selected $m(t\bar{t})$ *vs.* $|\cos(\theta)|$ bins are shown in different shades of red. All other $t\bar{t}$ contributions are shown in pink. A model without any polarization and spin correlation is shown as a blue line. The gray uncertainty band indicates the combined statistical and systematic uncertainties in the prediction. The vertical bars on the points show the statistical uncertainty. Ratios to the predicted yields are provided in the lower panels.

A possible bias in the measured Q_{mn} (D_n, $\tilde{D}_n$) was estimated by performing fits on simulations with variations of the coefficients of up to ± 0.3, which exceeds the maximum observed difference between the expected and measured values. We found that any bias turns out to be negligible compared to the other uncertainties in the measurements. We also performed the fit using the POWHEG+HERWIG and MADGRAPH5_aMC@NLO+PYTHIA simulations as pseudodata and found that we can extract the correct values of the coefficients.

9 Systematic uncertainties

Several theoretical and experimental systematic uncertainties affect the predicted event yields and are taken into account for the extraction of the Q_{mn} (D_n, $\tilde{D}_n$). Their templates are obtained from alternative or reweighted simulations corresponding to variations in a specific uncertainty source, usually by one standard deviation. We take into account the following theoretical uncertainties:

- The effect of higher-order contributions to the ME calculation is estimated by varying the renormalization μ_{r} and factorization μ_{f} scales up and down by a factor of two. Distributions for these variations are obtained using event weights in the POWHEG+PYTHIA simulation. The variations of μ_{r} and μ_{f} are parameterized in the fit by two independent nuisance parameters. The ME scales of $\mathrm{t\bar{t}}$ and single top quark production are treated separately.
- The difference in the $p_{\mathrm{T}}(\mathrm{t})$ spectrum between the POWHEG+PYTHIA NLO and the NNLO calculations, obtained with POWHEG MINNLO+PYTHIA exceeds what is expected based on the μ_{r} and μ_{f} variations. Therefore, an additional uncertainty is introduced, whose $+1$ standard deviation variation corresponds to the reweighting of the NLO to the NNLO simulation using a NN-based method [65, 66]. The NN-based approach is used to reduce the statistical fluctuations in this uncertainty.
- First order virtual electroweak corrections are calculated with HATHOR and applied to LO $\mathrm{t\bar{t}}$ events obtained with MADGRAPH5_aMC@NLO+PYTHIA. The ratio to the LO simulation without electroweak corrections is determined as a function of $m(\mathrm{t\bar{t}})$ and $|\cos(\theta)|$. These ratios are used as event weights to correct the POWHEG simulation. The differences between the electroweak corrected and the default POWHEG simulation are taken into account as uncertainty.
- The 100 Hessian variations of the NNPDF3.1 set plus the variation of strong coupling α_S are taken into account as PDF uncertainties. For each of these variations a nuisance parameter is added. The distributions are obtained using the corresponding event weights. The PDF variations are correlated for $\mathrm{t\bar{t}}$ and single top quark production.
- The uncertainties in the initial- and final-state parton showers are estimated by varying the scales for the different splittings $\mathrm{g} \to \mathrm{q\bar{q}}$, $\mathrm{g} \to \mathrm{gg}$, $\mathrm{q} \to \mathrm{qg}$, and $\mathrm{b} \to \mathrm{bg}$ by a factor of two, resulting in a total of eight independent variations. The corresponding distributions are obtained using event weights. The parton shower scale variations are correlated for $\mathrm{t\bar{t}}$ and single top quark production.
- The scale that separates the phase space of the first QCD emission into soft and hard parts is controlled by the h_{damp} parameter for POWHEG simulations. The values used for the CP5 tune are $1.38^{+0.92}_{-0.51}\, m_{\mathrm{t}}$. Separate samples produced with the different values of h_{damp} are used to obtain the corresponding distributions. To reduce the impact from statistical fluctuations we employ the NN based approach [65] to determine the

weights applied to the central simulation based on the kinematic properties of top quarks determined at the generator level.

- To estimate the effect of the uncertainty in m_{t}, a variation of 0.5 GeV [46] is taken into account. For the evaluation of the expected event yields, we use the m_{t}-dependent $\mathrm{t\bar{t}}$ production cross sections of 843 (820) pb for $m_{\mathrm{t}} = 172.0$ (173.0) GeV [67].
- The uncertainties in the underlying event modeling are estimated using separate samples that represent an envelope of the uncertainties in the PYTHIA CP5 tune [38].
- The fraction of leptonically decaying b hadrons is changed according to the known uncertainty in the branching fraction using event-based reweighting [1].
- The uncertainty in the color reconnection is assessed using an alternative model where the reconnection of colored particles from resonant decays is activated in PYTHIA, while this is deactivated in the default tune. Other variations use the gluon move and the QCD-inspired models [68, 69]. The differences between these three and the default samples are added as symmetric uncertainties.
- At the $\mathrm{t\bar{t}}$ production threshold, theoretical calculations based on nonrelativistic QCD [70] predict $\mathrm{t\bar{t}}$ bound states and other effects not included in the POWHEG+PYTHIA simulation. To estimate their effects on the measurement, we mimic the theoretical calculation by adding a pseudoscalar particle η_{t} with a mass of 343 GeV and a width of twice the top quark width. It is produced in gg fusion and decays as $\eta_{\mathrm{t}} \to \mathrm{WbW\bar{b}}$. This is calculated using MADGRAPH5_aMC@NLO+PYTHIA and normalized using the cross section of 6.43 pb from Ref. [71]. The difference observed using this model is used to estimate the uncertainty due to bound-state effects.

All theoretical uncertainties affect all data-taking periods in the same way and the corresponding nuisance parameters are fully correlated between them.

We take into account the following experimental uncertainties:

- The integrated luminosities for the 2016, 2017, and 2018 data-taking years have 1.2–2.5% individual uncertainties [72–74], while the overall uncertainty for the 2016–2018 period is 1.6%.
- The prediction of the number of pileup interactions in simulation is assuming a total inelastic proton-proton cross section of 69.2 mb [75]. Changes in the simulated pileup multiplicity are estimated by varying the total inelastic cross section by $\pm 4.6\%$. Templates with enhanced and reduced pileup are obtained by applying event weights. This uncertainty is treated as fully correlated between the data-taking periods.
- The jet energy scale uncertainties are split into 19 different sources [59]. The combined uncertainties are p_{T}- and η-dependent, with a magnitude that varies between 0.3 and 1.8% for the relevant jets. In addition, variations are applied depending on the true generated type to b jets, c jets, uds jets, and gluon jets. The correlations among the years are evaluated for each source. The differences in the distributions are obtained by rescaling the jet momenta in the simulation.
- Separate uncertainties for the jet energy resolution are taken into account for jets in the endcap and barrel regions by varying the resolution corrections within their uncertainties. These uncertainties are uncorrelated among the years.
- The dominant uncertainty in the $p_{\mathrm{T}}^{\mathrm{miss}}$ is due to the jet energy calibration. Therefore,

the $p_{\mathrm{T}}^{\mathrm{miss}}$ is also recalculated whenever the jet momenta are rescaled. An additional contribution to the uncertainty due to particles that do not belong to the selected jets is estimated [62]. This uncertainty is uncorrelated among years.

- Uncertainties in the electron and muon reconstruction and trigger efficiencies are determined [56]. For each flavor a statistical and systematic uncertainty in the derived scale factors are taken into account, where the statistical component is uncorrelated and the systematic component is correlated among the years. In addition, an overall normalization uncertainty of 0.5% is used to account for the differences in DY and $\mathrm{t\bar{t}}$ events.
- Since the analysis uses three b tagging categories as input to the NN, we allow for separate variations of the uncertainties in the scale factors for the tight, medium, and loose b tagging selections [60, 76]. The variations are performed by recalculating an event probability using all jets and their true type. The uncertainties in the correction factors for b and c jets are split into several sources such as statistical, jet energy correction, and pileup uncertainties. The statistical uncertainty is uncorrelated among the years, while the rest is treated as correlated. The uncertainties in the correction factors for the light jet flavors are split into a correlated and an uncorrelated component.
- During the data-taking, a gradual shift in the timing of the inputs of the ECAL L1 trigger in the region $|\eta| > 2.0$ and of the muon trigger caused a specific trigger inefficiency. Correction factors as functions of p_{T}, η, and time are computed from data and applied to the simulation. The statistical uncertainties in these correction factors are taken into account.
- The uncertainties in the background estimations are detailed in Section 7.

For each bin, an additional nuisance parameter is added [77] whose variation corresponds to the statistical uncertainty in the central templates. It is known that statistical fluctuations are also important for the systematic variations. In particular, if the variations are evaluated based on statistically independent simulations, the statistical effects can easily reach or even exceed the magnitude of the systematic effect. Therefore, it is often helpful to require a certain smoothness of the relative systematic effects. This reduces unphysical constraints of the related nuisance parameters. A 6(3)-dimensional smoothing [78] is applied for the full matrix (D and $\tilde{D}$) measurements.

10 Results

From the fits to the data we obtain the values of Q_{mn} (D_n, $\tilde{D}_n$) in bins of $m(\mathrm{t\bar{t}})$ *vs.* $|\cos(\theta)|$ or $p_{\mathrm{T}}(\mathrm{t})$ *vs.* $|\cos(\theta)|$. In the following, we concentrate on regions of the phase space that are of special interest, e.g., where a higher level of entanglement is expected. Most of the presented results are obtained from the combination of several $m(\mathrm{t\bar{t}})$ *vs.* $|\cos(\theta)|$ or $p_{\mathrm{T}}(\mathrm{t})$ *vs.* $|\cos(\theta)|$ bins.

With the $\mathrm{t\bar{t}}$ event yields of the post-fit model at the generator level Y_n, and the normalization factors a_n, we obtain the total fitted event yields $K_n = Y_n a_n$. The result in a combined bin g is then obtained by averaging the measurements from bins $\{n\}$ using

$$\hat{Q}_{mg} = \frac{1}{\sum\limits_{n\in g} K_n} \sum_{n\in g} K_n Q_{mn}. \tag{14}$$

The uncertainties in $\hat{Q}_{mg}$ are calculated using error propagation taking into account the uncertainties and their correlations in the event yields and the Q_{mn} as obtained from the fit. The combined normalization factors are obtained based on the K_n sum

$$c_g = \frac{1}{\sum\limits_{n \in g} Y'_n} \sum_{n \in g} K_n, \tag{15}$$

where Y'_n are the $t\bar{t}$ yields of the pre-fit model at the generator level.

Following Refs. [9, 23], we use the new observables $C^{\pm}_{nr} = C_{nr} \pm C_{rn}$, $C^{\pm}_{rk} = C_{rk} \pm C_{kr}$, and $C^{\pm}_{nk} = C_{nk} \pm C_{kn}$, where for the calculation the covariances are taken into account. These are either even or odd under parity (P) and charge-parity (CP) transformations.

The inclusive full matrix measurements based on the $m(t\bar{t})$ *vs.* $|\cos(\theta)|$ and $p_T(t)$ *vs.* $|\cos(\theta)|$ fits are obtained from the combination of all bins in the additional observables, and are shown in Fig. 17. The displayed values of Δ_E are calculated following Eq. (5).

As expected, both binnings lead to consistent results, where the $p_T(t)$ *vs.* $|\cos(\theta)|$ binning has a higher expected and observed precision. For the inclusive coefficients, the values predicted by POWHEG+PYTHIA, POWHEG+HERWIG, MADGRAPH5_aMC@NLO+PYTHIA, and MINNLO+PYTHIA are similar. The measured coefficients are in agreement with the predictions and consistent with the previous measurement in the $t\bar{t}$ dilepton channel [9]. The measured polarizations are all compatible with zero. Only the diagonal elements of C differ from zero with the exception of C^{+}_{rk}, which is the only even coefficient under P and CP transformation. In Fig. 18 the results of the inclusive D and $\tilde{D}$ measurements obtained with the $m(t\bar{t})$ *vs.* $|\cos(\theta)|$ and $p_T(t)$ *vs.* $|\cos(\theta)|$ binnings are shown.

Entangled quantum states are expected at the threshold of $t\bar{t}$ production and also at high $m(t\bar{t})$ and $p_T(t)$ in events with low $|\cos(\theta)|$ [21]. Therefore, taking advantage of the binning in the additional observables, we can obtain the spin correlation coefficients and thus test the entanglement criterion in several $m(t\bar{t})$ and $p_T(t)$ regions and its dependence on $|\cos(\theta)|$. Figures 19–22 provide the results of the full matrix measurements including the Δ_E values in bins of $m(t\bar{t})$ and $p_T(t)$, i.e., we combine the $|\cos(\theta)|$ bins in each of these regions. While POWHEG+HERWIG predicts a slightly smaller spin correlation than the other simulations, the measured coefficients are compatible with all predictions. With these measurements, the differences in the spin correlation for various kinematic regions become clearly visible. In particular, for the measurement in $p_T(t)$, we observe the signs of C_{rr} and C_{kk} changing from positive to negative with increasing $p_T(t)$, indicating the transition from the spin-singlet to the spin-triplet as the dominant state.

At the $t\bar{t}$ production threshold, the most significant results for entanglement using the full matrix measurement, based on the criterion $\Delta_E > 1$, are obtained for $m(t\bar{t}) < 400\,\text{GeV}$ and for $p_T(t) < 100\,\text{GeV}$. We evaluate the significance of the deviation from the separable state hypothesis with $\Delta_E = 1$ based on the uncertainties in the measured values of Δ_E. However, the observed significance for entanglement does not exceed 2 standard deviations.

The D and $\tilde{D}$ measurements are presented in bins of $m(t\bar{t})$ and $p_T(t)$ in Fig. 23. The finer $p_T(t)$ binning in the D measurement allows studying events with $p_T(t) < 50\,\text{GeV}$, where a significance for entanglement of 3.5 (4.4) standard deviations is observed (expected). A similar analysis performed in the dilepton channel [15] has higher sensitivity for entanglement at the $t\bar{t}$ production threshold. Overall POWHEG+HERWIG predicts slightly higher values of D in the threshold region, but the measured coefficients remain compatible with all predictions.

Figure 24 shows the contributions of various uncertainty sources to the uncertainties in the measured Δ_E, D, and $\tilde{D}$ in bins of $m(t\bar{t})$. In general, the uncertainties in the results are dominated by the statistical contribution, with the exception of the D measurement, where system-

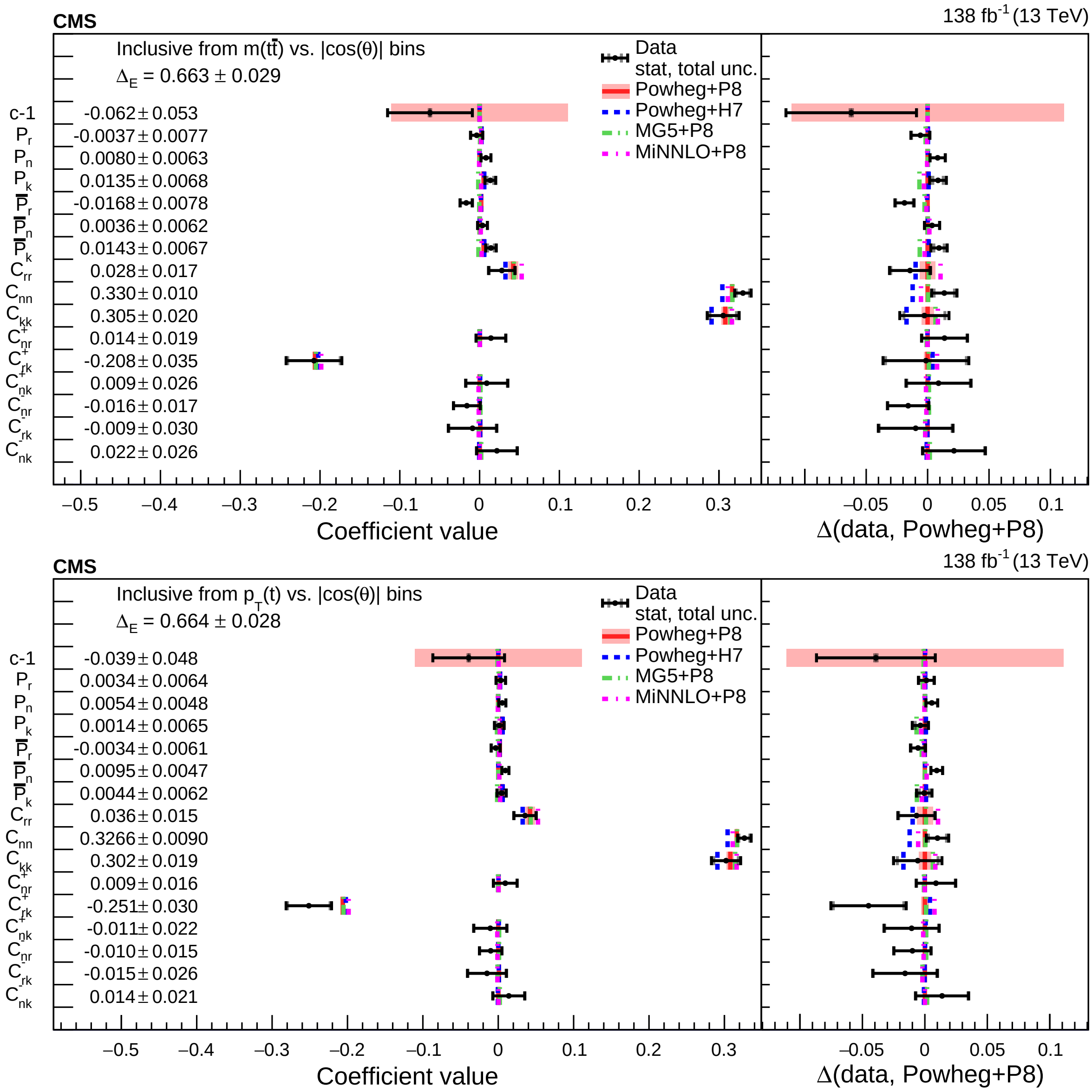

Figure 17: Results of the inclusive full matrix measurement obtained by combining the bins of the $m(\mathrm{t\bar{t}})$ *vs.* $|\cos(\theta)|$ (upper) and $p_{\mathrm{T}}(\mathrm{t})$ *vs.* $|\cos(\theta)|$ (lower) measurements. The measurements (markers) are shown with the statistical uncertainty (inner error bars) and total uncertainty (outer error bars) and compared to the predictions of POWHEG+PYTHIA, POWHEG+HERWIG, MADGRAPH5_aMC@NLO+PYTHIA and MINNLO+PYTHIA. In the right panels, results are presented with the POWHEG+PYTHIA predictions subtracted. The POWHEG+PYTHIA prediction is displayed with ME scale and PDF uncertainties. The values of Δ_{E} are displayed for each measurement.

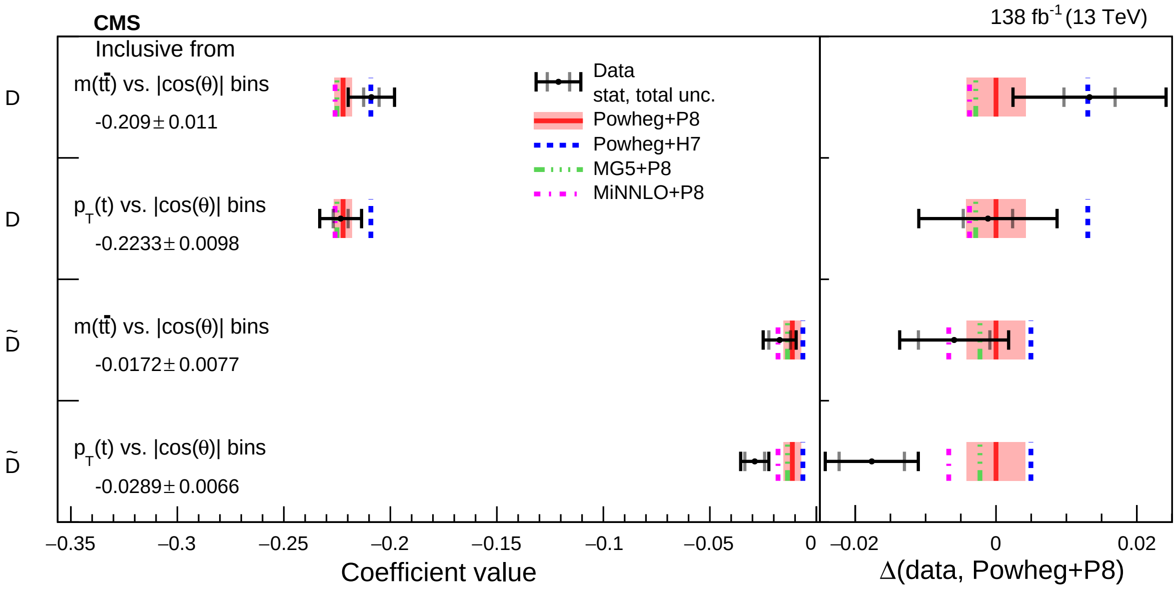

Figure 18: Results of the inclusive D and $\tilde{D}$ measurement obtained by combining the bins of the $m(\mathrm{t\bar{t}})$ *vs.* $|\cos(\theta)|$ and $p_{\mathrm{T}}(\mathrm{t})$ *vs.* $|\cos(\theta)|$ measurements. The measurements (markers) are shown with the statistical uncertainty (inner error bars) and total uncertainty (outer error bars) and compared to the predictions of POWHEG+PYTHIA, POWHEG+HERWIG, MADGRAPH5_aMC@NLO+PYTHIA and MINNLO+PYTHIA. In the right panel, results are presented with the POWHEG+PYTHIA predictions subtracted. The POWHEG+PYTHIA prediction is displayed with ME scale and PDF uncertainties.

atic effects are more important at low $m(\mathrm{t\bar{t}})$. The uncertainty in the b tagging calibration is the dominant source, but depending on the bin, theoretical uncertainties can be of similar sizes, in particular ME and PS scales.

We further study the results in the region $|\cos(\theta)| < 0.4$. These are shown in bins of $m(\mathrm{t\bar{t}})$ in Figs. 25–26 for the full matrix and in Fig. 27 for the $\tilde{D}$ measurement. The most significant observation (expectation) of entanglement is obtained for $m(\mathrm{t\bar{t}}) > 800$ GeV and $|\cos(\theta)| < 0.4$, with 6.7 (5.6) standard deviations for the full matrix measurement and 6.1 (5.5) standard deviations for the $\tilde{D}$ measurement. The D measurement does not have any sensitivity for entanglement in this region, since the diagonal elements of the C matrix do not all have the same sign.

Figure 28 summarizes the observed (expected) significance of the measured entanglement variables. In the upper panels of Fig. 28, the measured results for D (left) near the $\mathrm{t\bar{t}}$ production threshold and for $\tilde{D}$ (right) at high $m(\mathrm{t\bar{t}})$ and low $|\cos(\theta)|$ are shown. For the full matrix measurement (lower), the Δ_{E} results with the highest expected significance are shown for the threshold and high-$m(\mathrm{t\bar{t}})$ kinematic regions.

Previous measurements of the $\mathrm{t\bar{t}}$ entanglement by ATLAS [14] and CMS [15] were performed only at the threshold of $\mathrm{t\bar{t}}$ production, where the relative velocity of the top quarks is low. In this analysis, we additionally measure the entanglement at high $m(\mathrm{t\bar{t}})$, where, in most of the selected events, the top quark and antiquark decays are space-like separated because of their high relative velocity. Using the decay products, the spin correlation is measured when the top quarks decay. From simulations we know that for $m(\mathrm{t\bar{t}}) > 800$ GeV the fraction of space-like separated decays is about 90% [79]. An observation of entanglement could be explained by an unobserved exchange of classical information between the decaying top quarks. Therefore, we introduce a more stringent criterion for entanglement that cannot be explained by such an

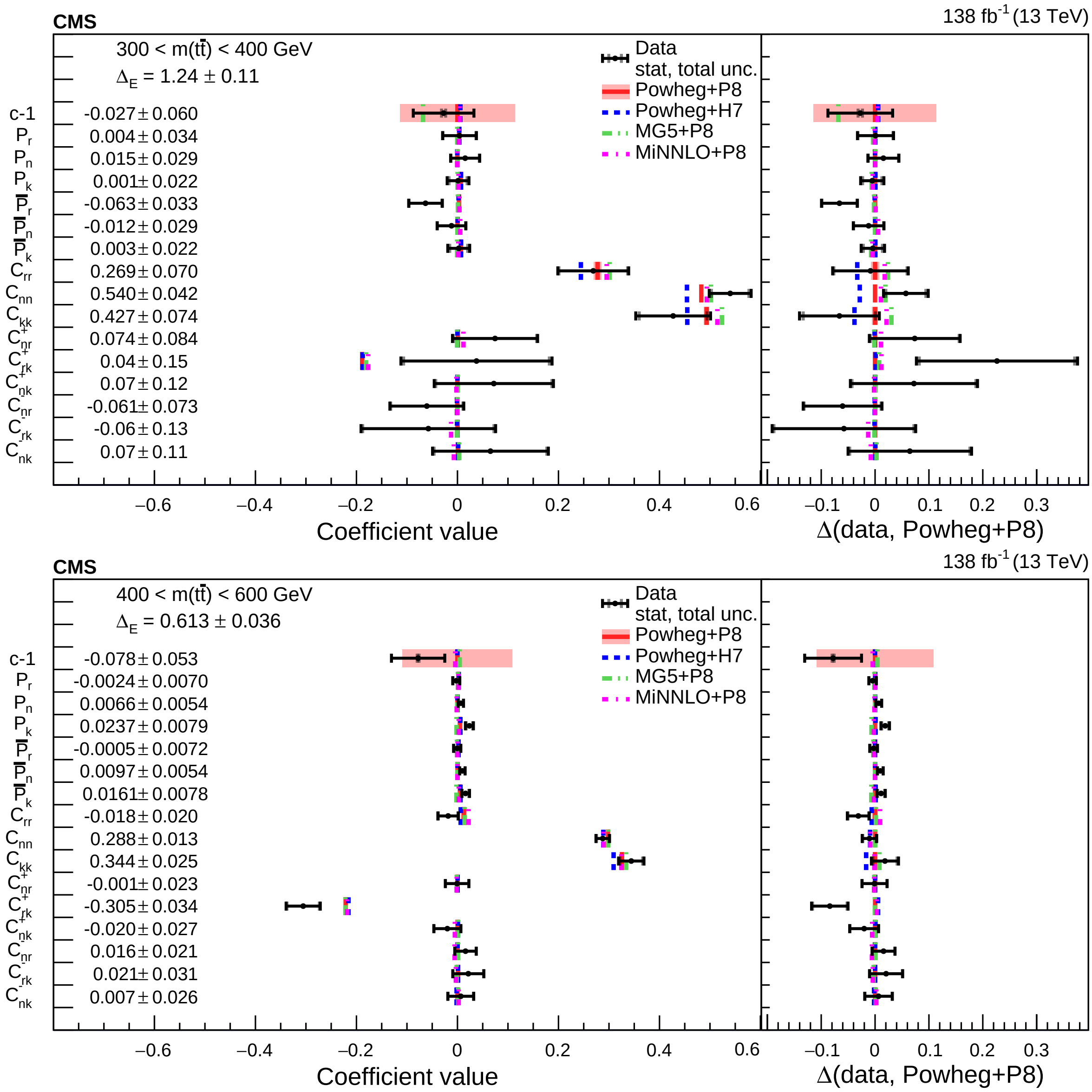

Figure 19: Results of the full matrix measurement in bins of $m(\mathrm{t\bar{t}})$. The measurements (markers) are shown with the statistical uncertainty (inner error bars) and total uncertainty (outer error bars) and compared to the predictions of POWHEG+PYTHIA, POWHEG+HERWIG, MADGRAPH5_aMC@NLO+PYTHIA and MINNLO+PYTHIA. In the right panels, results are presented with the POWHEG+PYTHIA predictions subtracted. The POWHEG+PYTHIA prediction is displayed with ME scale and PDF uncertainties. The values of Δ_{E} are displayed for each measurement.

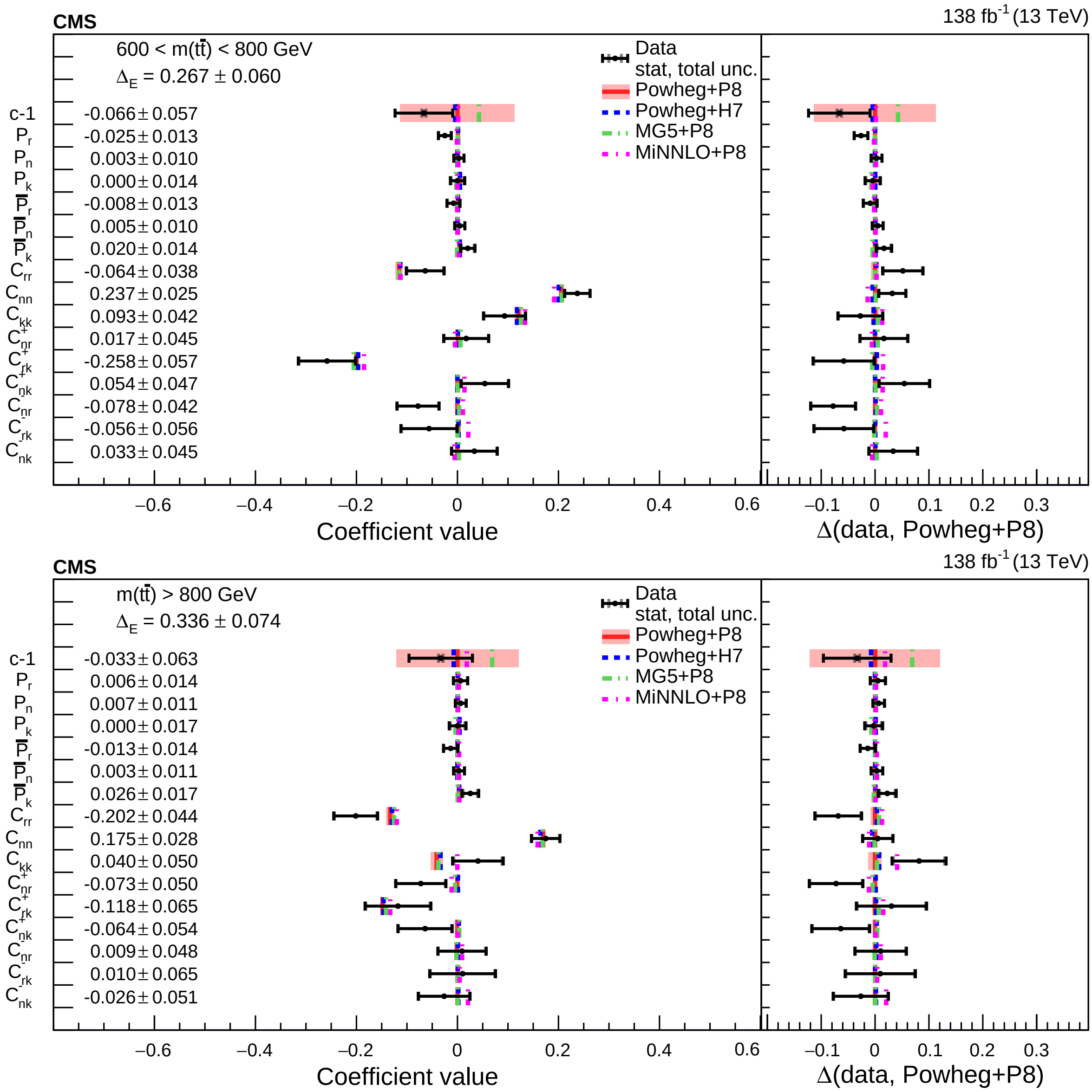

Figure 20: Results of the full matrix measurement in bins of $m(\mathrm{t\bar{t}})$. The measurements (markers) are shown with the statistical uncertainty (inner error bars) and total uncertainty (outer error bars) and compared to the predictions of POWHEG+PYTHIA, POWHEG+HERWIG, MADGRAPH5_aMC@NLO+PYTHIA and MINNLO+PYTHIA. In the right panels, results are presented with the POWHEG+PYTHIA predictions subtracted. The POWHEG+PYTHIA prediction is displayed with ME scale and PDF uncertainties. The values of Δ_E are displayed for each measurement.

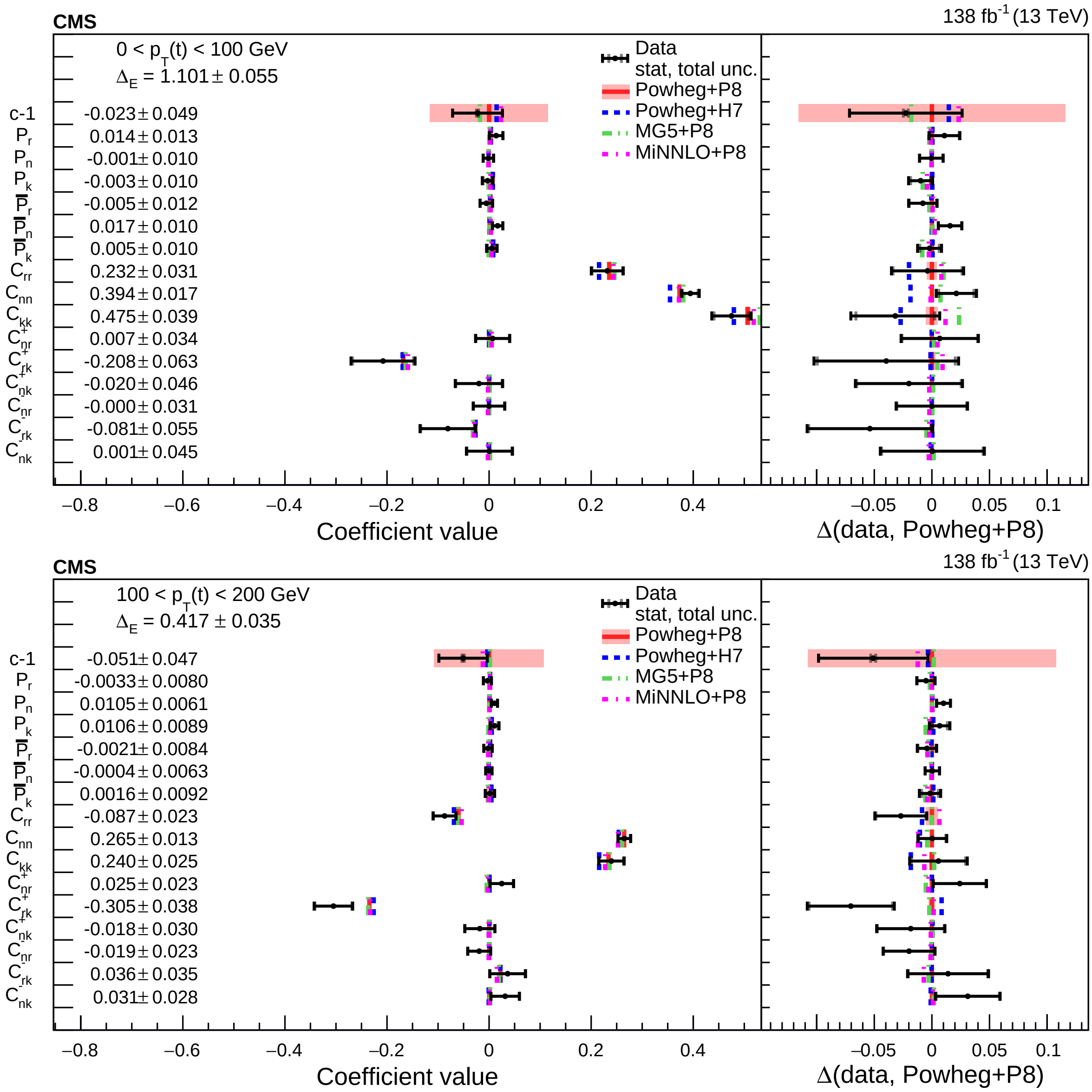

Figure 21: Results of the full matrix measurement in bins of $p_T(t)$. The measurements (markers) are shown with the statistical uncertainty (inner error bars) and total uncertainty (outer error bars) and compared to the predictions of POWHEG+PYTHIA, POWHEG+HERWIG, MADGRAPH5_aMC@NLO+PYTHIA and MINNLO+PYTHIA. In the right panels, results are presented with the POWHEG+PYTHIA predictions subtracted. The POWHEG+PYTHIA prediction is displayed with ME scale and PDF uncertainties. The values of Δ_E are displayed for each measurement.

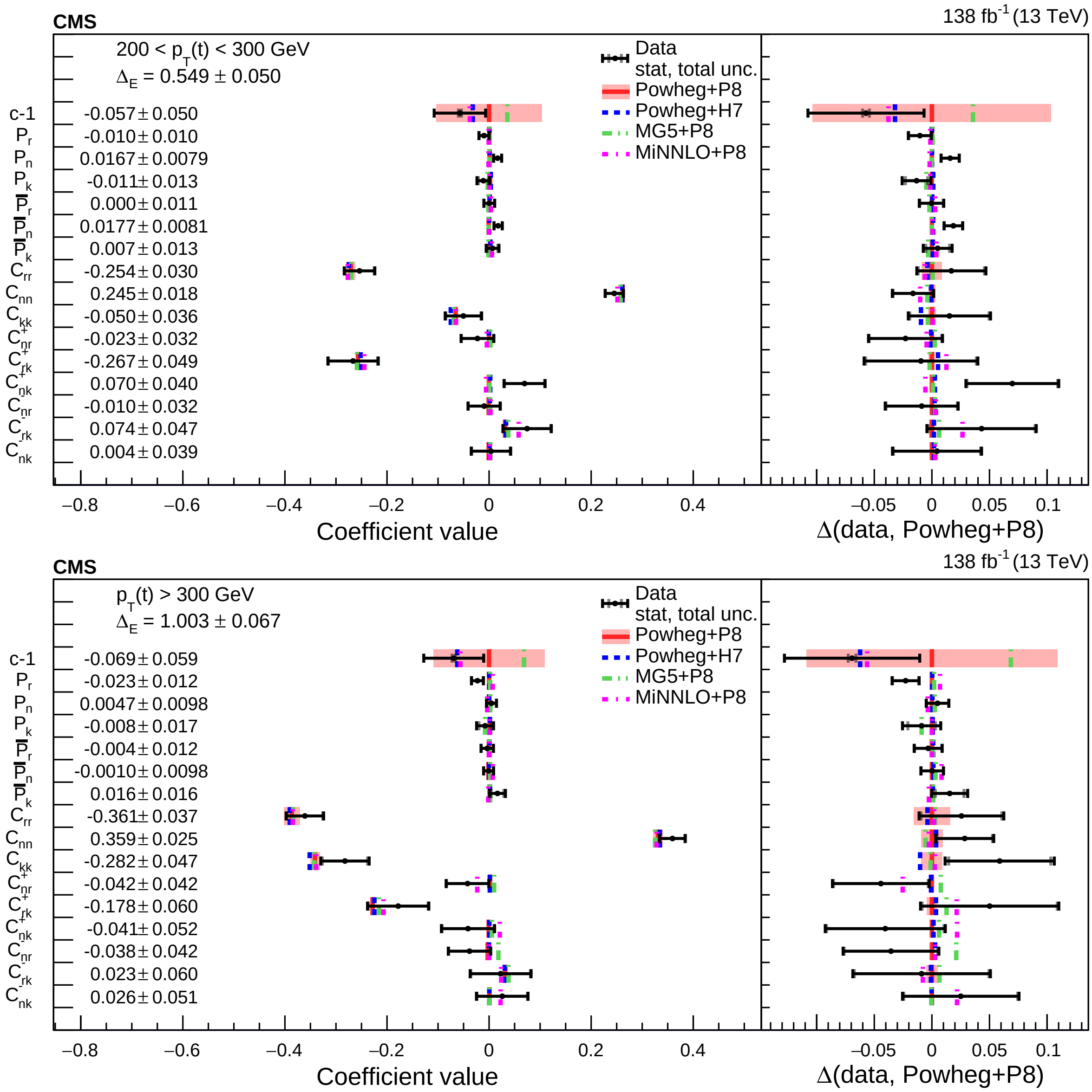

Figure 22: Results of the full matrix measurement in bins of $p_T(t)$. The measurements (markers) are shown with the statistical uncertainty (inner error bars) and total uncertainty (outer error bars) and compared to the predictions of POWHEG+PYTHIA, POWHEG+HERWIG, MADGRAPH5_aMC@NLO+PYTHIA and MINNLO+PYTHIA. In the right panels, results are presented with the POWHEG+PYTHIA predictions subtracted. The POWHEG+PYTHIA prediction is displayed with ME scale and PDF uncertainties. The values of Δ_E are displayed for each measurement.

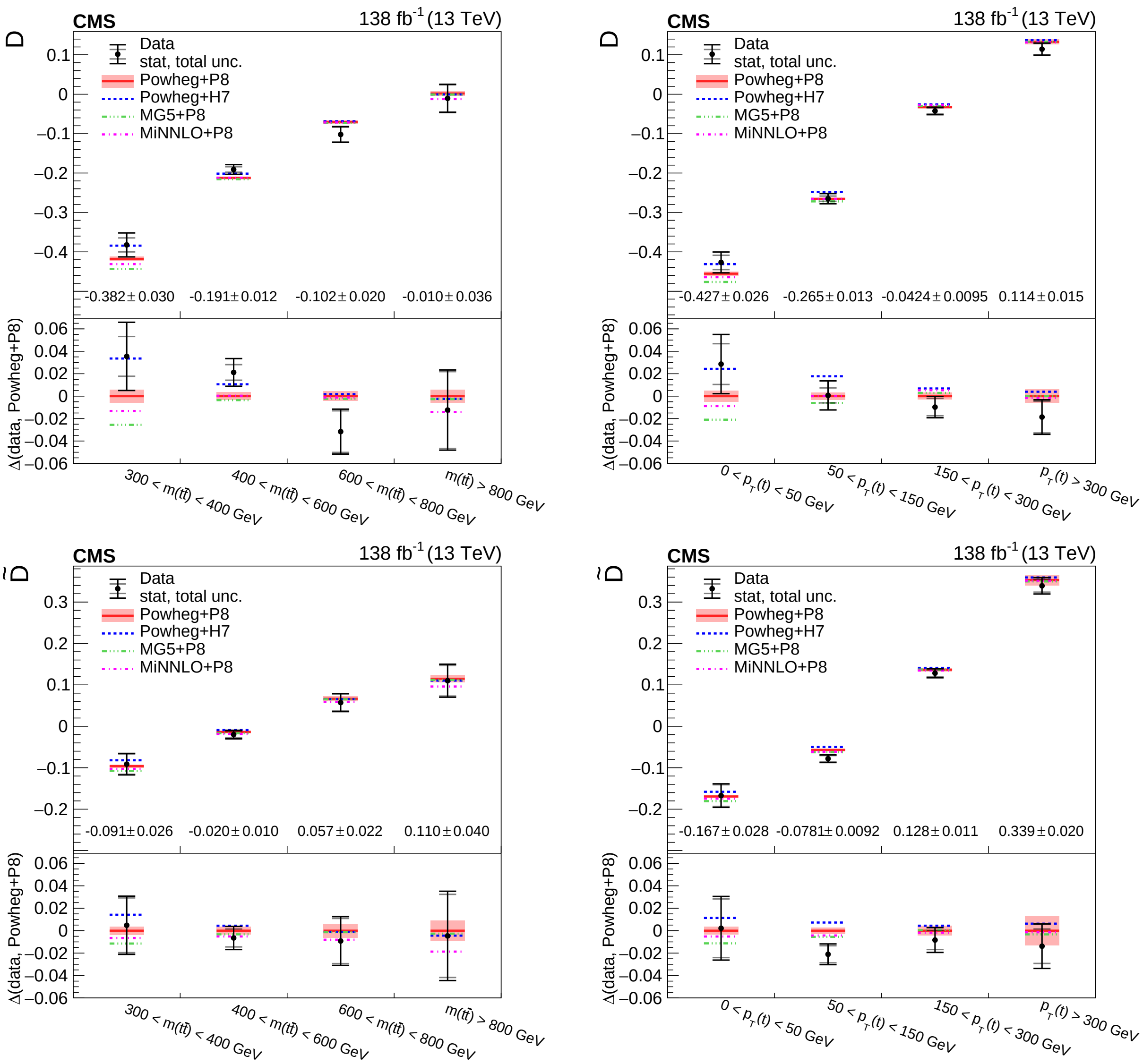

Figure 23: Results of the D and $\tilde{D}$ measurements in bins of $m(\mathrm{t\bar{t}})$ and $p_{\mathrm{T}}(\mathrm{t})$. The measurements (markers) are shown with the statistical uncertainty (inner error bars) and total uncertainty (outer error bars) and compared to the predictions of POWHEG+PYTHIA, POWHEG+HERWIG, MADGRAPH5_aMC@NLO+PYTHIA and MINNLO+PYTHIA. In the lower panel results are presented with the POWHEG+PYTHIA predictions subtracted. The POWHEG+PYTHIA prediction is displayed with ME scale and PDF uncertainties.

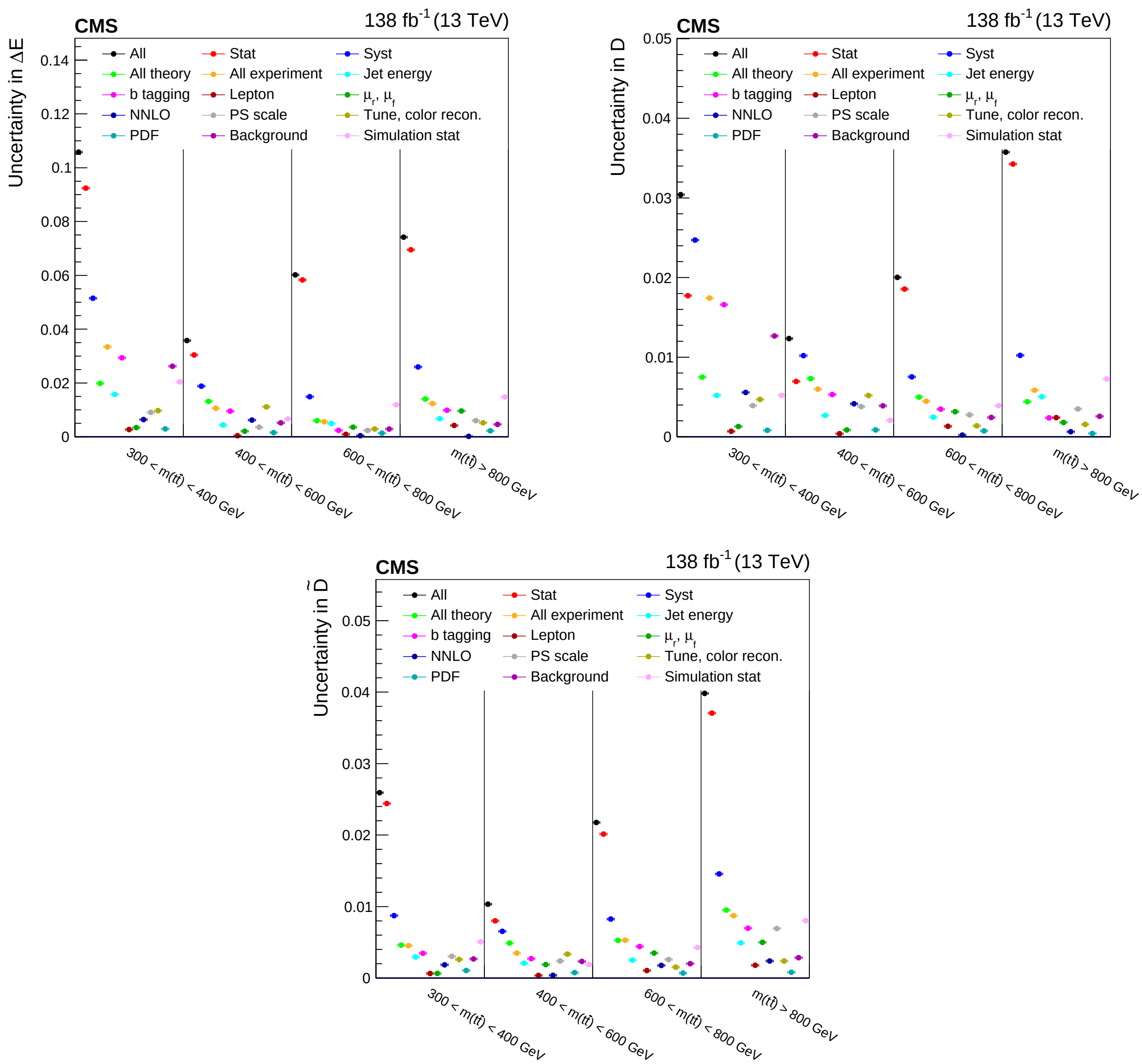

Figure 24: Contribution of individual uncertainty sources or groups of uncertainties in the measured Δ_{E}, D, and $\tilde{D}$ in bins of $m(\mathrm{t\bar{t}})$.

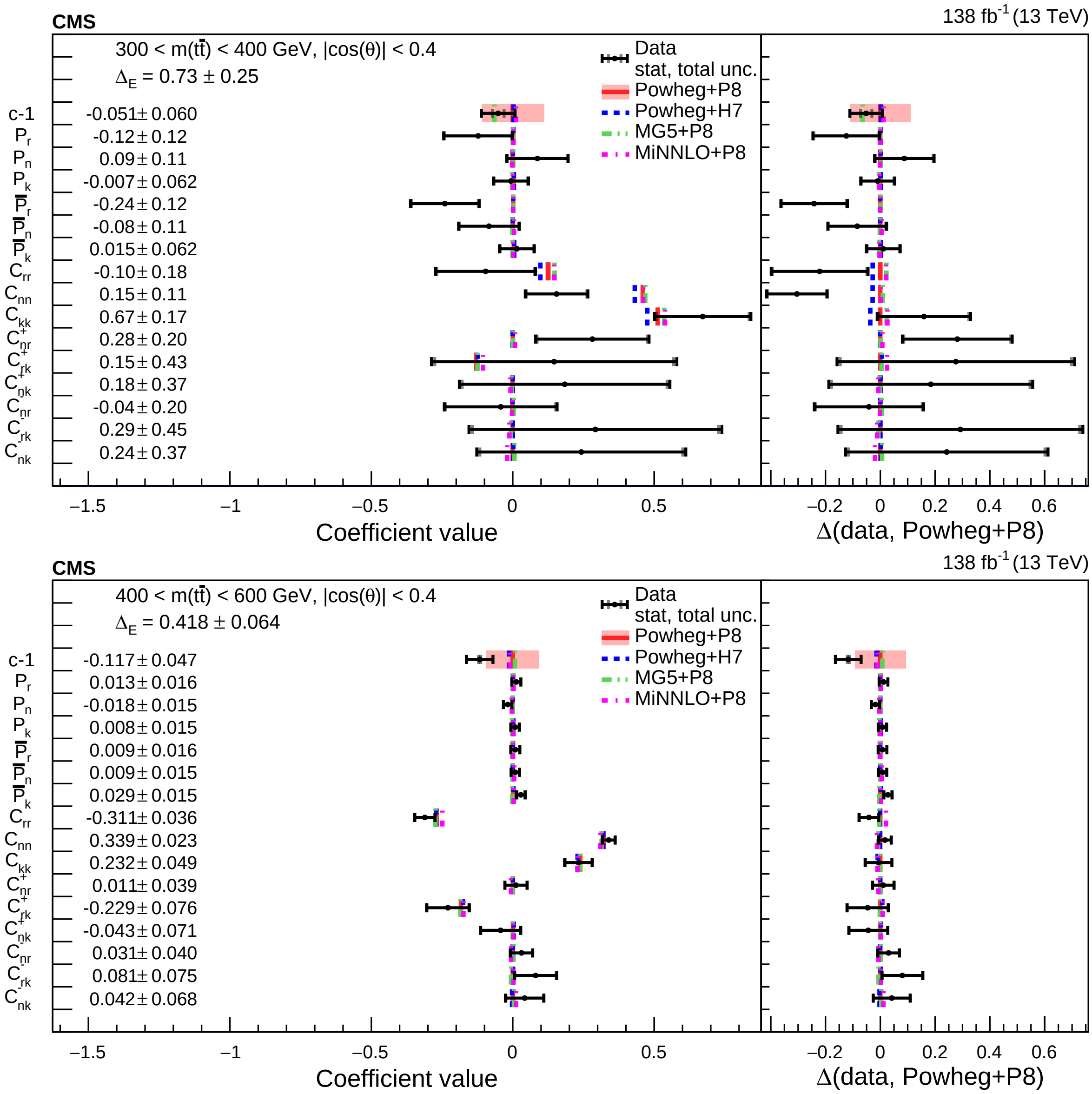

Figure 25: Results of the full matrix measurement in bins of $m(t\bar{t})$ for $|\cos(\theta)| < 0.4$. The measurements (markers) are shown with the statistical uncertainty (inner error bars) and total uncertainty (outer error bars) and compared to the predictions of POWHEG+PYTHIA, POWHEG+HERWIG, MADGRAPH5_aMC@NLO+PYTHIA and MINNLO+PYTHIA. In the right panels, results are presented with the POWHEG+PYTHIA predictions subtracted. The POWHEG+PYTHIA prediction is displayed with ME scale and PDF uncertainties. The values of Δ_E are displayed for each measurement.

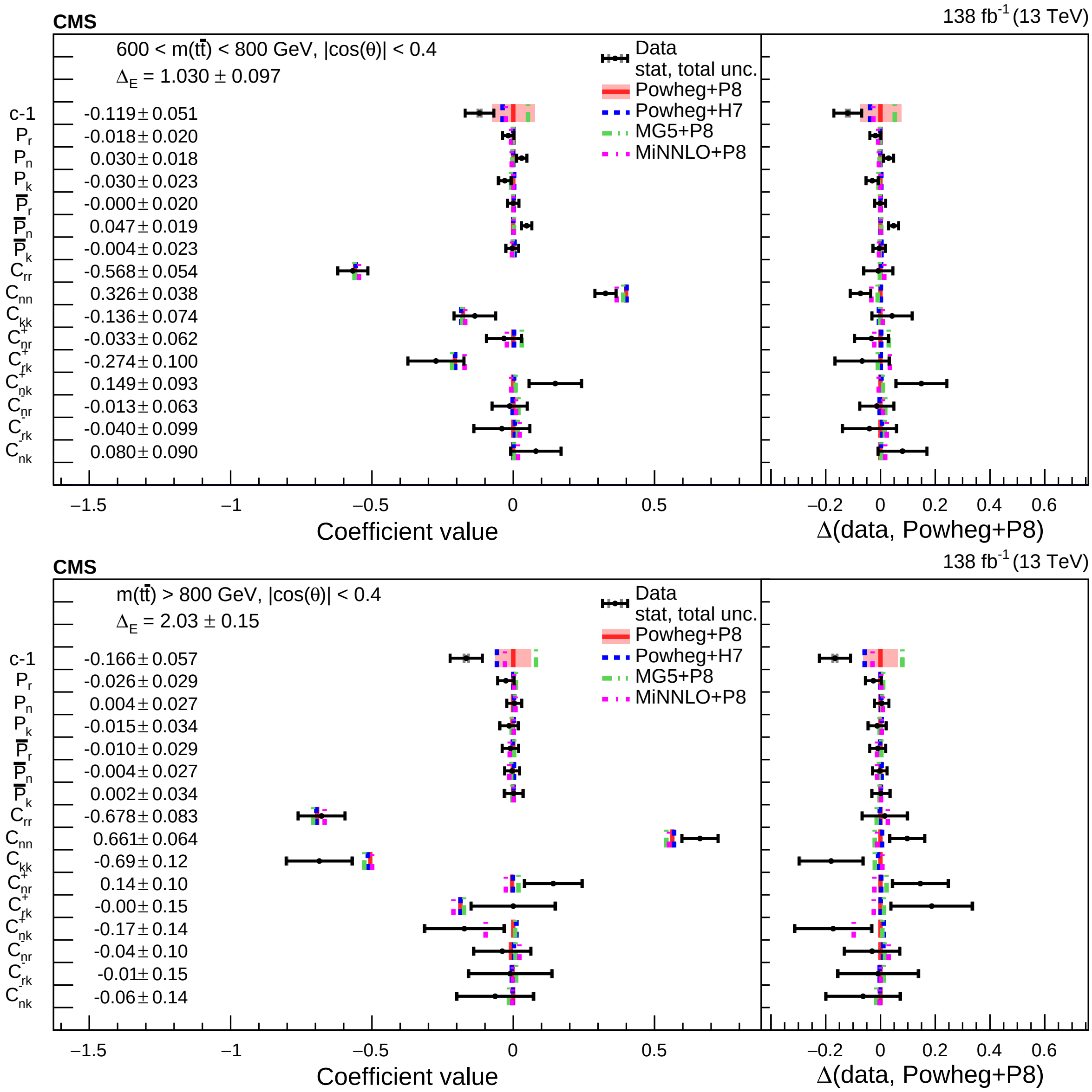

Figure 26: Results of the full matrix measurement in bins of $m(\mathrm{t\bar{t}})$ for $|\cos(\theta)| < 0.4$. The measurements (markers) are shown with the statistical uncertainty (inner error bars) and total uncertainty (outer error bars) and compared to the predictions of POWHEG+PYTHIA, POWHEG+HERWIG, MADGRAPH5_aMC@NLO+PYTHIA and MINNLO+PYTHIA. In the right panels, results are presented with the POWHEG+PYTHIA predictions subtracted. The POWHEG+PYTHIA prediction is displayed with ME scale and PDF uncertainties. The values of Δ_{E} are displayed for each measurement.

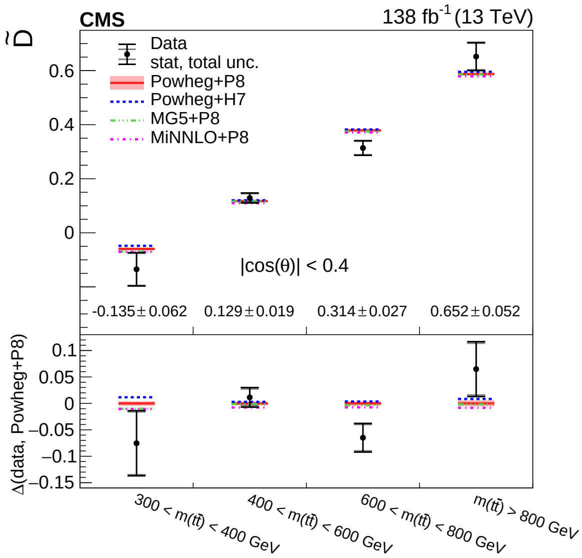

Figure 27: Results of the $\tilde{D}$ measurements in bins of $m(\mathrm{t\bar{t}})$ for $|\cos(\theta)| < 0.4$. The measurements (markers) are shown with the statistical uncertainty (inner error bars) and total uncertainty (outer error bars) and compared to the predictions of POWHEG+PYTHIA, POWHEG+HERWIG, MADGRAPH5_aMC@NLO+PYTHIA and MINNLO+PYTHIA. In the lower panel results are presented with the POWHEG+PYTHIA predictions subtracted. The POWHEG+PYTHIA prediction is displayed with ME scale and PDF uncertainties.

exchange of information at $v \leq c$ alone ("critical entanglement"). For this, the time-like separated decays are assumed to contribute with the maximum possible value for entanglement of $\Delta_{\mathrm{E\,max}} = 3$, while the space-like separated decays should at least fulfill the condition $\Delta_{\mathrm{E\,sep}} = 1$. Therefore, the lower boundary of critical entanglement $\Delta_{\mathrm{E\,crit}}$ can be defined for a given fraction f of space-like separated decays as follows:

$$\Delta_{\mathrm{E\,crit}} = f\Delta_{\mathrm{E\,sep}} + (1-f)\Delta_{\mathrm{E\,max}}. \quad (16)$$

As was shown in Ref. [80], using top quark decays in the definition of f results in the most stringent criterion $\Delta_{\mathrm{E\,crit}}$. The most sensitive measurements in the threshold and high-$m(\mathrm{t\bar{t}})$ kinematic regions are summarized in Fig. 29 together with the value for $\Delta_{\mathrm{E\,crit}}$ for each case, and the significance with respect to critical entanglement and separable states. The first bin $p_{\mathrm{T}}(\mathrm{t}) < 50\,\mathrm{GeV}$ was obtained using the D measurement, and the second bin for $m(\mathrm{t\bar{t}}) > 800\,\mathrm{GeV}$ and $|\cos(\theta)| < 0.4$ was obtained using the full matrix measurement. In the second bin, the space-like fraction is $f = 90\%$, which corresponds to a $\Delta_{\mathrm{E\,crit}} = 1.2$. The measured (expected) value exceeds this limit by 5.4 (4.1) standard deviations as shown by the blue vertical arrow.

To validate the Gaussian approximation used in calculating these significances, we perform profile likelihood fits for fixed values of Δ_{E} in the bin with $m(\mathrm{t\bar{t}}) > 800\,\mathrm{GeV}$ and $|\cos(\theta)| < 0.4$. For this test, the parameter transformation $C_{nn} = \Delta_{\mathrm{E}} - |C_{rr} + C_{kk}|$ is applied to make Δ_{E} a parameter of L. The significances are calculated as $\sqrt{-2\Delta\log(L)}$, where $\Delta\log(L)$ is the difference between the profiled likelihood values for a fixed value of Δ_{E} and the global maximum. In Fig. 30, the scan of $-2\Delta\log(L)$ is shown as a function of Δ_{E}. The extracted significances for $\Delta_{\mathrm{E}} = 1$ and 1.2 are in close agreement with those obtained with the approximate method.

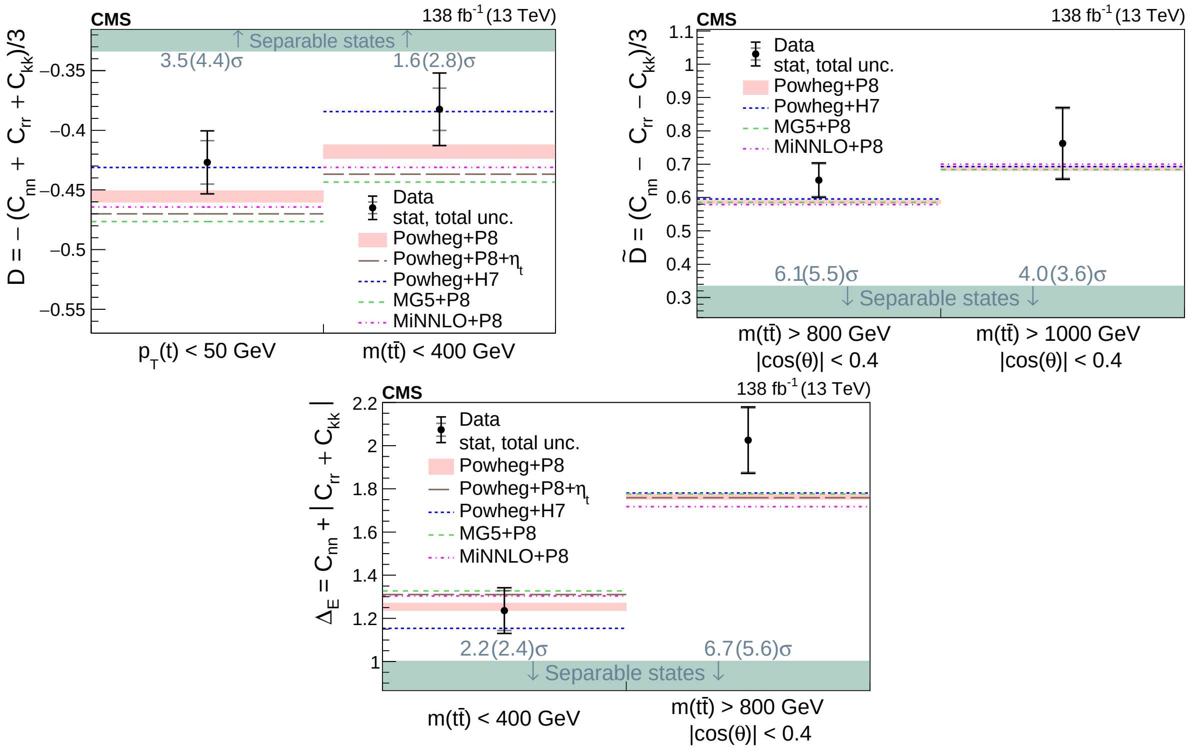

Figure 28: Entanglement results for the D measurement in the threshold region (upper left), $\tilde{D}$ measurement in the high-$m(\mathrm{t\bar{t}})$ region (upper right), and the full matrix measurement in different $m(\mathrm{t\bar{t}})$ regions (lower). The measurements (points) are shown with the statistical uncertainty (inner error bars) and total uncertainty (outer error bars) and compared to the predictions of POWHEG+PYTHIA, POWHEG+PYTHIA+η_t, POWHEG+HERWIG, MADGRAPH5_aMC@NLO+PYTHIA, and MINNLO+PYTHIA. The POWHEG+PYTHIA prediction is displayed with the ME scale and PDF uncertainties, while for all other predictions only the central values are indicated. The observed (expected) significance of the deviation from the boundary of separable states (green region) is quoted in standard deviations (σ).

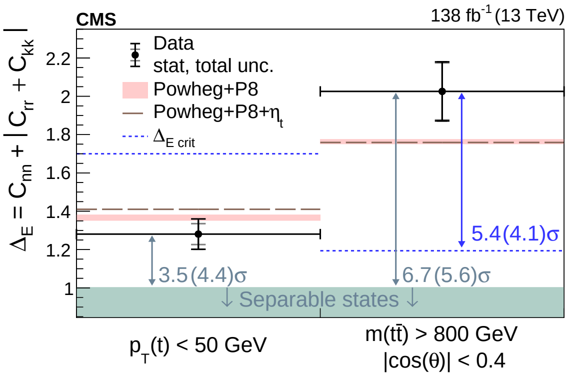

Figure 29: The observed levels of entanglement characterized by Δ_E are shown in the threshold region using the D measurement (first bin), and in the high-$m(t\bar{t})$ region using the full matrix measurement (second bin). The measurements (points) are shown with the statistical uncertainty (inner error bars) and total uncertainty (outer error bars) and compared to the predictions of POWHEG+PYTHIA, POWHEG+PYTHIA+η_t. The POWHEG+PYTHIA prediction is displayed with the ME scale and PDF uncertainties. The horizontal blue lines correspond to the maximum level of entanglement $\Delta_{E\,crit}$ that can be explained by the exchange of information between t and $\bar{t}$ at the speed of light. The significance in standard deviations (σ) by which the measurement exceeds $\Delta_{E\,crit}$ and unity is quoted in blue and light green, respectively, and indicated by the corresponding arrows.

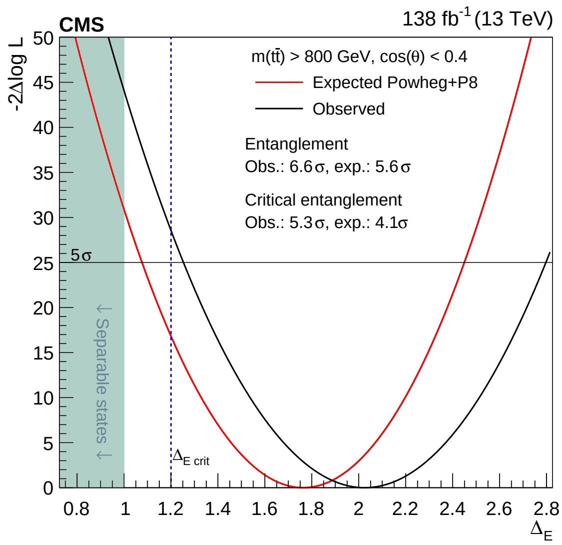

Figure 30: Results of the profile likelihood scans. The quantity $-2\Delta\log(L)$ is shown as function of Δ_E in the bin with $m(t\bar{t}) > 800\,\text{GeV}$ and $|\cos(\theta)| < 0.4$ for data (black line) and the POWHEG+PYTHIA simulation (red line). The observed and expected significances in standard deviations (σ) for Δ_E exceeding unity and $\Delta_{E\,crit}$ are quoted.

11 Summary

The polarization and spin correlation in top quark pair ($t\bar{t}$) production are measured in events with an electron or a muon plus jets in the final state. The entanglement between the spins of the top quark and antiquark is determined from the measured spin correlation by applying the Peres–Horodecki criterion. The measurements are based on proton-proton collision data at $\sqrt{s} = 13\,\text{TeV}$ collected by the CMS experiment at the LHC, corresponding to an integrated luminosity of $138\,\text{fb}^{-1}$. The decay products of the top quarks are identified using an artificial neural network. The coefficients of the polarization vectors and the spin correlation matrix are extracted simultaneously from the angular distributions of $t\bar{t}$ decay products using a binned likelihood fit. This is done both inclusively and in various regions of the phase space. The observed polarization and spin correlation are in agreement with the standard model expectations. The standard model predicts entangled $t\bar{t}$ states at the production threshold and at high masses of the $t\bar{t}$ system. Entanglement is observed in events with high $t\bar{t}$ mass, with an observed (expected) significance of 6.7 (5.6) standard deviations, while in events with low transverse momentum of the top quark a significance of 3.5 (4.4) standard deviations is observed (expected). This is the first observation of entanglement at high $t\bar{t}$ mass where in about 90% of the observed $t\bar{t}$ events the decays of the top quark and antiquark are space-like separated.

Acknowledgments

We congratulate our colleagues in the CERN accelerator departments for the excellent performance of the LHC and thank the technical and administrative staffs at CERN and at other CMS institutes for their contributions to the success of the CMS effort. In addition, we gratefully acknowledge the computing centers and personnel of the Worldwide LHC Computing Grid and other centers for delivering so effectively the computing infrastructure essential to our analyses. Finally, we acknowledge the enduring support for the construction and operation of the LHC, the CMS detector, and the supporting computing infrastructure provided by the following funding agencies: SC (Armenia), BMBWF and FWF (Austria); FNRS and FWO (Belgium); CNPq, CAPES, FAPERJ, FAPERGS, and FAPESP (Brazil); MES and BNSF (Bulgaria); CERN; CAS, MoST, and NSFC (China); MINCIENCIAS (Colombia); MSES and CSF (Croatia); RIF (Cyprus); SENESCYT (Ecuador); ERC PRG, RVTT3 and MoER TK202 (Estonia); Academy of Finland, MEC, and HIP (Finland); CEA and CNRS/IN2P3 (France); SRNSF (Georgia); BMBF, DFG, and HGF (Germany); GSRI (Greece); NKFIH (Hungary); DAE and DST (India); IPM (Iran); SFI (Ireland); INFN (Italy); MSIP and NRF (Republic of Korea); MES (Latvia); LMTLT (Lithuania); MOE and UM (Malaysia); BUAP, CINVESTAV, CONACYT, LNS, SEP, and UASLP-FAI (Mexico); MOS (Montenegro); MBIE (New Zealand); PAEC (Pakistan); MES and NSC (Poland); FCT (Portugal); MESTD (Serbia); MCIN/AEI and PCTI (Spain); MOSTR (Sri Lanka); Swiss Funding Agencies (Switzerland); MST (Taipei); MHESI and NSTDA (Thailand); TUBITAK and TENMAK (Turkey); NASU (Ukraine); STFC (United Kingdom); DOE and NSF (USA).

Individuals have received support from the Marie-Curie program and the European Research Council and Horizon 2020 Grant, contract Nos. 675440, 724704, 752730, 758316, 765710, 824093, 101115353, 101002207, and COST Action CA16108 (European Union); the Leventis Foundation; the Alfred P. Sloan Foundation; the Alexander von Humboldt Foundation; the Science Committee, project no. 22rl-037 (Armenia); the Belgian Federal Science Policy Office; the Fonds pour la Formation à la Recherche dans l'Industrie et dans l'Agriculture (FRIA-Belgium); the F.R.S.-FNRS and FWO (Belgium) under the "Excellence of Science – EOS" – be.h project n. 30820817; the Beijing Municipal Science & Technology Commission, No. Z191100007219010 and Fundamental Research Funds for the Central Universities (China); the Ministry of Education, Youth and Sports (MEYS) of the Czech Republic; the Shota Rustaveli National Science Foundation, grant FR-22-985 (Georgia); the Deutsche Forschungsgemeinschaft (DFG), among others, under Germany's Excellence Strategy – EXC 2121 "Quantum Universe" – 390833306, and under project number 400140256 - GRK2497; the Hellenic Foundation for Research and Innovation (HFRI), Project Number 2288 (Greece); the Hungarian Academy of Sciences, the New National Excellence Program - ÚNKP, the NKFIH research grants K 131991, K 133046, K 138136, K 143460, K 143477, K 146913, K 146914, K 147048, 2020-2.2.1-ED-2021-00181, and TKP2021-NKTA-64 (Hungary); the Council of Science and Industrial Research, India; ICSC – National Research Center for High Performance Computing, Big Data and Quantum Computing and FAIR – Future Artificial Intelligence Research, funded by the NextGenerationEU program (Italy); the Latvian Council of Science; the Ministry of Education and Science, project no. 2022/WK/14, and the National Science Center, contracts Opus 2021/41/B/ST2/01369 and 2021/43/B/ST2/01552 (Poland); the Fundação para a Ciência e a Tecnologia, grant CEECIND/01334/2018 (Portugal); the National Priorities Research Program by Qatar National Research Fund; MCIN/AEI/10.13039/501100011033, ERDF "a way of making Europe", and the Programa Estatal de Fomento de la Investigación Científica y Técnica de Excelencia María de Maeztu, grant MDM-2017-0765 and Programa Severo Ochoa del Principado de Asturias (Spain); the Chulalongkorn Academic into Its 2nd Century Project Advancement Project, and the National Science, Research and Innovation Fund via the Program Management Unit for Human Resources & Institutional Development, Research and Innovation, grant B39G670016 (Thailand); the Kavli Foundation; the Nvidia Corporation; the SuperMicro Corporation; the Welch Foundation, contract C-1845; and the Weston Havens Foundation (USA).

References

[1] Particle Data Group, S. Navas et al., "Review of particle physics", *Phys. Rev. D* **110** (2024) 030001, doi:10.1103/PhysRevD.110.030001.

[2] G. Mahlon and S. J. Parke, "Spin correlation effects in top quark pair production at the LHC", *Phys. Rev. D* **81** (2010) 074024, doi:10.1103/PhysRevD.81.074024, arXiv:1001.3422.

[3] M. Baumgart and B. Tweedie, "A new twist on top quark spin correlations", *JHEP* **03** (2013) 117, doi:10.1007/JHEP03(2013)117, arXiv:1212.4888.

[4] D0 Collaboration, "Evidence for spin correlation in $\mathrm{t\bar{t}}$ production", *Phys. Rev. Lett.* **108** (2012) 032004, doi:10.1103/PhysRevLett.108.032004, arXiv:1110.4194.

[5] D0 Collaboration, "Measurement of spin correlation between top and antitop quarks produced in $\mathrm{p\overline{p}}$ collisions at $\sqrt{s} = 1.96\,\mathrm{TeV}$", *Phys. Lett. B* **757** (2016) 199, doi:10.1016/j.physletb.2016.03.053, arXiv:1512.08818.

[6] CMS Collaboration, "Measurements of $\mathrm{t\bar{t}}$ spin correlations and top-quark polarization using dilepton final states in pp collisions at $\sqrt{s} = 7\,\mathrm{TeV}$", *Phys. Rev. Lett.* **112** (2014) 182001, doi:10.1103/PhysRevLett.112.182001, arXiv:1311.3924.

[7] CMS Collaboration, "Measurement of spin correlations in $\mathrm{t\bar{t}}$ production using the matrix element method in the muon+jets final state in pp collisions at $\sqrt{s} = 8\,\mathrm{TeV}$", *Phys. Lett. B* **758** (2016) 321, doi:10.1016/j.physletb.2016.05.005, arXiv:1511.06170.

[8] CMS Collaboration, “Measurements of $t\bar{t}$ spin correlations and top quark polarization using dilepton final states in pp collisions at $\sqrt{s} = 8\,\text{TeV}$”, *Phys. Rev. D* **93** (2016) 052007, doi:10.1103/PhysRevD.93.052007, arXiv:1601.01107.

[9] CMS Collaboration, “Measurement of the top quark polarization and $t\bar{t}$ spin correlations using dilepton final states in proton-proton collisions at $\sqrt{s} = 13\,\text{TeV}$”, *Phys. Rev. D* **100** (2019) 072002, doi:10.1103/PhysRevD.100.072002, arXiv:1907.03729.

[10] ATLAS Collaboration, “Observation of spin correlation in $t\bar{t}$ events from pp collisions at $\sqrt(s) = 7\,\text{TeV}$ using the ATLAS detector”, *Phys. Rev. Lett.* **108** (2012) 212001, doi:10.1103/PhysRevLett.108.212001, arXiv:1203.4081.

[11] ATLAS Collaboration, “Measurement of spin correlation in top-antitop quark events and search for top squark pair production in pp collisions at $\sqrt{s} = 8\,\text{TeV}$ using the ATLAS detector”, *Phys. Rev. Lett.* **114** (2015) 142001, doi:10.1103/PhysRevLett.114.142001, arXiv:1412.4742.

[12] ATLAS Collaboration, “Measurements of spin correlation in top-antitop quark events from proton-proton collisions at $\sqrt{s} = 7\,\text{TeV}$ using the ATLAS detector”, *Phys. Rev. D* **90** (2014) 112016, doi:10.1103/PhysRevD.90.112016, arXiv:1407.4314.

[13] ATLAS Collaboration, “Measurements of top-quark pair spin correlations in the $e\mu$ channel at $\sqrt{s} = 13\,\text{TeV}$ using pp collisions in the ATLAS detector”, *Eur. Phys. J. C* **80** (2020) 754, doi:10.1140/epjc/s10052-020-8181-6, arXiv:1903.07570.

[14] ATLAS Collaboration, “Observation of quantum entanglement in top-quark pairs using the ATLAS detector”, 2023. arXiv:2311.07288. Submitted to *Nature*.

[15] CMS Collaboration, “Observation of quantum entanglement in top quark pair production in proton-proton collisions at $\sqrt{s} = 13\,\text{TeV}$”, 2024. arXiv:2406.03976. Submitted to *Rep. Prog. Phys.*

[16] L. Wu and H. Zhou, “Polarization of top and chargino from stop decay in natural SUSY”, *Phys. Lett. B* **794** (2019) 96, doi:10.1016/j.physletb.2019.05.033, arXiv:1811.08573.

[17] F. Maltoni, C. Severi, S. Tentori, and E. Vryonidou, “Quantum detection of new physics in top-quark pair production at the LHC”, *JHEP* **03** (2024) 099, doi:10.1007/JHEP03(2024)099, arXiv:2401.08751.

[18] Y. Afik and J. R. M. de Nova, “Entanglement and quantum tomography with top quarks at the LHC”, *Eur. Phys. J. Plus* **136** (2021) 907, doi:10.1140/epjp/s13360-021-01902-1, arXiv:2003.02280.

[19] M. Fabbrichesi, R. Floreanini, and E. Gabrielli, “Constraining new physics in entangled two-qubit systems: top-quark, tau-lepton and photon pairs”, *Eur. Phys. J. C* **83** (2023) 162, doi:10.1140/epjc/s10052-023-11307-2, arXiv:2208.11723.

[20] M. Fabbrichesi, R. Floreanini, and G. Panizzo, “Testing Bell inequalities at the LHC with top-quark pairs”, *Phys. Rev. Lett.* **127** (2021) 161801, doi:10.1103/PhysRevLett.127.161801, arXiv:2102.11883.

[21] Z. Dong, D. Gonçalves, K. Kong, and A. Navarro, “Entanglement and Bell inequalities with boosted $t\bar{t}$”, *Phys. Rev. D* **109** (2024) 115023, doi:10.1103/PhysRevD.109.115023, arXiv:2305.07075.

[22] HEPData record for this analysis, 2024. doi:10.17182/hepdata.153301.

[23] W. Bernreuther, D. Heisler, and Z.-G. Si, “A set of top quark spin correlation and polarization observables for the LHC: Standard model predictions and new physics contributions”, *JHEP* **12** (2015) 026, doi:10.1007/JHEP12(2015)026, arXiv:1508.05271.

[24] A. Brandenburg, Z. G. Si, and P. Uwer, “QCD-corrected spin analysing power of jets in decays of polarized top quarks”, *Phys. Lett. B* **539** (2002) 235, doi:10.1016/S0370-2693(02)02098-1, arXiv:hep-ph/0205023.

[25] A. Peres, “Separability criterion for density matrices”, *Phys. Rev. Lett.* **77** (1996) 1413, doi:10.1103/PhysRevLett.77.1413, arXiv:quant-ph/9604005.

[26] P. Horodecki, “Separability criterion and inseparable mixed states with positive partial transposition”, *Phys. Lett. A* **232** (1997) 333, doi:10.1016/S0375-9601(97)00416-7, arXiv:quant-ph/9703004.

[27] Y. Afik and J. R. M. de Nova, “Quantum information with top quarks in QCD”, *Quantum* **6** (2022) 820, doi:10.22331/q-2022-09-29-820, arXiv:2203.05582.

[28] J. A. Aguilar-Saavedra and J. A. Casas, “Improved tests of entanglement and Bell inequalities with LHC tops”, *Eur. Phys. J. C* **82** (2022) 666, doi:10.1140/epjc/s10052-022-10630-4, arXiv:2205.00542.

[29] CMS Collaboration, “Performance of the CMS Level-1 trigger in proton-proton collisions at $\sqrt{s} = 13\,\text{TeV}$”, *JINST* **15** (2020) P10017, doi:10.1088/1748-0221/15/10/P10017, arXiv:2006.10165.

[30] CMS Collaboration, “The CMS trigger system”, *JINST* **12** (2017) P01020, doi:10.1088/1748-0221/12/01/P01020, arXiv:1609.02366.

[31] CMS Collaboration, “Technical proposal for the Phase-II upgrade of the Compact Muon Solenoid”, CMS Technical Proposal CERN-LHCC-2015-010, CMS-TDR-15-02, 2015. doi:10.17181/CERN.VU8I.D59J.

[32] CMS Collaboration, “Particle-flow reconstruction and global event description with the CMS detector”, *JINST* **12** (2017) P10003, doi:10.1088/1748-0221/12/10/P10003, arXiv:1706.04965.

[33] CMS Collaboration, “The CMS experiment at the CERN LHC”, *JINST* **3** (2008) S08004, doi:10.1088/1748-0221/3/08/S08004.

[34] P. Nason, “A new method for combining NLO QCD with shower Monte Carlo algorithms”, *JHEP* **11** (2004) 040, doi:10.1088/1126-6708/2004/11/040, arXiv:hep-ph/0409146.

[35] S. Frixione, P. Nason, and C. Oleari, “Matching NLO QCD computations with parton shower simulations: the POWHEG method”, *JHEP* **11** (2007) 070, doi:10.1088/1126-6708/2007/11/070, arXiv:0709.2092.

[36] S. Frixione, G. Ridolfi, and P. Nason, “A positive-weight next-to-leading-order Monte Carlo for heavy flavour hadroproduction”, *JHEP* **09** (2007) 126, doi:10.1088/1126-6708/2007/09/126, arXiv:0707.3088.

[37] T. Sjöstrand et al., "An introduction to PYTHIA 8.2", *Comput. Phys. Commun.* **191** (2015) 159, doi:10.1016/j.cpc.2015.01.024, arXiv:1410.3012.

[38] CMS Collaboration, "Extraction and validation of a new set of CMS PYTHIA 8 tunes from underlying-event measurements", *Eur. Phys. J. C* **80** (2020) 4, doi:10.1140/epjc/s10052-019-7499-4, arXiv:1903.12179.

[39] J. Mazzitelli et al., "Next-to-next-to-leading order event generation for top-quark pair production", *Phys. Rev. Lett.* **127** (2021) 062001, doi:10.1103/PhysRevLett.127.062001, arXiv:2012.14267.

[40] M. Aliev et al., "HATHOR: Hadronic top and heavy quarks cross section calculator", *Comput. Phys. Commun.* **182** (2011) 1034, doi:10.1016/j.cpc.2010.12.040, arXiv:1007.1327.

[41] M. Bähr et al., "HERWIG++ physics and manual", *Eur. Phys. J. C* **58** (2008) 639, doi:10.1140/epjc/s10052-008-0798-9, arXiv:0803.0883.

[42] CMS Collaboration, "Development and validation of HERWIG 7 tunes from CMS underlying-event measurements", *Eur. Phys. J. C* **81** (2021) 312, doi:10.1140/epjc/s10052-021-08949-5, arXiv:2011.03422.

[43] J. Alwall et al., "The automated computation of tree-level and next-to-leading order differential cross sections, and their matching to parton shower simulations", *JHEP* **07** (2014) 079, doi:10.1007/JHEP07(2014)079, arXiv:1405.0301.

[44] R. Frederix and S. Frixione, "Merging meets matching in MC@NLO", *JHEP* **12** (2012) 061, doi:10.1007/JHEP12(2012)061, arXiv:1209.6215.

[45] M. Czakon and A. Mitov, "TOP++: a program for the calculation of the top-pair cross-section at hadron colliders", *Comput. Phys. Commun.* **185** (2014) 2930, doi:10.1016/j.cpc.2014.06.021, arXiv:1112.5675.

[46] CMS Collaboration, "Measurement of the top quark mass using proton-proton data at $\sqrt{s} = 7$ and 8 TeV", *Phys. Rev. D* **93** (2016) 072004, doi:10.1103/PhysRevD.93.072004, arXiv:1509.04044.

[47] M. L. Mangano, M. Moretti, F. Piccinini, and M. Treccani, "Matching matrix elements and shower evolution for top-pair production in hadronic collisions", *JHEP* **01** (2007) 013, doi:10.1088/1126-6708/2007/01/013, arXiv:hep-ph/0611129.

[48] J. Alwall et al., "Comparative study of various algorithms for the merging of parton showers and matrix elements in hadronic collisions", *Eur. Phys. J. C* **53** (2008) 473, doi:10.1140/epjc/s10052-007-0490-5, arXiv:0706.2569.

[49] Y. Li and F. Petriello, "Combining QCD and electroweak corrections to dilepton production in FEWZ", *Phys. Rev. D* **86** (2012) 094034, doi:10.1103/PhysRevD.86.094034, arXiv:1208.5967.

[50] P. Kant et al., "HATHOR for single top-quark production: Updated predictions and uncertainty estimates for single top-quark production in hadronic collisions", *Comput. Phys. Commun.* **191** (2015) 74, doi:10.1016/j.cpc.2015.02.001, arXiv:1406.4403.

[51] N. Kidonakis, "NNLL threshold resummation for top-pair and single-top production", *Phys. Part. Nucl.* **45** (2014) 714, doi:10.1134/S1063779614040091, arXiv:1210.7813.

[52] NNPDF Collaboration, "Parton distributions from high-precision collider data", *Eur. Phys. J. C* **77** (2017) 663, doi:10.1140/epjc/s10052-017-5199-5, arXiv:1706.00428.

[53] GEANT4 Collaboration, "GEANT4—a simulation toolkit", *Nucl. Instrum. Meth. A* **506** (2003) 250, doi:10.1016/S0168-9002(03)01368-8.

[54] CMS Collaboration, "Electron and photon reconstruction and identification with the CMS experiment at the CERN LHC", *JINST* **16** (2021) P05014, doi:10.1088/1748-0221/16/05/P05014, arXiv:2012.06888.

[55] CMS Collaboration, "Performance of the CMS muon detector and muon reconstruction with proton-proton collisions at $\sqrt{s} = 13\,\text{TeV}$", *JINST* **13** (2018) P06015, doi:10.1088/1748-0221/13/06/P06015, arXiv:1804.04528.

[56] CMS Collaboration, "Measurements of inclusive W and Z cross sections in pp collisions at $\sqrt{s} = 7\,\text{TeV}$", *JHEP* **01** (2011) 080, doi:10.1007/JHEP01(2011)080, arXiv:1012.2466.

[57] M. Cacciari, G. P. Salam, and G. Soyez, "The anti-k_{T} jet clustering algorithm", *JHEP* **04** (2008) 063, doi:10.1088/1126-6708/2008/04/063, arXiv:0802.1189.

[58] M. Cacciari, G. P. Salam, and G. Soyez, "FASTJET user manual", *Eur. Phys. J. C* **72** (2012) 1896, doi:10.1140/epjc/s10052-012-1896-2, arXiv:1111.6097.

[59] CMS Collaboration, "Jet energy scale and resolution in the CMS experiment in pp collisions at 8 TeV", *JINST* **12** (2017) P02014, doi:10.1088/1748-0221/12/02/P02014, arXiv:1607.03663.

[60] E. Bols et al., "Jet flavour classification using DeepJet", *JINST* **15** (2020) P12012, doi:10.1088/1748-0221/15/12/P12012, arXiv:2008.10519.

[61] CMS Collaboration, "Identification of heavy-flavour jets with the CMS detector in pp collisions at 13 TeV", *JINST* **13** (2018) P05011, doi:10.1088/1748-0221/13/05/P05011, arXiv:1712.07158.

[62] CMS Collaboration, "Performance of missing transverse momentum reconstruction in proton-proton collisions at $\sqrt{s} = 13\,\text{TeV}$ using the CMS detector", *JINST* **14** (2019) P07004, doi:10.1088/1748-0221/14/07/P07004, arXiv:1903.06078.

[63] D. P. Kingma and J. Ba, "ADAM: a method for stochastic optimization", in *Proc. 3rd Int. Conf. on Learning Representations (ICLR 2015): San Diego CA, USA, May 7–9, 2015*. 2015. arXiv:1412.6980.

[64] E. Gross and O. Vitells, "Trial factors for the look elsewhere effect in high energy physics", *Eur. Phys. J. C* **70** (2010) 525, doi:10.1140/epjc/s10052-010-1470-8, arXiv:1005.1891.

[65] A. Andreassen and B. Nachman, "Neural networks for full phase-space reweighting and parameter tuning", *Phys. Rev. D* **101** (2020) 091901, doi:10.1103/PhysRevD.101.091901, arXiv:1907.08209.

[66] CMS Collaboration, "Reweighting of simulated events using machine learning techniques in CMS", CMS Physics Analysis Summary CMS-PAS-MLG-24-001, 2024.

[67] M. Czakon, P. Fiedler, and A. Mitov, "Total top-quark pair-production cross section at hadron colliders through $\mathcal{O}(\alpha_S{}^4)$", *Phys. Rev. Lett.* **110** (2013) 252004, doi:10.1103/PhysRevLett.110.252004, arXiv:1303.6254.

[68] S. Argyropoulos and T. Sjöstrand, "Effects of color reconnection on $t\bar{t}$ final states at the LHC", *JHEP* **11** (2014) 043, doi:10.1007/JHEP11(2014)043, arXiv:1407.6653.

[69] J. R. Christiansen and P. Z. Skands, "String formation beyond leading colour", *JHEP* **08** (2015) 003, doi:10.1007/JHEP08(2015)003, arXiv:1505.01681.

[70] W.-L. Ju et al., "Top quark pair production near threshold: single/double distributions and mass determination", *JHEP* **06** (2020) 158, doi:10.1007/JHEP06(2020)158, arXiv:2004.03088.

[71] B. Fuks, K. Hagiwara, K. Ma, and Y.-J. Zheng, "Signatures of toponium formation in LHC run 2 data", *Phys. Rev. D* **104** (2021) 034023, doi:10.1103/PhysRevD.104.034023, arXiv:2102.11281.

[72] CMS Collaboration, "Precision luminosity measurement in proton-proton collisions at $\sqrt{s} = 13\,\text{TeV}$ in 2015 and 2016 at CMS", *Eur. Phys. J. C* **81** (2021) 800, doi:10.1140/epjc/s10052-021-09538-2, arXiv:2104.01927.

[73] CMS Collaboration, "CMS luminosity measurement for the 2017 data-taking period at $\sqrt{s} = 13\,\text{TeV}$", CMS Physics Analysis Summary CMS-PAS-LUM-17-004, 2018.

[74] CMS Collaboration, "CMS luminosity measurement for the 2018 data-taking period at $\sqrt{s} = 13\,\text{TeV}$", CMS Physics Analysis Summary CMS-PAS-LUM-18-002, 2019.

[75] CMS Collaboration, "Measurement of the inelastic proton-proton cross section at $\sqrt{s} = 13\,\text{TeV}$", *JHEP* **07** (2018) 161, doi:10.1007/JHEP07(2018)161, arXiv:1802.02613.

[76] CMS Collaboration, "Performance summary of AK4 jet b tagging with data from proton-proton collisions at 13 TeV with the CMS detector", CMS Detector Performance Note CMS-DP-2023-005, 2023.

[77] R. Barlow and C. Beeston, "Fitting using finite Monte Carlo samples", *Comput. Phys. Commun.* **77** (1993) 219, doi:10.1016/0010-4655(93)90005-W.

[78] W. S. Cleveland, "Robust locally weighted regression and smoothing scatterplots", *J. Am. Stat. Assoc.* **74** (1979) 829, doi:10.2307/2286407.

[79] C. Severi, C. Degli Esposti Boschi, F. Maltoni, and M. Sioli, "Quantum tops at the LHC: from entanglement to Bell inequalities", *Eur. Phys. J. C* **82** (2022) 285, doi:10.1140/epjc/s10052-022-10245-9, arXiv:2110.10112.

[80] R. Demina and G. Landi, "Locality in collider tests of quantum mechanics with top quark pairs", 2024. arXiv:2407.15223. Submitted to *Phys. Rev. Lett.*

A The CMS Collaboration

Yerevan Physics Institute, Yerevan, Armenia
A. Hayrapetyan, A. Tumasyan[1]

Institut für Hochenergiephysik, Vienna, Austria
W. Adam, J.W. Andrejkovic, L. Benato, T. Bergauer, S. Chatterjee, K. Damanakis, M. Dragicevic, P.S. Hussain, M. Jeitler[2], N. Krammer, A. Li, D. Liko, I. Mikulec, J. Schieck[2], R. Schöfbeck[2], D. Schwarz, M. Sonawane, W. Waltenberger, C.-E. Wulz[2]

Universiteit Antwerpen, Antwerpen, Belgium
T. Janssen, T. Van Laer, P. Van Mechelen

Vrije Universiteit Brussel, Brussel, Belgium
N. Breugelmans, J. D'Hondt, S. Dansana, A. De Moor, M. Delcourt, F. Heyen, S. Lowette, I. Makarenko, D. Müller, S. Tavernier, M. Tytgat[3], G.P. Van Onsem, S. Van Putte, D. Vannerom

Université Libre de Bruxelles, Bruxelles, Belgium
B. Bilin, B. Clerbaux, A.K. Das, I. De Bruyn, G. De Lentdecker, H. Evard, L. Favart, P. Gianneios, J. Jaramillo, A. Khalilzadeh, F.A. Khan, K. Lee, A. Malara, S. Paredes, M.A. Shahzad, L. Thomas, M. Vanden Bemden, C. Vander Velde, P. Vanlaer

Ghent University, Ghent, Belgium
M. De Coen, D. Dobur, G. Gokbulut, Y. Hong, J. Knolle, L. Lambrecht, D. Marckx, K. Mota Amarilo, K. Skovpen, N. Van Den Bossche, J. van der Linden, L. Wezenbeek

Université Catholique de Louvain, Louvain-la-Neuve, Belgium
A. Benecke, A. Bethani, G. Bruno, C. Caputo, J. De Favereau De Jeneret, C. Delaere, I.S. Donertas, A. Giammanco, A.O. Guzel, Sa. Jain, V. Lemaitre, J. Lidrych, P. Mastrapasqua, T.T. Tran, S. Turkcapar

Centro Brasileiro de Pesquisas Fisicas, Rio de Janeiro, Brazil
G.A. Alves, E. Coelho, G. Correia Silva, C. Hensel, T. Menezes De Oliveira, C. Mora Herrera[4], P. Rebello Teles, M. Soeiro, E.J. Tonelli Manganote[5], A. Vilela Pereira[4]

Universidade do Estado do Rio de Janeiro, Rio de Janeiro, Brazil
W.L. Aldá Júnior, M. Barroso Ferreira Filho, H. Brandao Malbouisson, W. Carvalho, J. Chinellato[6], E.M. Da Costa, G.G. Da Silveira[7], D. De Jesus Damiao, S. Fonseca De Souza, R. Gomes De Souza, T. Laux Kuhn[7], M. Macedo, J. Martins, L. Mundim, H. Nogima, J.P. Pinheiro, A. Santoro, A. Sznajder, M. Thiel

Universidade Estadual Paulista, Universidade Federal do ABC, São Paulo, Brazil
C.A. Bernardes[7], L. Calligaris, T.R. Fernandez Perez Tomei, E.M. Gregores, I. Maietto Silverio, P.G. Mercadante, S.F. Novaes, B. Orzari, Sandra S. Padula

Institute for Nuclear Research and Nuclear Energy, Bulgarian Academy of Sciences, Sofia, Bulgaria
A. Aleksandrov, G. Antchev, R. Hadjiiska, P. Iaydjiev, M. Misheva, M. Shopova, G. Sultanov

University of Sofia, Sofia, Bulgaria
A. Dimitrov, L. Litov, B. Pavlov, P. Petkov, A. Petrov, E. Shumka

Instituto De Alta Investigación, Universidad de Tarapacá, Casilla 7 D, Arica, Chile
S. Keshri, D. Laroze, S. Thakur

Beihang University, Beijing, China
T. Cheng, T. Javaid, L. Yuan

Department of Physics, Tsinghua University, Beijing, China
Z. Hu, Z. Liang, J. Liu

Institute of High Energy Physics, Beijing, China
G.M. Chen[8], H.S. Chen[8], M. Chen[8], F. Iemmi, C.H. Jiang, A. Kapoor[9], H. Liao, Z.-A. Liu[10], R. Sharma[11], J.N. Song[10], J. Tao, C. Wang[8], J. Wang, Z. Wang[8], H. Zhang, J. Zhao

State Key Laboratory of Nuclear Physics and Technology, Peking University, Beijing, China
A. Agapitos, Y. Ban, S. Deng, B. Guo, C. Jiang, A. Levin, C. Li, Q. Li, Y. Mao, S. Qian, S.J. Qian, X. Qin, X. Sun, D. Wang, H. Yang, L. Zhang, Y. Zhao, C. Zhou

Guangdong Provincial Key Laboratory of Nuclear Science and Guangdong-Hong Kong Joint Laboratory of Quantum Matter, South China Normal University, Guangzhou, China
S. Yang

Sun Yat-Sen University, Guangzhou, China
Z. You

University of Science and Technology of China, Hefei, China
K. Jaffel, N. Lu

Nanjing Normal University, Nanjing, China
G. Bauer[12], B. Li[13], K. Yi[14], J. Zhang

Institute of Modern Physics and Key Laboratory of Nuclear Physics and Ion-beam Application (MOE) - Fudan University, Shanghai, China
Y. Li

Zhejiang University, Hangzhou, Zhejiang, China
Z. Lin, C. Lu, M. Xiao

Universidad de Los Andes, Bogota, Colombia
C. Avila, D.A. Barbosa Trujillo, A. Cabrera, C. Florez, J. Fraga, J.A. Reyes Vega

Universidad de Antioquia, Medellin, Colombia
F. Ramirez, C. Rendón, M. Rodriguez, A.A. Ruales Barbosa, J.D. Ruiz Alvarez

University of Split, Faculty of Electrical Engineering, Mechanical Engineering and Naval Architecture, Split, Croatia
D. Giljanovic, N. Godinovic, D. Lelas, A. Sculac

University of Split, Faculty of Science, Split, Croatia
M. Kovac, A. Petkovic, T. Sculac

Institute Rudjer Boskovic, Zagreb, Croatia
P. Bargassa, V. Brigljevic, B.K. Chitroda, D. Ferencek, K. Jakovcic, A. Starodumov[15], T. Susa

University of Cyprus, Nicosia, Cyprus
A. Attikis, K. Christoforou, A. Hadjiagapiou, C. Leonidou, J. Mousa, C. Nicolaou, L. Paizanos, F. Ptochos, P.A. Razis, H. Rykaczewski, H. Saka, A. Stepennov

Charles University, Prague, Czech Republic
M. Finger, M. Finger Jr., A. Kveton

Universidad San Francisco de Quito, Quito, Ecuador
E. Carrera Jarrin

Academy of Scientific Research and Technology of the Arab Republic of Egypt, Egyptian Network of High Energy Physics, Cairo, Egypt
Y. Assran[16,17], B. El-mahdy, S. Elgammal[17]

Center for High Energy Physics (CHEP-FU), Fayoum University, El-Fayoum, Egypt
M. Abdullah Al-Mashad, M.A. Mahmoud

National Institute of Chemical Physics and Biophysics, Tallinn, Estonia
K. Ehataht, M. Kadastik, T. Lange, S. Nandan, C. Nielsen, J. Pata, M. Raidal, L. Tani, C. Veelken

Department of Physics, University of Helsinki, Helsinki, Finland
H. Kirschenmann, K. Osterberg, M. Voutilainen

Helsinki Institute of Physics, Helsinki, Finland
S. Bharthuar, N. Bin Norjoharuddeen, E. Brücken, F. Garcia, P. Inkaew, K.T.S. Kallonen, T. Lampén, K. Lassila-Perini, S. Lehti, T. Lindén, M. Myllymäki, M.m. Rantanen, H. Siikonen, J. Tuominiemi

Lappeenranta-Lahti University of Technology, Lappeenranta, Finland
P. Luukka, H. Petrow

IRFU, CEA, Université Paris-Saclay, Gif-sur-Yvette, France
M. Besancon, F. Couderc, M. Dejardin, D. Denegri, J.L. Faure, F. Ferri, S. Ganjour, P. Gras, G. Hamel de Monchenault, M. Kumar, V. Lohezic, J. Malcles, F. Orlandi, L. Portales, A. Rosowsky, M.Ö. Sahin, A. Savoy-Navarro[18], P. Simkina, M. Titov, M. Tornago

Laboratoire Leprince-Ringuet, CNRS/IN2P3, Ecole Polytechnique, Institut Polytechnique de Paris, Palaiseau, France
F. Beaudette, G. Boldrini, P. Busson, A. Cappati, C. Charlot, M. Chiusi, T.D. Cuisset, F. Damas, O. Davignon, A. De Wit, I.T. Ehle, B.A. Fontana Santos Alves, S. Ghosh, A. Gilbert, R. Granier de Cassagnac, A. Hakimi, B. Harikrishnan, L. Kalipoliti, G. Liu, M. Nguyen, C. Ochando, R. Salerno, J.B. Sauvan, Y. Sirois, L. Urda Gómez, E. Vernazza, A. Zabi, A. Zghiche

Université de Strasbourg, CNRS, IPHC UMR 7178, Strasbourg, France
J.-L. Agram[19], J. Andrea, D. Apparu, D. Bloch, J.-M. Brom, E.C. Chabert, C. Collard, S. Falke, U. Goerlach, R. Haeberle, A.-C. Le Bihan, M. Meena, O. Poncet, G. Saha, M.A. Sessini, P. Van Hove, P. Vaucelle

Centre de Calcul de l'Institut National de Physique Nucleaire et de Physique des Particules, CNRS/IN2P3, Villeurbanne, France
A. Di Florio

Institut de Physique des 2 Infinis de Lyon (IP2I), Villeurbanne, France

D. Amram, S. Beauceron, B. Blancon, G. Boudoul, N. Chanon, D. Contardo, P. Depasse, C. Dozen[20], H. El Mamouni, J. Fay, S. Gascon, M. Gouzevitch, C. Greenberg, G. Grenier, B. Ille, E. Jourd'huy, M. Lethuillier, L. Mirabito, S. Perries, A. Purohit, M. Vander Donckt, P. Verdier, J. Xiao

Georgian Technical University, Tbilisi, Georgia
A. Khvedelidze[15], I. Lomidze, Z. Tsamalaidze[15]

RWTH Aachen University, I. Physikalisches Institut, Aachen, Germany
V. Botta, S. Consuegra Rodríguez, L. Feld, K. Klein, M. Lipinski, D. Meuser, A. Pauls, D. Pérez Adán, N. Röwert, M. Teroerde

RWTH Aachen University, III. Physikalisches Institut A, Aachen, Germany
S. Diekmann, A. Dodonova, N. Eich, D. Eliseev, F. Engelke, J. Erdmann, M. Erdmann, P. Fackeldey, B. Fischer, T. Hebbeker, K. Hoepfner, F. Ivone, A. Jung, M.y. Lee, F. Mausolf, M. Merschmeyer, A. Meyer, S. Mukherjee, D. Noll, F. Nowotny, A. Pozdnyakov, Y. Rath, W. Redjeb, F. Rehm, H. Reithler, V. Sarkisovi, A. Schmidt, C. Seth, A. Sharma, J.L. Spah, A. Stein, F. Torres Da Silva De Araujo[21], S. Wiedenbeck, S. Zaleski

RWTH Aachen University, III. Physikalisches Institut B, Aachen, Germany
C. Dziwok, G. Flügge, T. Kress, A. Nowack, O. Pooth, A. Stahl, T. Ziemons, A. Zotz

Deutsches Elektronen-Synchrotron, Hamburg, Germany
H. Aarup Petersen, M. Aldaya Martin, J. Alimena, S. Amoroso, Y. An, J. Bach, S. Baxter, M. Bayatmakou, H. Becerril Gonzalez, O. Behnke, A. Belvedere, F. Blekman[22], K. Borras[23], A. Campbell, A. Cardini, C. Cheng, F. Colombina, G. Eckerlin, D. Eckstein, L.I. Estevez Banos, E. Gallo[22], A. Geiser, V. Guglielmi, M. Guthoff, A. Hinzmann, L. Jeppe, B. Kaech, M. Kasemann, C. Kleinwort, R. Kogler, M. Komm, D. Krücker, W. Lange, D. Leyva Pernia, K. Lipka[24], W. Lohmann[25], F. Lorkowski, R. Mankel, I.-A. Melzer-Pellmann, M. Mendizabal Morentin, A.B. Meyer, G. Milella, K. Moral Figueroa, A. Mussgiller, L.P. Nair, J. Niedziela, A. Nürnberg, Y. Otarid, J. Park, E. Ranken, A. Raspereza, D. Rastorguev, J. Rübenach, L. Rygaard, A. Saggio, M. Scham[26,23], S. Schnake[23], P. Schütze, C. Schwanenberger[22], D. Selivanova, K. Sharko, M. Shchedrolosiev, D. Stafford, F. Vazzoler, A. Ventura Barroso, R. Walsh, D. Wang, Q. Wang, K. Wichmann, L. Wiens[23], C. Wissing, Y. Yang, A. Zimermmane Castro Santos

University of Hamburg, Hamburg, Germany
A. Albrecht, S. Albrecht, M. Antonello, S. Bein, S. Bollweg, M. Bonanomi, P. Connor, K. El Morabit, Y. Fischer, E. Garutti, A. Grohsjean, J. Haller, D. Hundhausen, H.R. Jabusch, G. Kasieczka, P. Keicher, R. Klanner, W. Korcari, T. Kramer, C.c. Kuo, V. Kutzner, F. Labe, J. Lange, A. Lobanov, C. Matthies, L. Moureaux, M. Mrowietz, A. Nigamova, Y. Nissan, A. Paasch, K.J. Pena Rodriguez, T. Quadfasel, B. Raciti, M. Rieger, D. Savoiu, J. Schindler, P. Schleper, M. Schröder, J. Schwandt, M. Sommerhalder, H. Stadie, G. Steinbrück, A. Tews, B. Wiederspan, M. Wolf

Karlsruher Institut fuer Technologie, Karlsruhe, Germany
S. Brommer, E. Butz, T. Chwalek, A. Dierlamm, A. Droll, U. Elicabuk, N. Faltermann, M. Giffels, A. Gottmann, F. Hartmann[27], R. Hofsaess, M. Horzela, U. Husemann, J. Kieseler, M. Klute, R. Koppenhöfer, O. Lavoryk, J.M. Lawhorn,

M. Link, A. Lintuluoto, S. Maier, S. Mitra, M. Mormile, Th. Müller, M. Neukum, M. Oh, E. Pfeffer, M. Presilla, G. Quast, K. Rabbertz, B. Regnery, N. Shadskiy, I. Shvetsov, H.J. Simonis, L. Sowa, L. Stockmeier, K. Tauqeer, M. Toms, N. Trevisani, R.F. Von Cube, M. Wassmer, S. Wieland, F. Wittig, R. Wolf, X. Zuo

Institute of Nuclear and Particle Physics (INPP), NCSR Demokritos, Aghia Paraskevi, Greece
G. Anagnostou, G. Daskalakis, A. Kyriakis, A. Papadopoulos[27], A. Stakia

National and Kapodistrian University of Athens, Athens, Greece
P. Kontaxakis, G. Melachroinos, Z. Painesis, I. Papavergou, I. Paraskevas, N. Saoulidou, K. Theofilatos, E. Tziaferi, K. Vellidis, I. Zisopoulos

National Technical University of Athens, Athens, Greece
G. Bakas, T. Chatzistavrou, G. Karapostoli, K. Kousouris, I. Papakrivopoulos, E. Siamarkou, G. Tsipolitis, A. Zacharopoulou

University of Ioánnina, Ioánnina, Greece
I. Bestintzanos, I. Evangelou, C. Foudas, C. Kamtsikis, P. Katsoulis, P. Kokkas, P.G. Kosmoglou Kioseoglou, N. Manthos, I. Papadopoulos, J. Strologas

HUN-REN Wigner Research Centre for Physics, Budapest, Hungary
C. Hajdu, D. Horvath[28,29], K. Márton, A.J. Rádl[30], F. Sikler, V. Veszpremi

MTA-ELTE Lendület CMS Particle and Nuclear Physics Group, Eötvös Loránd University, Budapest, Hungary
M. Csanád, K. Farkas, A. Fehérkuti[31], M.M.A. Gadallah[32], Á. Kadlecsik, P. Major, G. Pásztor, G.I. Veres

Faculty of Informatics, University of Debrecen, Debrecen, Hungary
B. Ujvari, G. Zilizi

Institute of Nuclear Research ATOMKI, Debrecen, Hungary
G. Bencze, S. Czellar, J. Molnar, Z. Szillasi

Karoly Robert Campus, MATE Institute of Technology, Gyongyos, Hungary
F. Nemes[31], T. Novak

Panjab University, Chandigarh, India
S. Bansal, S.B. Beri, V. Bhatnagar, G. Chaudhary, S. Chauhan, N. Dhingra[33], A. Kaur, A. Kaur, H. Kaur, M. Kaur, S. Kumar, T. Sheokand, J.B. Singh, A. Singla

University of Delhi, Delhi, India
A. Ahmed, A. Bhardwaj, A. Chhetri, B.C. Choudhary, A. Kumar, A. Kumar, M. Naimuddin, K. Ranjan, M.K. Saini, S. Saumya

Saha Institute of Nuclear Physics, HBNI, Kolkata, India
S. Baradia, S. Barman[34], S. Bhattacharya, S. Das Gupta, S. Dutta, S. Dutta, S. Sarkar

Indian Institute of Technology Madras, Madras, India
M.M. Ameen, P.K. Behera, S.C. Behera, S. Chatterjee, G. Dash, P. Jana, P. Kalbhor, S. Kamble, J.R. Komaragiri[35], D. Kumar[35], T. Mishra, B. Parida[36], P.R. Pujahari, N.R. Saha, A. Sharma, A.K. Sikdar, R.K. Singh, P. Verma, S. Verma, A. Vijay

Tata Institute of Fundamental Research-A, Mumbai, India
S. Dugad, G.B. Mohanty, M. Shelake, P. Suryadevara

Tata Institute of Fundamental Research-B, Mumbai, India
A. Bala, S. Banerjee, R.M. Chatterjee, M. Guchait, Sh. Jain, A. Jaiswal, S. Kumar, G. Majumder, K. Mazumdar, S. Parolia, A. Thachayath

National Institute of Science Education and Research, An OCC of Homi Bhabha National Institute, Bhubaneswar, Odisha, India
S. Bahinipati[37], C. Kar, D. Maity[38], P. Mal, K. Naskar[38], A. Nayak[38], S. Nayak, K. Pal, P. Sadangi, S.K. Swain, S. Varghese[38], D. Vats[38]

Indian Institute of Science Education and Research (IISER), Pune, India
S. Acharya[39], A. Alpana, S. Dube, B. Gomber[39], P. Hazarika, B. Kansal, A. Laha, B. Sahu[39], S. Sharma, K.Y. Vaish

Isfahan University of Technology, Isfahan, Iran
H. Bakhshiansohi[40], A. Jafari[41], M. Zeinali[42]

Institute for Research in Fundamental Sciences (IPM), Tehran, Iran
S. Bashiri, S. Chenarani[43], S.M. Etesami, Y. Hosseini, M. Khakzad, E. Khazaie, M. Mohammadi Najafabadi, S. Tizchang[44]

University College Dublin, Dublin, Ireland
M. Felcini, M. Grunewald

INFN Sezione di Bari[a], Università di Bari[b], Politecnico di Bari[c], Bari, Italy
M. Abbrescia[a,b], A. Colaleo[a,b], D. Creanza[a,c], B. D'Anzi[a,b], N. De Filippis[a,c], M. De Palma[a,b], W. Elmetenawee[a,b,45], N. Ferrara[a,b], L. Fiore[a], G. Iaselli[a,c], L. Longo[a], M. Louka[a,b], G. Maggi[a,c], M. Maggi[a], I. Margjeka[a], V. Mastrapasqua[a,b], S. My[a,b], S. Nuzzo[a,b], A. Pellecchia[a,b], A. Pompili[a,b], G. Pugliese[a,c], R. Radogna[a,b], D. Ramos[a], A. Ranieri[a], L. Silvestris[a], F.M. Simone[a,c], Ü. Sözbilir[a], A. Stamerra[a,b], D. Troiano[a,b], R. Venditti[a,b], P. Verwilligen[a], A. Zaza[a,b]

INFN Sezione di Bologna[a], Università di Bologna[b], Bologna, Italy
G. Abbiendi[a], C. Battilana[a,b], D. Bonacorsi[a,b], P. Capiluppi[a,b], A. Castro[†a,b], F.R. Cavallo[a], M. Cuffiani[a,b], G.M. Dallavalle[a], T. Diotalevi[a,b], F. Fabbri[a], A. Fanfani[a,b], D. Fasanella[a], P. Giacomelli[a], L. Giommi[a,b], C. Grandi[a], L. Guiducci[a,b], S. Lo Meo[a,46], M. Lorusso[a,b], L. Lunerti[a], S. Marcellini[a], G. Masetti[a], F.L. Navarria[a,b], G. Paggi[a,b], A. Perrotta[a], F. Primavera[a,b], A.M. Rossi[a,b], S. Rossi Tisbeni[a,b], T. Rovelli[a,b], G.P. Siroli[a,b]

INFN Sezione di Catania[a], Università di Catania[b], Catania, Italy
S. Costa[a,b,47], A. Di Mattia[a], A. Lapertosa[a], R. Potenza[a,b], A. Tricomi[a,b,47], C. Tuve[a,b]

INFN Sezione di Firenze[a], Università di Firenze[b], Firenze, Italy
P. Assiouras[a], G. Barbagli[a], G. Bardelli[a,b], B. Camaiani[a,b], A. Cassese[a], R. Ceccarelli[a], V. Ciulli[a,b], C. Civinini[a], R. D'Alessandro[a,b], E. Focardi[a,b], T. Kello[a], G. Latino[a,b], P. Lenzi[a,b], M. Lizzo[a], M. Meschini[a], S. Paoletti[a], A. Papanastassiou[a,b], G. Sguazzoni[a], L. Viliani[a]

INFN Laboratori Nazionali di Frascati, Frascati, Italy
L. Benussi, S. Bianco, S. Meola[48], D. Piccolo

INFN Sezione di Genova[a], Università di Genova[b], Genova, Italy
M. Alves Gallo Pereira[a], F. Ferro[a], E. Robutti[a], S. Tosi[a,b]

INFN Sezione di Milano-Bicocca[a], Università di Milano-Bicocca[b], Milano, Italy
A. Benaglia[a], F. Brivio[a], F. Cetorelli[a,b], F. De Guio[a,b], M.E. Dinardo[a,b], P. Dini[a], S. Gennai[a], R. Gerosa[a,b], A. Ghezzi[a,b], P. Govoni[a,b], L. Guzzi[a], M.T. Lucchini[a,b], M. Malberti[a], S. Malvezzi[a], A. Massironi[a], D. Menasce[a], L. Moroni[a], M. Paganoni[a,b], S. Palluotto[a,b], D. Pedrini[a], A. Perego[a,b], B.S. Pinolini[a], G. Pizzati[a,b], S. Ragazzi[a,b], T. Tabarelli de Fatis[a,b]

INFN Sezione di Napoli[a], Università di Napoli 'Federico II'[b], Napoli, Italy; Università della Basilicata[c], Potenza, Italy; Scuola Superiore Meridionale (SSM)[d], Napoli, Italy
S. Buontempo[a], A. Cagnotta[a,b], F. Carnevali[a,b], N. Cavallo[a,c], F. Fabozzi[a,c], A.O.M. Iorio[a,b], L. Lista[a,b,49], P. Paolucci[a,27], B. Rossi[a]

INFN Sezione di Padova[a], Università di Padova[b], Padova, Italy; Università di Trento[c], Trento, Italy
R. Ardino[a], P. Azzi[a], N. Bacchetta[a,50], D. Bisello[a,b], P. Bortignon[a], G. Bortolato[a,b], A. Bragagnolo[a,b], A.C.M. Bulla[a], R. Carlin[a,b], T. Dorigo[a], F. Gasparini[a,b], U. Gasparini[a,b], S. Giorgetti[a], M. Gulmini[a,51], E. Lusiani[a], M. Margoni[a,b], A.T. Meneguzzo[a,b], M. Migliorini[a,b], J. Pazzini[a,b], P. Ronchese[a,b], R. Rossin[a,b], F. Simonetto[a,b], M. Tosi[a,b], A. Triossi[a,b], S. Ventura[a], M. Zanetti[a,b], P. Zotto[a,b], A. Zucchetta[a,b], G. Zumerle[a,b]

INFN Sezione di Pavia[a], Università di Pavia[b], Pavia, Italy
A. Braghieri[a], S. Calzaferri[a], D. Fiorina[a], P. Montagna[a,b], V. Re[a], C. Riccardi[a,b], P. Salvini[a], I. Vai[a,b], P. Vitulo[a,b]

INFN Sezione di Perugia[a], Università di Perugia[b], Perugia, Italy
S. Ajmal[a,b], M.E. Ascioti[a,b], G.M. Bilei[a], C. Carrivale[a,b], D. Ciangottini[a,b], L. Fanò[a,b], M. Magherini[a,b], V. Mariani[a,b], M. Menichelli[a], F. Moscatelli[a,52], A. Rossi[a,b], A. Santocchia[a,b], D. Spiga[a], T. Tedeschi[a,b]

INFN Sezione di Pisa[a], Università di Pisa[b], Scuola Normale Superiore di Pisa[c], Pisa, Italy; Università di Siena[d], Siena, Italy
C. Aimè[a], C.A. Alexe[a,c], P. Asenov[a,b], P. Azzurri[a], G. Bagliesi[a], R. Bhattacharya[a], L. Bianchini[a,b], T. Boccali[a], E. Bossini[a], D. Bruschini[a,c], R. Castaldi[a], M.A. Ciocci[a,b], M. Cipriani[a,b], V. D'Amante[a,d], R. Dell'Orso[a], S. Donato[a], A. Giassi[a], F. Ligabue[a,c], A.C. Marini[a], D. Matos Figueiredo[a], A. Messineo[a,b], S. Mishra[a], V.K. Muraleedharan Nair Bindhu[a,b,38], M. Musich[a,b], F. Palla[a], A. Rizzi[a,b], G. Rolandi[a,c], S. Roy Chowdhury[a], T. Sarkar[a], A. Scribano[a], P. Spagnolo[a], R. Tenchini[a], G. Tonelli[a,b], N. Turini[a,d], F. Vaselli[a,c], A. Venturi[a], P.G. Verdini[a]

INFN Sezione di Roma[a], Sapienza Università di Roma[b], Roma, Italy
C. Baldenegro Barrera[a,b], P. Barria[a], C. Basile[a,b], F. Cavallari[a], L. Cunqueiro Mendez[a,b], D. Del Re[a,b], E. Di Marco[a,b], M. Diemoz[a], F. Errico[a,b], R. Gargiulo[a,b], E. Longo[a,b], L. Martikainen[a,b], J. Mijuskovic[a,b], G. Organtini[a,b], F. Pandolfi[a], R. Paramatti[a,b], C. Quaranta[a,b], S. Rahatlou[a,b], C. Rovelli[a], F. Santanastasio[a,b], L. Soffi[a], V. Vladimirov[a,b]

INFN Sezione di Torino[a], Università di Torino[b], Torino, Italy; Università del Piemonte Orientale[c], Novara, Italy

N. Amapane[a,b], R. Arcidiacono[a,c], S. Argiro[a,b], M. Arneodo[a,c], N. Bartosik[a], R. Bellan[a,b], A. Bellora[a,b], C. Biino[a], C. Borca[a,b], N. Cartiglia[a], M. Costa[a,b], R. Covarelli[a,b], N. Demaria[a], L. Finco[a], M. Grippo[a,b], B. Kiani[a,b], F. Legger[a], F. Luongo[a,b], C. Mariotti[a], L. Markovic[a,b], S. Maselli[a], A. Mecca[a,b], L. Menzio[a,b], P. Meridiani[a], E. Migliore[a,b], M. Monteno[a], R. Mulargia[a], M.M. Obertino[a,b], G. Ortona[a], L. Pacher[a,b], N. Pastrone[a], M. Pelliccioni[a], M. Ruspa[a,c], F. Siviero[a,b], V. Sola[a,b], A. Solano[a,b], A. Staiano[a], C. Tarricone[a,b], D. Trocino[a], G. Umoret[a,b], R. White[a,b]

INFN Sezione di Trieste[a], Università di Trieste[b], Trieste, Italy
J. Babbar[a,b], S. Belforte[a], V. Candelise[a,b], M. Casarsa[a], F. Cossutti[a], K. De Leo[a], G. Della Ricca[a,b]

Kyungpook National University, Daegu, Korea
S. Dogra, J. Hong, B. Kim, J. Kim, D. Lee, H. Lee, S.W. Lee, C.S. Moon, Y.D. Oh, M.S. Ryu, S. Sekmen, B. Tae, Y.C. Yang

Department of Mathematics and Physics - GWNU, Gangneung, Korea
M.S. Kim

Chonnam National University, Institute for Universe and Elementary Particles, Kwangju, Korea
G. Bak, P. Gwak, H. Kim, D.H. Moon

Hanyang University, Seoul, Korea
E. Asilar, J. Choi, D. Kim, T.J. Kim, J.A. Merlin, Y. Ryou

Korea University, Seoul, Korea
S. Choi, S. Han, B. Hong, K. Lee, K.S. Lee, S. Lee, J. Yoo

Kyung Hee University, Department of Physics, Seoul, Korea
J. Goh, S. Yang

Sejong University, Seoul, Korea
H. S. Kim, Y. Kim, S. Lee

Seoul National University, Seoul, Korea
J. Almond, J.H. Bhyun, J. Choi, J. Choi, W. Jun, J. Kim, Y.W. Kim, S. Ko, H. Kwon, H. Lee, J. Lee, J. Lee, B.H. Oh, S.B. Oh, H. Seo, U.K. Yang, I. Yoon

University of Seoul, Seoul, Korea
W. Jang, D.Y. Kang, Y. Kang, S. Kim, B. Ko, J.S.H. Lee, Y. Lee, I.C. Park, Y. Roh, I.J. Watson

Yonsei University, Department of Physics, Seoul, Korea
S. Ha, K. Hwang, H.D. Yoo

Sungkyunkwan University, Suwon, Korea
M. Choi, M.R. Kim, H. Lee, Y. Lee, I. Yu

College of Engineering and Technology, American University of the Middle East (AUM), Dasman, Kuwait
T. Beyrouthy, Y. Gharbia

Kuwait University - College of Science - Department of Physics, Safat, Kuwait
F. Alazemi

Riga Technical University, Riga, Latvia
K. Dreimanis, A. Gaile, C. Munoz Diaz, D. Osite, G. Pikurs, A. Potrebko, M. Seidel, D. Sidiropoulos Kontos

University of Latvia (LU), Riga, Latvia
N.R. Strautnieks

Vilnius University, Vilnius, Lithuania
M. Ambrozas, A. Juodagalvis, A. Rinkevicius, G. Tamulaitis

National Centre for Particle Physics, Universiti Malaya, Kuala Lumpur, Malaysia
I. Yusuff[53], Z. Zolkapli

Universidad de Sonora (UNISON), Hermosillo, Mexico
J.F. Benitez, A. Castaneda Hernandez, H.A. Encinas Acosta, L.G. Gallegos Maríñez, M. León Coello, J.A. Murillo Quijada, A. Sehrawat, L. Valencia Palomo

Centro de Investigacion y de Estudios Avanzados del IPN, Mexico City, Mexico
G. Ayala, H. Castilla-Valdez, H. Crotte Ledesma, E. De La Cruz-Burelo, I. Heredia-De La Cruz[54], R. Lopez-Fernandez, J. Mejia Guisao, C.A. Mondragon Herrera, A. Sánchez Hernández

Universidad Iberoamericana, Mexico City, Mexico
C. Oropeza Barrera, D.L. Ramirez Guadarrama, M. Ramírez García

Benemerita Universidad Autonoma de Puebla, Puebla, Mexico
I. Bautista, I. Pedraza, H.A. Salazar Ibarguen, C. Uribe Estrada

University of Montenegro, Podgorica, Montenegro
I. Bubanja, N. Raicevic

University of Canterbury, Christchurch, New Zealand
P.H. Butler

National Centre for Physics, Quaid-I-Azam University, Islamabad, Pakistan
A. Ahmad, M.I. Asghar, A. Awais, M.I.M. Awan, H.R. Hoorani, W.A. Khan

AGH University of Krakow, Krakow, Poland
V. Avati, L. Grzanka, M. Malawski

National Centre for Nuclear Research, Swierk, Poland
H. Bialkowska, M. Bluj, M. Górski, M. Kazana, M. Szleper, P. Zalewski

Institute of Experimental Physics, Faculty of Physics, University of Warsaw, Warsaw, Poland
K. Bunkowski, K. Doroba, A. Kalinowski, M. Konecki, J. Krolikowski, A. Muhammad

Warsaw University of Technology, Warsaw, Poland
P. Fokow, K. Pozniak, W. Zabolotny

Laboratório de Instrumentação e Física Experimental de Partículas, Lisboa, Portugal
M. Araujo, D. Bastos, C. Beirão Da Cruz E Silva, A. Boletti, M. Bozzo, T. Camporesi, G. Da Molin, P. Faccioli, M. Gallinaro, J. Hollar, N. Leonardo, G.B. Marozzo, A. Petrilli, M. Pisano, J. Seixas, J. Varela, J.W. Wulff

Faculty of Physics, University of Belgrade, Belgrade, Serbia
P. Adzic, P. Milenovic

VINCA Institute of Nuclear Sciences, University of Belgrade, Belgrade, Serbia
D. Devetak, M. Dordevic, J. Milosevic, L. Nadderd, V. Rekovic

Centro de Investigaciones Energéticas Medioambientales y Tecnológicas (CIEMAT), Madrid, Spain
J. Alcaraz Maestre, Cristina F. Bedoya, J.A. Brochero Cifuentes, Oliver M. Carretero, M. Cepeda, M. Cerrada, N. Colino, B. De La Cruz, A. Delgado Peris, A. Escalante Del Valle, D. Fernández Del Val, J.P. Fernández Ramos, J. Flix, M.C. Fouz, O. Gonzalez Lopez, S. Goy Lopez, J.M. Hernandez, M.I. Josa, J. Llorente Merino, C. Martin Perez, E. Martin Viscasillas, D. Moran, C. M. Morcillo Perez, Á. Navarro Tobar, C. Perez Dengra, A. Pérez-Calero Yzquierdo, J. Puerta Pelayo, I. Redondo, S. Sánchez Navas, J. Sastre, J. Vazquez Escobar

Universidad Autónoma de Madrid, Madrid, Spain
J.F. de Trocóniz

Universidad de Oviedo, Instituto Universitario de Ciencias y Tecnologías Espaciales de Asturias (ICTEA), Oviedo, Spain
B. Alvarez Gonzalez, J. Cuevas, J. Fernandez Menendez, S. Folgueras, I. Gonzalez Caballero, P. Leguina, E. Palencia Cortezon, J. Prado Pico, C. Ramón Álvarez, V. Rodríguez Bouza, A. Soto Rodríguez, A. Trapote, C. Vico Villalba, P. Vischia

Instituto de Física de Cantabria (IFCA), CSIC-Universidad de Cantabria, Santander, Spain
S. Bhowmik, S. Blanco Fernández, I.J. Cabrillo, A. Calderon, J. Duarte Campderros, M. Fernandez, G. Gomez, C. Lasaosa García, R. Lopez Ruiz, C. Martinez Rivero, P. Martinez Ruiz del Arbol, F. Matorras, P. Matorras Cuevas, E. Navarrete Ramos, J. Piedra Gomez, L. Scodellaro, I. Vila, J.M. Vizan Garcia

University of Colombo, Colombo, Sri Lanka
B. Kailasapathy[55], D.D.C. Wickramarathna

University of Ruhuna, Department of Physics, Matara, Sri Lanka
W.G.D. Dharmaratna[56], K. Liyanage, N. Perera

CERN, European Organization for Nuclear Research, Geneva, Switzerland
D. Abbaneo, C. Amendola, E. Auffray, G. Auzinger, J. Baechler, D. Barney, A. Bermúdez Martínez, M. Bianco, A.A. Bin Anuar, A. Bocci, L. Borgonovi, C. Botta, E. Brondolin, C. Caillol, G. Cerminara, N. Chernyavskaya, D. d'Enterria, A. Dabrowski, A. David, A. De Roeck, M.M. Defranchis, M. Deile, M. Dobson, G. Franzoni, W. Funk, S. Giani, D. Gigi, K. Gill, F. Glege, J. Hegeman, J.K. Heikkilä, B. Huber, V. Innocente, T. James, P. Janot, O. Kaluzinska, O. Karacheban[25], S. Laurila, P. Lecoq, E. Leutgeb, C. Lourenço, L. Malgeri, M. Mannelli, M. Matthewman, A. Mehta, F. Meijers, S. Mersi, E. Meschi, V. Milosevic, F. Monti, F. Moortgat, M. Mulders, I. Neutelings, S. Orfanelli, F. Pantaleo, G. Petrucciani, A. Pfeiffer, M. Pierini, H. Qu, D. Rabady, B. Ribeiro Lopes, F. Riti, M. Rovere, H. Sakulin, R. Salvatico, S. Sanchez Cruz, S. Scarfi, C. Schwick, M. Selvaggi, A. Sharma, K. Shchelina, P. Silva, P. Sphicas[57], A.G. Stahl Leiton, A. Steen, S. Summers, D. Treille, P. Tropea, D. Walter, J. Wanczyk[58], J. Wang, K.A. Wozniak[59], S. Wuchterl, P. Zehetner, P. Zejdl, W.D. Zeuner

Paul Scherrer Institut, Villigen, Switzerland
T. Bevilacqua[60], L. Caminada[60], A. Ebrahimi, W. Erdmann, R. Horisberger,

Q. Ingram, H.C. Kaestli, D. Kotlinski, C. Lange, M. Missiroli[60], L. Noehte[60], T. Rohe, A. Samalan

ETH Zurich - Institute for Particle Physics and Astrophysics (IPA), Zurich, Switzerland
T.K. Aarrestad, M. Backhaus, G. Bonomelli, A. Calandri, C. Cazzaniga, K. Datta, P. De Bryas Dexmiers D'archiac[58], A. De Cosa, G. Dissertori, M. Dittmar, M. Donegà, F. Eble, M. Galli, K. Gedia, F. Glessgen, C. Grab, N. Härringer, T.G. Harte, D. Hits, W. Lustermann, A.-M. Lyon, R.A. Manzoni, M. Marchegiani, L. Marchese, A. Mascellani[58], F. Nessi-Tedaldi, F. Pauss, V. Perovic, S. Pigazzini, B. Ristic, R. Seidita, J. Steggemann[58], A. Tarabini, D. Valsecchi, R. Wallny

Universität Zürich, Zurich, Switzerland
C. Amsler[61], P. Bärtschi, M.F. Canelli, K. Cormier, M. Huwiler, W. Jin, A. Jofrehei, B. Kilminster, S. Leontsinis, S.P. Liechti, A. Macchiolo, P. Meiring, F. Meng, J. Motta, A. Reimers, P. Robmann, M. Senger, E. Shokr, F. Stäger, R. Tramontano

National Central University, Chung-Li, Taiwan
C. Adloff[62], D. Bhowmik, C.M. Kuo, W. Lin, P.K. Rout, P.C. Tiwari[35]

National Taiwan University (NTU), Taipei, Taiwan
L. Ceard, K.F. Chen, Z.g. Chen, A. De Iorio, W.-S. Hou, T.h. Hsu, Y.w. Kao, S. Karmakar, G. Kole, Y.y. Li, R.-S. Lu, E. Paganis, X.f. Su, J. Thomas-Wilsker, L.s. Tsai, D. Tsionou, H.y. Wu, E. Yazgan

High Energy Physics Research Unit, Department of Physics, Faculty of Science, Chulalongkorn University, Bangkok, Thailand
C. Asawatangtrakuldee, N. Srimanobhas, V. Wachirapusitanand

Çukurova University, Physics Department, Science and Art Faculty, Adana, Turkey
D. Agyel, F. Boran, F. Dolek, I. Dumanoglu[63], E. Eskut, Y. Guler[64], E. Gurpinar Guler[64], C. Isik, O. Kara, A. Kayis Topaksu, U. Kiminsu, Y. Komurcu, G. Onengut, K. Ozdemir[65], A. Polatoz, B. Tali[66], U.G. Tok, E. Uslan, I.S. Zorbakir

Middle East Technical University, Physics Department, Ankara, Turkey
G. Sokmen, M. Yalvac[67]

Bogazici University, Istanbul, Turkey
B. Akgun, I.O. Atakisi, E. Gülmez, M. Kaya[68], O. Kaya[69], S. Tekten[70]

Istanbul Technical University, Istanbul, Turkey
A. Cakir, K. Cankocak[63,71], G.G. Dincer[63], S. Sen[72]

Istanbul University, Istanbul, Turkey
O. Aydilek[73], B. Hacisahinoglu, I. Hos[74], B. Kaynak, S. Ozkorucuklu, O. Potok, H. Sert, C. Simsek, C. Zorbilmez

Yildiz Technical University, Istanbul, Turkey
S. Cerci, B. Isildak[75], D. Sunar Cerci, T. Yetkin

Institute for Scintillation Materials of National Academy of Science of Ukraine, Kharkiv, Ukraine
A. Boyaryntsev, B. Grynyov

National Science Centre, Kharkiv Institute of Physics and Technology, Kharkiv, Ukraine

L. Levchuk

University of Bristol, Bristol, United Kingdom
D. Anthony, J.J. Brooke, A. Bundock, F. Bury, E. Clement, D. Cussans, H. Flacher, M. Glowacki, J. Goldstein, H.F. Heath, M.-L. Holmberg, L. Kreczko, S. Paramesvaran, L. Robertshaw, V.J. Smith, K. Walkingshaw Pass

Rutherford Appleton Laboratory, Didcot, United Kingdom
A.H. Ball, K.W. Bell, A. Belyaev[76], C. Brew, R.M. Brown, D.J.A. Cockerill, C. Cooke, A. Elliot, K.V. Ellis, K. Harder, S. Harper, J. Linacre, K. Manolopoulos, D.M. Newbold, E. Olaiya, D. Petyt, T. Reis, A.R. Sahasransu, G. Salvi, T. Schuh, C.H. Shepherd-Themistocleous, I.R. Tomalin, K.C. Whalen, T. Williams

Imperial College, London, United Kingdom
I. Andreou, R. Bainbridge, P. Bloch, C.E. Brown, O. Buchmuller, C.A. Carrillo Montoya, G.S. Chahal[77], D. Colling, J.S. Dancu, I. Das, P. Dauncey, G. Davies, M. Della Negra, S. Fayer, G. Fedi, G. Hall, A. Howard, G. Iles, C.R. Knight, P. Krueper, J. Langford, K.H. Law, J. León Holgado, L. Lyons, A.-M. Magnan, B. Maier, S. Mallios, M. Mieskolainen, J. Nash[78], M. Pesaresi, P.B. Pradeep, B.C. Radburn-Smith, A. Richards, A. Rose, K. Savva, C. Seez, R. Shukla, A. Tapper, K. Uchida, G.P. Uttley, T. Virdee[27], M. Vojinovic, N. Wardle, D. Winterbottom

Brunel University, Uxbridge, United Kingdom
J.E. Cole, A. Khan, P. Kyberd, I.D. Reid

Baylor University, Waco, Texas, USA
S. Abdullin, A. Brinkerhoff, E. Collins, M.R. Darwish, J. Dittmann, K. Hatakeyama, V. Hegde, J. Hiltbrand, B. McMaster, J. Samudio, S. Sawant, C. Sutantawibul, J. Wilson

Catholic University of America, Washington, DC, USA
R. Bartek, A. Dominguez, A.E. Simsek, S.S. Yu

The University of Alabama, Tuscaloosa, Alabama, USA
B. Bam, A. Buchot Perraguin, R. Chudasama, S.I. Cooper, C. Crovella, S.V. Gleyzer, E. Pearson, C.U. Perez, P. Rumerio[79], E. Usai, R. Yi

Boston University, Boston, Massachusetts, USA
A. Akpinar, C. Cosby, G. De Castro, Z. Demiragli, C. Erice, C. Fangmeier, C. Fernandez Madrazo, E. Fontanesi, D. Gastler, F. Golf, S. Jeon, J. O'cain, I. Reed, J. Rohlf, K. Salyer, D. Sperka, D. Spitzbart, I. Suarez, A. Tsatsos, A.G. Zecchinelli

Brown University, Providence, Rhode Island, USA
G. Barone, G. Benelli, D. Cutts, L. Gouskos, M. Hadley, U. Heintz, K.W. Ho, J.M. Hogan[80], T. Kwon, G. Landsberg, K.T. Lau, J. Luo, S. Mondal, T. Russell, S. Sagir[81], X. Shen, F. Simpson, M. Stamenkovic, N. Venkatasubramanian

University of California, Davis, Davis, California, USA
S. Abbott, B. Barton, C. Brainerd, R. Breedon, H. Cai, M. Calderon De La Barca Sanchez, M. Chertok, M. Citron, J. Conway, P.T. Cox, R. Erbacher, F. Jensen, O. Kukral, G. Mocellin, M. Mulhearn, S. Ostrom, W. Wei, S. Yoo, F. Zhang

University of California, Los Angeles, California, USA
K. Adamidis, M. Bachtis, D. Campos, R. Cousins, A. Datta, G. Flores Avila, J. Hauser, M. Ignatenko, M.A. Iqbal, T. Lam, Y.f. Lo, E. Manca, A. Nunez Del Prado, D. Saltzberg, V. Valuev

University of California, Riverside, Riverside, California, USA
R. Clare, J.W. Gary, G. Hanson

University of California, San Diego, La Jolla, California, USA
A. Aportela, A. Arora, J.G. Branson, S. Cittolin, S. Cooperstein, D. Diaz, J. Duarte, L. Giannini, Y. Gu, J. Guiang, R. Kansal, V. Krutelyov, R. Lee, J. Letts, M. Masciovecchio, F. Mokhtar, S. Mukherjee, M. Pieri, D. Primosch, M. Quinnan, B.V. Sathia Narayanan, V. Sharma, M. Tadel, E. Vourliotis, F. Würthwein, Y. Xiang, A. Yagil

University of California, Santa Barbara - Department of Physics, Santa Barbara, California, USA
A. Barzdukas, L. Brennan, C. Campagnari, K. Downham, C. Grieco, M.M. Hussain, J. Incandela, J. Kim, A.J. Li, P. Masterson, H. Mei, J. Richman, S.N. Santpur, U. Sarica, R. Schmitz, F. Setti, J. Sheplock, D. Stuart, T.Á. Vámi, S. Wang, X. Yan, D. Zhang

California Institute of Technology, Pasadena, California, USA
S. Bhattacharya, A. Bornheim, O. Cerri, A. Latorre, J. Mao, H.B. Newman, G. Reales Gutiérrez, M. Spiropulu, J.R. Vlimant, C. Wang, S. Xie, R.Y. Zhu

Carnegie Mellon University, Pittsburgh, Pennsylvania, USA
J. Alison, S. An, P. Bryant, M. Cremonesi, V. Dutta, T. Ferguson, T.A. Gómez Espinosa, A. Harilal, A. Kallil Tharayil, C. Liu, T. Mudholkar, S. Murthy, P. Palit, K. Park, M. Paulini, A. Roberts, A. Sanchez, W. Terrill

University of Colorado Boulder, Boulder, Colorado, USA
J.P. Cumalat, W.T. Ford, A. Hart, A. Hassani, G. Karathanasis, N. Manganelli, J. Pearkes, C. Savard, N. Schonbeck, K. Stenson, K.A. Ulmer, S.R. Wagner, N. Zipper, D. Zuolo

Cornell University, Ithaca, New York, USA
J. Alexander, S. Bright-Thonney, X. Chen, D.J. Cranshaw, J. Dickinson, J. Fan, X. Fan, S. Hogan, P. Kotamnives, J. Monroy, M. Oshiro, J.R. Patterson, M. Reid, A. Ryd, J. Thom, P. Wittich, R. Zou

Fermi National Accelerator Laboratory, Batavia, Illinois, USA
M. Albrow, M. Alyari, O. Amram, G. Apollinari, A. Apresyan, L.A.T. Bauerdick, D. Berry, J. Berryhill, P.C. Bhat, K. Burkett, J.N. Butler, A. Canepa, G.B. Cerati, H.W.K. Cheung, F. Chlebana, G. Cummings, I. Dutta, V.D. Elvira, Y. Feng, J. Freeman, A. Gandrakota, Z. Gecse, L. Gray, D. Green, A. Grummer, S. Grünendahl, D. Guerrero, O. Gutsche, R.M. Harris, R. Heller, T.C. Herwig, J. Hirschauer, B. Jayatilaka, S. Jindariani, M. Johnson, U. Joshi, T. Klijnsma, B. Klima, K.H.M. Kwok, S. Lammel, C. Lee, D. Lincoln, R. Lipton, T. Liu, C. Madrid, K. Maeshima, C. Mantilla, D. Mason, P. McBride, P. Merkel, S. Mrenna, S. Nahn, J. Ngadiuba, D. Noonan, S. Norberg, V. Papadimitriou, N. Pastika, K. Pedro, C. Pena[82], F. Ravera, A. Reinsvold Hall[83], L. Ristori, M. Safdari, E. Sexton-Kennedy, N. Smith, A. Soha, L. Spiegel, S. Stoynev,

J. Strait, L. Taylor, S. Tkaczyk, N.V. Tran, L. Uplegger, E.W. Vaandering, I. Zoi

University of Florida, Gainesville, Florida, USA
C. Aruta, P. Avery, D. Bourilkov, P. Chang, V. Cherepanov, R.D. Field, C. Huh, E. Koenig, M. Kolosova, J. Konigsberg, A. Korytov, K. Matchev, N. Menendez, G. Mitselmakher, K. Mohrman, A. Muthirakalayil Madhu, N. Rawal, S. Rosenzweig, Y. Takahashi, J. Wang

Florida State University, Tallahassee, Florida, USA
T. Adams, A. Al Kadhim, A. Askew, S. Bower, R. Hashmi, R.S. Kim, S. Kim, T. Kolberg, G. Martinez, H. Prosper, P.R. Prova, M. Wulansatiti, R. Yohay, J. Zhang

Florida Institute of Technology, Melbourne, Florida, USA
B. Alsufyani, S. Butalla, S. Das, T. Elkafrawy[84], M. Hohlmann, E. Yanes

University of Illinois Chicago, Chicago, Illinois, USA
M.R. Adams, A. Baty, C. Bennett, R. Cavanaugh, R. Escobar Franco, O. Evdokimov, C.E. Gerber, M. Hawksworth, A. Hingrajiya, D.J. Hofman, J.h. Lee, D. S. Lemos, A.H. Merrit, C. Mills, S. Nanda, G. Oh, B. Ozek, D. Pilipovic, R. Pradhan, E. Prifti, T. Roy, S. Rudrabhatla, N. Singh, M.B. Tonjes, N. Varelas, M.A. Wadud, Z. Ye, J. Yoo

The University of Iowa, Iowa City, Iowa, USA
M. Alhusseini, D. Blend, K. Dilsiz[85], L. Emediato, G. Karaman, O.K. Köseyan, J.-P. Merlo, A. Mestvirishvili[86], O. Neogi, H. Ogul[87], Y. Onel, A. Penzo, C. Snyder, E. Tiras[88]

Johns Hopkins University, Baltimore, Maryland, USA
B. Blumenfeld, L. Corcodilos, J. Davis, A.V. Gritsan, L. Kang, S. Kyriacou, P. Maksimovic, M. Roguljic, J. Roskes, S. Sekhar, M. Swartz

The University of Kansas, Lawrence, Kansas, USA
A. Abreu, L.F. Alcerro Alcerro, J. Anguiano, S. Arteaga Escatel, P. Baringer, A. Bean, Z. Flowers, D. Grove, J. King, G. Krintiras, M. Lazarovits, C. Le Mahieu, J. Marquez, M. Murray, M. Nickel, M. Pitt, S. Popescu[89], C. Rogan, C. Royon, S. Sanders, C. Smith, G. Wilson

Kansas State University, Manhattan, Kansas, USA
B. Allmond, R. Gujju Gurunadha, A. Ivanov, K. Kaadze, Y. Maravin, J. Natoli, D. Roy, G. Sorrentino

University of Maryland, College Park, Maryland, USA
A. Baden, A. Belloni, J. Bistany-riebman, Y.M. Chen, S.C. Eno, N.J. Hadley, S. Jabeen, R.G. Kellogg, T. Koeth, B. Kronheim, Y. Lai, S. Lascio, A.C. Mignerey, S. Nabili, C. Palmer, C. Papageorgakis, M.M. Paranjpe, E. Popova[90], A. Shevelev, L. Wang

Massachusetts Institute of Technology, Cambridge, Massachusetts, USA
J. Bendavid, I.A. Cali, P.c. Chou, M. D'Alfonso, J. Eysermans, C. Freer, G. Gomez-Ceballos, M. Goncharov, G. Grosso, P. Harris, D. Hoang, D. Kovalskyi, J. Krupa, L. Lavezzo, Y.-J. Lee, K. Long, C. Mcginn, A. Novak, M.I. Park, C. Paus, C. Reissel, C. Roland, G. Roland, S. Rothman, G.S.F. Stephans, Z. Wang, B. Wyslouch, T. J. Yang

University of Minnesota, Minneapolis, Minnesota, USA

B. Crossman, B.M. Joshi, C. Kapsiak, M. Krohn, D. Mahon, J. Mans, B. Marzocchi, M. Revering, R. Rusack, R. Saradhy, N. Strobbe

University of Nebraska-Lincoln, Lincoln, Nebraska, USA
K. Bloom, D.R. Claes, G. Haza, J. Hossain, C. Joo, I. Kravchenko, A. Rohilla, J.E. Siado, W. Tabb, A. Vagnerini, A. Wightman, F. Yan, D. Yu

State University of New York at Buffalo, Buffalo, New York, USA
H. Bandyopadhyay, L. Hay, H.w. Hsia, I. Iashvili, A. Kalogeropoulos, A. Kharchilava, M. Morris, D. Nguyen, S. Rappoccio, H. Rejeb Sfar, A. Williams, P. Young

Northeastern University, Boston, Massachusetts, USA
G. Alverson, E. Barberis, J. Bonilla, B. Bylsma, M. Campana, J. Dervan, Y. Haddad, Y. Han, I. Israr, A. Krishna, J. Li, M. Lu, G. Madigan, R. Mccarthy, D.M. Morse, V. Nguyen, T. Orimoto, A. Parker, L. Skinnari, E. Tsai, D. Wood

Northwestern University, Evanston, Illinois, USA
J. Bueghly, S. Dittmer, K.A. Hahn, D. Li, Y. Liu, M. Mcginnis, Y. Miao, D.G. Monk, M.H. Schmitt, A. Taliercio, M. Velasco

University of Notre Dame, Notre Dame, Indiana, USA
G. Agarwal, R. Band, R. Bucci, S. Castells, A. Das, R. Goldouzian, M. Hildreth, K. Hurtado Anampa, T. Ivanov, C. Jessop, K. Lannon, J. Lawrence, N. Loukas, L. Lutton, J. Mariano, N. Marinelli, I. Mcalister, T. McCauley, C. Mcgrady, C. Moore, Y. Musienko[15], H. Nelson, M. Osherson, A. Piccinelli, R. Ruchti, A. Townsend, Y. Wan, M. Wayne, H. Yockey, M. Zarucki, L. Zygala

The Ohio State University, Columbus, Ohio, USA
A. Basnet, M. Carrigan, L.S. Durkin, C. Hill, M. Joyce, M. Nunez Ornelas, K. Wei, D.A. Wenzl, B.L. Winer, B. R. Yates

Princeton University, Princeton, New Jersey, USA
H. Bouchamaoui, K. Coldham, P. Das, G. Dezoort, P. Elmer, A. Frankenthal, B. Greenberg, N. Haubrich, K. Kennedy, G. Kopp, S. Kwan, D. Lange, A. Loeliger, D. Marlow, I. Ojalvo, J. Olsen, D. Stickland, C. Tully, L.H. Vage

University of Puerto Rico, Mayaguez, Puerto Rico, USA
S. Malik, R. Sharma

Purdue University, West Lafayette, Indiana, USA
A.S. Bakshi, S. Chandra, R. Chawla, A. Gu, L. Gutay, M. Jones, A.W. Jung, A.M. Koshy, M. Liu, G. Negro, N. Neumeister, G. Paspalaki, S. Piperov, V. Scheurer, J.F. Schulte, M. Stojanovic, J. Thieman, A. K. Virdi, F. Wang, A. Wildridge, W. Xie, Y. Yao

Purdue University Northwest, Hammond, Indiana, USA
J. Dolen, N. Parashar, A. Pathak

Rice University, Houston, Texas, USA
D. Acosta, T. Carnahan, K.M. Ecklund, P.J. Fernández Manteca, S. Freed, P. Gardner, F.J.M. Geurts, I. Krommydas, W. Li, J. Lin, O. Miguel Colin, B.P. Padley, R. Redjimi, J. Rotter, E. Yigitbasi, Y. Zhang

University of Rochester, Rochester, New York, USA

A. Bodek, P. de Barbaro, R. Demina, J.L. Dulemba, A. Garcia-Bellido, A. Herrera, O. Hindrichs, A. Khukhunaishvili, N. Parmar, P. Parygin[90], R. Taus

Rutgers, The State University of New Jersey, Piscataway, New Jersey, USA
B. Chiarito, J.P. Chou, S.V. Clark, D. Gadkari, Y. Gershtein, E. Halkiadakis, M. Heindl, C. Houghton, D. Jaroslawski, S. Konstantinou, I. Laflotte, A. Lath, R. Montalvo, K. Nash, J. Reichert, H. Routray, P. Saha, S. Salur, S. Schnetzer, S. Somalwar, R. Stone, S.A. Thayil, S. Thomas, J. Vora, H. Wang

University of Tennessee, Knoxville, Tennessee, USA
D. Ally, A.G. Delannoy, S. Fiorendi, S. Higginbotham, T. Holmes, A.R. Kanuganti, N. Karunarathna, L. Lee, E. Nibigira, S. Spanier

Texas A&M University, College Station, Texas, USA
D. Aebi, M. Ahmad, T. Akhter, K. Androsov[58], O. Bouhali[91], R. Eusebi, J. Gilmore, T. Huang, T. Kamon[92], H. Kim, S. Luo, R. Mueller, D. Overton, D. Rathjens, A. Safonov

Texas Tech University, Lubbock, Texas, USA
N. Akchurin, J. Damgov, N. Gogate, A. Hussain, Y. Kazhykarim, K. Lamichhane, S.W. Lee, A. Mankel, T. Peltola, I. Volobouev

Vanderbilt University, Nashville, Tennessee, USA
E. Appelt, Y. Chen, S. Greene, A. Gurrola, W. Johns, R. Kunnawalkam Elayavalli, A. Melo, F. Romeo, P. Sheldon, S. Tuo, J. Velkovska, J. Viinikainen

University of Virginia, Charlottesville, Virginia, USA
B. Cardwell, H. Chung, B. Cox, J. Hakala, R. Hirosky, A. Ledovskoy, C. Neu

Wayne State University, Detroit, Michigan, USA
S. Bhattacharya, P.E. Karchin

University of Wisconsin - Madison, Madison, Wisconsin, USA
A. Aravind, S. Banerjee, K. Black, T. Bose, E. Chavez, S. Dasu, P. Everaerts, C. Galloni, H. He, M. Herndon, A. Herve, C.K. Koraka, A. Lanaro, R. Loveless, J. Madhusudanan Sreekala, A. Mallampalli, A. Mohammadi, S. Mondal, G. Parida, L. Pétré, D. Pinna, A. Savin, V. Shang, V. Sharma, W.H. Smith, D. Teague, H.F. Tsoi, W. Vetens, A. Warden

Authors affiliated with an institute or an international laboratory covered by a cooperation agreement with CERN
S. Afanasiev, V. Alexakhin, D. Budkouski, I. Golutvin†, I. Gorbunov, V. Karjavine, V. Korenkov, A. Lanev, A. Malakhov, V. Matveev[93], V. Palichik, V. Perelygin, M. Savina, V. Shalaev, S. Shmatov, S. Shulha, V. Smirnov, O. Teryaev, N. Voytishin, B.S. Yuldashev[94], A. Zarubin, I. Zhizhin, G. Gavrilov, V. Golovtcov, Y. Ivanov, V. Kim[93], P. Levchenko[95], V. Murzin, V. Oreshkin, D. Sosnov, V. Sulimov, L. Uvarov, A. Vorobyev†, Yu. Andreev, A. Dermenev, S. Gninenko, N. Golubev, A. Karneyeu, D. Kirpichnikov, M. Kirsanov, N. Krasnikov, I. Tlisova, A. Toropin, T. Aushev, K. Ivanov, V. Gavrilov, N. Lychkovskaya, A. Nikitenko[96,97], V. Popov, A. Zhokin, R. Chistov[93], M. Danilov[93], S. Polikarpov[93], V. Andreev, M. Azarkin, M. Kirakosyan, A. Terkulov, E. Boos, V. Bunichev, M. Dubinin[82], L. Dudko, A. Ershov, V. Klyukhin, S. Obraztsov, M. Perfilov, S. Petrushanko, V. Savrin, P. Volkov, G. Vorotnikov, V. Blinov[93], T. Dimova[93], A. Kozyrev[93], O. Radchenko[93], Y. Skovpen[93], V. Kachanov, D. Kon-

stantinov, S. Slabospitskii, A. Uzunian, A. Babaev, V. Borshch, D. Druzhkin[98]

†: Deceased
[1]Also at Yerevan State University, Yerevan, Armenia
[2]Also at TU Wien, Vienna, Austria
[3]Also at Ghent University, Ghent, Belgium
[4]Also at Universidade do Estado do Rio de Janeiro, Rio de Janeiro, Brazil
[5]Also at FACAMP - Faculdades de Campinas, Sao Paulo, Brazil
[6]Also at Universidade Estadual de Campinas, Campinas, Brazil
[7]Also at Federal University of Rio Grande do Sul, Porto Alegre, Brazil
[8]Also at University of Chinese Academy of Sciences, Beijing, China
[9]Also at China Center of Advanced Science and Technology, Beijing, China
[10]Also at University of Chinese Academy of Sciences, Beijing, China
[11]Also at China Spallation Neutron Source, Guangdong, China
[12]Now at Henan Normal University, Xinxiang, China
[13]Also at University of Shanghai for Science and Technology, Shanghai, China
[14]Now at The University of Iowa, Iowa City, Iowa, USA
[15]Also at an institute or an international laboratory covered by a cooperation agreement with CERN
[16]Also at Suez University, Suez, Egypt
[17]Now at British University in Egypt, Cairo, Egypt
[18]Also at Purdue University, West Lafayette, Indiana, USA
[19]Also at Université de Haute Alsace, Mulhouse, France
[20]Also at Istinye University, Istanbul, Turkey
[21]Also at The University of the State of Amazonas, Manaus, Brazil
[22]Also at University of Hamburg, Hamburg, Germany
[23]Also at RWTH Aachen University, III. Physikalisches Institut A, Aachen, Germany
[24]Also at Bergische University Wuppertal (BUW), Wuppertal, Germany
[25]Also at Brandenburg University of Technology, Cottbus, Germany
[26]Also at Forschungszentrum Jülich, Juelich, Germany
[27]Also at CERN, European Organization for Nuclear Research, Geneva, Switzerland
[28]Also at Institute of Nuclear Research ATOMKI, Debrecen, Hungary
[29]Now at Universitatea Babes-Bolyai - Facultatea de Fizica, Cluj-Napoca, Romania
[30]Also at MTA-ELTE Lendület CMS Particle and Nuclear Physics Group, Eötvös Loránd University, Budapest, Hungary
[31]Also at HUN-REN Wigner Research Centre for Physics, Budapest, Hungary
[32]Also at Physics Department, Faculty of Science, Assiut University, Assiut, Egypt
[33]Also at Punjab Agricultural University, Ludhiana, India
[34]Also at University of Visva-Bharati, Santiniketan, India
[35]Also at Indian Institute of Science (IISc), Bangalore, India
[36]Also at Amity University Uttar Pradesh, Noida, India
[37]Also at IIT Bhubaneswar, Bhubaneswar, India
[38]Also at Institute of Physics, Bhubaneswar, India
[39]Also at University of Hyderabad, Hyderabad, India
[40]Also at Deutsches Elektronen-Synchrotron, Hamburg, Germany
[41]Also at Isfahan University of Technology, Isfahan, Iran
[42]Also at Sharif University of Technology, Tehran, Iran
[43]Also at Department of Physics, University of Science and Technology of Mazandaran, Behshahr, Iran
[44]Also at Department of Physics, Faculty of Science, Arak University, ARAK, Iran

[45]Also at Helwan University, Cairo, Egypt
[46]Also at Italian National Agency for New Technologies, Energy and Sustainable Economic Development, Bologna, Italy
[47]Also at Centro Siciliano di Fisica Nucleare e di Struttura Della Materia, Catania, Italy
[48]Also at Università degli Studi Guglielmo Marconi, Roma, Italy
[49]Also at Scuola Superiore Meridionale, Università di Napoli 'Federico II', Napoli, Italy
[50]Also at Fermi National Accelerator Laboratory, Batavia, Illinois, USA
[51]Also at Laboratori Nazionali di Legnaro dell'INFN, Legnaro, Italy
[52]Also at Consiglio Nazionale delle Ricerche - Istituto Officina dei Materiali, Perugia, Italy
[53]Also at Department of Applied Physics, Faculty of Science and Technology, Universiti Kebangsaan Malaysia, Bangi, Malaysia
[54]Also at Consejo Nacional de Ciencia y Tecnología, Mexico City, Mexico
[55]Also at Trincomalee Campus, Eastern University, Sri Lanka, Nilaveli, Sri Lanka
[56]Also at Saegis Campus, Nugegoda, Sri Lanka
[57]Also at National and Kapodistrian University of Athens, Athens, Greece
[58]Also at Ecole Polytechnique Fédérale Lausanne, Lausanne, Switzerland
[59]Also at University of Vienna, Vienna, Austria
[60]Also at Universität Zürich, Zurich, Switzerland
[61]Also at Stefan Meyer Institute for Subatomic Physics, Vienna, Austria
[62]Also at Laboratoire d'Annecy-le-Vieux de Physique des Particules, IN2P3-CNRS, Annecy-le-Vieux, France
[63]Also at Near East University, Research Center of Experimental Health Science, Mersin, Turkey
[64]Also at Konya Technical University, Konya, Turkey
[65]Also at Izmir Bakircay University, Izmir, Turkey
[66]Also at Adiyaman University, Adiyaman, Turkey
[67]Also at Bozok Universitetesi Rektörlügü, Yozgat, Turkey
[68]Also at Marmara University, Istanbul, Turkey
[69]Also at Milli Savunma University, Istanbul, Turkey
[70]Also at Kafkas University, Kars, Turkey
[71]Now at Istanbul Okan University, Istanbul, Turkey
[72]Also at Hacettepe University, Ankara, Turkey
[73]Also at Erzincan Binali Yildirim University, Erzincan, Turkey
[74]Also at Istanbul University - Cerrahpasa, Faculty of Engineering, Istanbul, Turkey
[75]Also at Yildiz Technical University, Istanbul, Turkey
[76]Also at School of Physics and Astronomy, University of Southampton, Southampton, United Kingdom
[77]Also at IPPP Durham University, Durham, United Kingdom
[78]Also at Monash University, Faculty of Science, Clayton, Australia
[79]Also at Università di Torino, Torino, Italy
[80]Also at Bethel University, St. Paul, Minnesota, USA
[81]Also at Karamanoğlu Mehmetbey University, Karaman, Turkey
[82]Also at California Institute of Technology, Pasadena, California, USA
[83]Also at United States Naval Academy, Annapolis, Maryland, USA
[84]Also at Ain Shams University, Cairo, Egypt
[85]Also at Bingol University, Bingol, Turkey
[86]Also at Georgian Technical University, Tbilisi, Georgia
[87]Also at Sinop University, Sinop, Turkey
[88]Also at Erciyes University, Kayseri, Turkey

[89]Also at Horia Hulubei National Institute of Physics and Nuclear Engineering (IFIN-HH), Bucharest, Romania
[90]Now at another institute or international laboratory covered by a cooperation agreement with CERN
[91]Also at Texas A&M University at Qatar, Doha, Qatar
[92]Also at Kyungpook National University, Daegu, Korea
[93]Also at another institute or international laboratory covered by a cooperation agreement with CERN
[94]Also at Institute of Nuclear Physics of the Uzbekistan Academy of Sciences, Tashkent, Uzbekistan
[95]Also at Northeastern University, Boston, Massachusetts, USA
[96]Also at Imperial College, London, United Kingdom
[97]Now at Yerevan Physics Institute, Yerevan, Armenia
[98]Also at Universiteit Antwerpen, Antwerpen, Belgium